SANDIA REPORT
SAND2001-3626
Unlimited Release
Printed November 2001

Linking Atomistic Simulations with Phase Field Modeling of Solidification

Jeffrey J. Hoyt, Mark Asta, Alain Karma

Prepared by
Sandia National Laboratories
Albuquerque, New Mexico 87185 and Livermore, California 94550

Sandia is a multiprogram laboratory operated by Sandia Corporation,
a Lockheed Martin Company, for the United States Department of
Energy under Contract DE-AC04-94AL85000.

Approved for public release; further dissemination unlimited.

Sandia National Laboratories

Issued by Sandia National Laboratories, operated for the United States Department of Energy by Sandia Corporation.

NOTICE: This report was prepared as an account of work sponsored by an agency of the United States Government. Neither the United States Government, nor any agency thereof, nor any of their employees, nor any of their contractors, subcontractors, or their employees, make any warranty, express or implied, or assume any legal liability or responsibility for the accuracy, completeness, or usefulness of any information, apparatus, product, or process disclosed, or represent that its use would not infringe privately owned rights. Reference herein to any specific commercial product, process, or service by trade name, trademark, manufacturer, or otherwise, does not necessarily constitute or imply its endorsement, recommendation, or favoring by the United States Government, any agency thereof, or any of their contractors or subcontractors. The views and opinions expressed herein do not necessarily state or reflect those of the United States Government, any agency thereof, or any of their contractors.

Printed in the United States of America. This report has been reproduced directly from the best available copy.

Available to DOE and DOE contractors from
U.S. Department of Energy
Office of Scientific and Technical Information
P.O. Box 62
Oak Ridge, TN 37831

Telephone: (865)576-8401
Facsimile: (865)576-5728
E-Mail: reports@adonis.osti.gov
Online ordering: http://www.doe.gov/bridge

Available to the public from
U.S. Department of Commerce
National Technical Information Service
5285 Port Royal Rd
Springfield, VA 22161

Telephone: (800)553-6847
Facsimile: (703)605-6900
E-Mail: orders@ntis.fedworld.gov
Online order: http://www.ntis.gov/ordering.htm

SAND2001-3626
Unlimited Release
Printed November 2001

Linking Atomistic Simulations with Phase Field Modeling of Solidification

LDRD 10303 Final Report

Jeffrey J. Hoyt
Materials & Process Modeling Department
Sandia National Laboratories
PO Box 5800
Albuquerque, NM

Mark Asta
Dept. of Materials Science and Engineering
Northwestern University
Evanston, IL

Alain Karma
Physics Department
Northeastern University
Boston, MA

Abstract

The phase field model provides an efficient numerical means to accurately model the complex morphologies observed in dendritic solidification of metals and alloys. In this

report we review the basic formulation of the phase field model and demonstrate its relation to the sharp interface description. In dendrite solidification at low undercooling or low supersaturation there exists several disparate length scales and implementation of the phase field technique in this important limit has remained a significant challenge. We shall review several techniques which have been successful in overcoming the length scale problem. Techniques include the thin interface limit, the use of adaptive mesh refinement and the use of random walkers.

Despite the demonstrated success of the phase field method, application of the technique to real alloy systems remains a formidable challenge. Several materials parameters, required as input to continuum models, are difficult, if not impossible, to measure experimentally. The liquid state diffusion coefficient, the solid-liquid interfacial free energy and the kinetic coefficient relating the velocity of a planar interface to the undercooling are examples of difficult to measure quantities required in the phase field formulation. More significantly, the small anisotropy of the latter two quantities is essential and must be included in the modeling problem. In this report we will describe in detail molecular dynamics and Monte Carlo simulations which have recently been developed to compute the necessary materials parameters and the anisotropies. Finally, it will be shown that parameters derived from atomistic simulation methods, when combined with phase field modeling, can accurately reproduce the experimentally measured dendrite growth velocity as a function of undercooling in pure Ni.

Table of Contents

1. Introduction 6

2. Continuum Modeling 8

2.1 Sharp Interface Models 9

2.1.1 Basic Equations 9

2.1.2 The Ivantsov Solution 11

2.1.3 Microscopic Solvability 13

2.2 The Phase Field Model 16

2.2.1 Basic Equations 16

2.2.2 The Thin Interface Limit 21

2.2.3 Adaptive Mesh Refinement Schemes 24

2.2.4 The Random Walker Technique 26

2.2.5 Binary Alloys 28

3. Atomistic Simulations 33

3.1 The Solid-Liquid Interfacial Free Energy 34

3.2 The Kinetic Coefficient 40

3.2.1 Forced Velocity Simulations 41

3.2.2 Free Solidification Simulations 43

3.2.3 Fluctuations 45

3.2.4 The Broughton, Gilmer and Jackson Growth Model 48

3.3 The Diffusion Coefficient 53

3.4 Binary Alloys 57

4. Experimental Validation 60

5. Summary and Future Directions 63

6. References 64

7. Tables and Figures 77

1. Introduction

The term dendrites refers to the branched tree-like solid spikes which propagate into the liquid during the solidification of supercooled pure melts or supersaturated alloys. In a cast, brazed or welded component, many important microstructural characteristics, such as the grain size and solute redistribution, are largely determined by the details of dendrite formation and growth. Due to the importance of dendrite growth in controlling microstructure and hence mechanical integrity, understanding the underlying physics of the phenomenon has remained an ongoing challenge within the metallurgical community for several decades. Dendritic solidification is also a classic example of pattern formation in nonequilibrium dissipative systems. There exist many examples throughout nature of transformations which spontaneously generate patterns of a fixed period and, in the case of dendrites, a specific velocity of propagation. In this respect dendrite formation shares many important characteristics with such diverse problems as cellular flame fronts and Benard convection from the field of fluid dynamics and the clustering behavior of dictyostelium amoeba from the field of biology. Despite the technological and scientific interest of dendritic solidification, modeling of the process remains a formidable challenge.

The moving solid-liquid boundary inherent in any solidification problem and the complex morphological features of a dendrite render the modeling task seemingly intractable. Yet, about ten years ago it was demonstrated that the phase field method could generate realistic looking dendrites and since that time it has emerged as the method of choice for modeling solidification. The technique was originally designed to overcome the tricky numerical obstacle of front tracking by defining a function, the phase field, which varies continuously, albeit rapidly, across the solid-liquid boundary. The evolution equation of the phase field itself, when coupled with the diffusion of heat or solute, essentially recasts the moving sharp interface problem onto a more manageable finite difference solution of a set of partial differential equations. Unfortunately, early studies on the phase field model also uncovered technical limitations which need to be addressed in order that the ultimate goal – accurate modeling of dendrite growth in real alloy systems - can be successfully achieved. The first obstacle is one of numerical implementation. At low undercooling or supersaturation, there exists three important length scales in the dendrite problem each of which can differ by several orders of magnitude. To capture the low undercooling limit, a straightforward finite difference solution on a fixed grid is simply too large a task on present day computers. In recent years, several ingenious tools have been developed for successfully bridging length scales, these include, the thin interface approach, adaptive mesh refinement and the use of random walkers. All of these methods have shown unqualified success. The second hurdle encountered when applying phase field techniques to actual alloys is one of materials parameters. There are several quantities required as input to solidification modeling which are difficult and in some cases impossible to measure experimentally. Three important parameters stand out: the solid-liquid interfacial free energy, the kinetic coefficient and, in the case of alloy solidification, the liquid state solute diffusion coefficient. In addition, the microscopic solvability theory of dendrite growth demonstrates that crystalline anisotropies, even though very small, determine the steady state dendrite velocity and shape. Therefore, even more important than the actual values of the interfacial free energy and kinetic coefficient is the small directional dependences of these quantities. It is now apparent that molecular dynamics simulations using accurate descriptions of the interatomic potentials in metals can provide many of the materials parameters which are difficult to obtain in the laboratory. The purpose of the current review is to summarize the aforementioned recent advances in continuum and atomistic modeling techniques which have been developed to advance the field of dendritric solidification.

Much of the theoretical and mathematical underpinnings of the phase field model are now firmly established and the early successes of the technique are now well known. Therefore, since it is impossible to cover the entire field in the present review, we will concentrate on the latest developments of efficient numerical methods and the emerging use of atomistic simulation as a tool to provide necessary input to the dendrite growth problem. The review is organized as follows. The first section, continuum modeling, starts with a summary of the sharp interface approach and the numerous important findings generated prior to the development of phase field method. Subsequently, the basic equations and parameters of the phase field model are reviewed and the numerical challenges are discussed. Finally, techniques for overcoming the numerical difficulties are described. The second section concerns atomistic simulation approaches. Here techniques for computing diffusivities, interfacial free energies and the kinetic coefficient are outlined in detail. Particular attention is paid to the computation of crystalline anisotropies. The review concludes with a success story; an example of how results from molecular dynamics simulations can be combined with phase field techniques to predict the dendrite velocity vs. undercooling behavior for pure Ni. The modeling results, containing no adjustable parameters, are in very good agreement with experimental data.

2. Continuum Modeling

The starting point of any continuum description of dendrite growth is the diffusion equation describing the evolution of an appropriate field, temperature in the case of a pure material and the concentration field for the case of an alloy. Historically, boundary conditions were then specified at the solid-liquid boundary where the interface was assumed to be infinitely sharp. The preferred method of solidification modeling, namely the phase field model, replaces the sharp interface with a diffuse boundary and conditions valid at the evolving boundary need not be specified. Nevertheless, it is important to review results obtained from the sharp interface assumption for two reasons. First, several key findings critical to our present day understanding of dendrite growth have been obtained under the sharp interface model and second, the infinitely sharp boundary represents an important limit with which to set parameters and test the validity of various phase field formulations.

Also, in this section we shall review the thermodynamic and kinetic formulation of the phase field method. Although the method very quickly proved to be effective in overcoming the formidable numerical problem of tracking a moving interface, several problems surfaced which prevented an efficient application of the phase field method in all cases. The most notable obstacle is the presence of three very disparate length scales in the dendrite growth problem at low undercoolings. Below we will review several numerical schemes which have recently been proposed to alleviate the length scale dilemma.

2.1 Sharp Interface Models

2.1.1 *Basic Equations*

Consider the problem of dendrite solidification in a supercooled pure material. The temperature field is governed by

$$\frac{\partial T}{\partial t} = D_{th} \nabla^2 T \tag{2.1}$$

where D_{th} is the thermal diffusivity. The diffusion equation is supplemented by two boundary conditions specified at the solid-liquid interface. Conservation of heat demands that the rate of latent heat generation due to the solidifying boundary be removed by diffusion through the solid and liquid phases. The conservation law leads to a relationship for the velocity normal to the interface, V_n, given by:

$$LV_n = cD_{th}\hat{n} \cdot \left(\nabla T|_S - \nabla T|_L \right) \tag{2.2}$$

Here L is the latent heat and c_p is the constant pressure heat capacity, the two quantities given on a unit volume basis. The quantities $\hat{n} \cdot \nabla T|_{S,L}$ are the gradients in temperature normal to the interface for the solid (S) and liquid (L) phases, $\hat{n}$ is the normal vector to the interface pointing into the liquid phase. In the condition 2.2 it is assumed that c_p and D_{th} are equal in both phases, that is, the symmetric model of solidification is invoked. The second boundary condition to the dendrite growth problem in pure materials is a specification of the temperature along the interface, T_I:

$$T_I - T_M = -\frac{T_M}{L}\sum_{i=1,2}\left[\gamma(\hat{n}) + \frac{\partial^2\gamma(\hat{n})}{\partial\theta_i^2}\right]\frac{1}{R_i} - \frac{V_n}{\mu(\hat{n})} \qquad 2.3$$

where T_M is the melting temperature, the θ_i terms are the local angles between the interface normal direction $\hat{n}$ and the two local principal directions on the solid-liquid boundary and R_i denotes the two principal radii of curvature. The parameter γ is the interfacial free energy of the interface and μ is known as the kinetic coefficient. Equation 2.3 illustrates the fact that the interface undercooling, $\Delta T = T_I - T_M$, is the sum of two effects. The capillary induced undercooling, or the Gibbs-Thomson effect, yields the melting point depression due to the interface curvature and is given by the first term on the RHS in the above boundary condition. The final term is the kinetic undercooling which represents a suppression of the interface temperature due to the attachment of liquid atoms to the solid phase. Notice that Eq. 2.3 establishes an operational definition of the kinetic coefficient, it is the proportionality constant between the velocity of a planar boundary and the interface undercooling, $V = \mu\Delta T$.

In eq. 2.3 the crystallographic orientation dependence of both γ and μ have been explicitly included, as will be seen below the anisotropy of these parameters are absolutely essential to the dendrite growth problem. Nevertheless, it is of interest to rewrite the system of equations in scaled form using an isotropic value for γ. Let the dimensionless temperature field be given by $u = (T - T_M)/(L/c_p)$. Then eqs. 2.1-2.3 can be recast as:

$$\begin{aligned} \frac{\partial u}{\partial t} &= D_{th}\nabla^2 u \\ V_n &= D_{th}\hat{n}\cdot\left(\nabla u|_S - \nabla u|_L\right) \\ u_I &= -d_o\left(1/R_1 + 1/R_2\right) - \beta V_n \end{aligned} \qquad 2.4$$

where $\beta = c_p/(L\mu)$ is the scaled kinetic coefficient and $d_o = \gamma_o T_M c_p / L^2$ is known as the capillary length. To complete the basic equations of the sharp interface model of dendrite growth an initial condition must be specified in the form of a dimensionless undercooling given by:

$$\Delta = \frac{T_M - T_\infty}{L / c_p} \tag{2.5}$$

where T_∞ is the initial temperature of the melt. All of the above governing equations are valid for a pure melt, a discussion of the growth laws in the case of a binary alloy will be postponed until section 2.2.5.

2.1.2 *The Ivantsov Solution*

As alluded to in the introduction the sharp interface model is very difficult to solve numerically. The moving boundary, the complex branched morphology of the dendrite and a curvature dependent boundary condition all render the sharp interface description virtually intractable. Nevertheless, important insights into the nature of dendrite growth can be gleaned from an analytic solution obtained under a set of rather severe approximations. In 1947 Ivantsov [1] examined the problem of an isolated dendrite propagating at a constant velocity V in a supercooled liquid with initial temperature Δ. In reality a dendrite observed in a frame of reference moving with the dendrite tip does not maintain a constant shape due to the formation and growth of sidebranches. Thus, as a first approximation, Ivantsov assumed the dendrites to be free of sidebranches and the shape of the resulting "needle crystal" was taken to be a paraboloid of revolution with a radius of curvature at the tip given by ρ. A second major assumption is the neglect of both capillarity and kinetic undercooling, resulting in $u_I = 0$. In a parabolic coordinate system, the steady state diffusion equation can be solved analytically for a vanishing interface temperature and when applying the conservation of heat constraint the following relationship was found:

$$\Delta = p e^{p} E_1(p) \tag{2.6}$$

where E_1 is the exponential integral:

$$E_1(x) = \int_x^\infty \frac{e^{-x'}}{x'} dx' \tag{2.7}$$

and $p = \rho V / 2D_{th}$ is an important dimensionless parameter known as the Peclet number. Subsequent to the Invantsov work, Horvay and Cahn [2] treated the analogous problem in ellipsoidal coordinates.

The Ivantsov solution suggests that the product of tip radius and growth velocity is fixed for a specified undercooling. Unfortunately, $\rho V = const$ represents an infinite number of possible steady states whereas nature selects a unique $\rho - V$ pair from this continuum of possible solutions. Many studies since the original Ivantsov work have appeared which attempt to lift this degeneracy. Fisher (see Chalmers [3]) argued that the temperature field near the dendrite tip should be approximately that surrounding a growing sphere. By equating the radial growth rate of a sphere with the propagation velocity of the dendrite a modified $\rho - V$ relationship was found which then contained the length scale missing from the Ivantsov problem, namely the capillary length. In 1967, Sekerka et al (see Langer [4] incorporated capillarity into the solution by assuming simply that the curvature was everywhere equal to $2/\rho$. Temkin [5] retained the Ivantsov general solution, but applied the conservation of heat boundary condition only at the tip of the needle crystal. All three of the above modifications predicted a maximum in the V vs ρ relation and, at the time, it was conjectured that the operating point of the growing dendrite corresponds to the point of maximum velocity. Unfortunately, a rigorous justification for the maximum velocity hypothesis was never found. Furthermore, experimental results by Glicksman et al [6] on the transparent organic material succinonitrile clearly demonstrated that dendrite growth is not governed by a maximum velocity constraint. The authors measured independently the tip radius and velocity for various undercoolings and showed that the experimental operating point, although lying very close to the Invantsov relationship, was nearly an order of magnitude removed from the maximum velocity point predicted by the closest modified theory (Temkin).

In a series of papers Langer and Muller-Krumbhaar [7-9] examined the morphological stability of a dendrite for the case of vanishing capillarity and identified a instability in which the tip of the dendrite splits in two. In addition, it was shown that as the capillary length increases, at some point, the tip splitting behavior disappears, although amplified noise in the form of sidebranches still exist. The authors argued that if the operating point is in fact determined by stability then the criterion must reduce to the simple form:

$$\sigma = \frac{2d_o D_{th}}{\rho^2 V} = \sigma^* \tag{2.8}$$

and they further speculated that σ^* corresponds to the point of marginal stability, ie. the point where the dendrite is just stable with respect to the splitting mode. Like the maximum-velocity idea, no formal proof of the marginal stability criterion has been attempted and although the criterion has since been abandoned in favor of microscopic solvability theory, the parameter σ^* remains a useful one in the study of dendrite growth. Experiments conducted on several systems - such as ice [10-14] and succinonitrile [6, 15] – at many different undercoolings, and hence various $\rho - V$ combinations, all demonstrated that the operating point σ^* is in fact a constant. A constant σ^* when combined with the Invantsov solution provides a rough qualitative description of dendrite morphology. At large undercoolings dendrites are sharp and fast moving whereas at low values of Δ dendrites are fat and slow moving. The key remaining question then became: what determines the value of σ^* for any given system?

2.1.3 *Microscopic Solvability*

In 1974, Nash and Glicksman [16] employed a boundary element formalism to numerically determine the shape and velocity relationship for a free dendrite. In two dimensions, the integral formulation needed to describe the dendrite shape $z(x)$ is given by:

$$\Delta - d_o(\hat{n})\kappa = \frac{1}{2\pi l}\int_{-\infty}^{\infty} dx' \exp\left[\frac{z(x') - z(x)}{l}\right] K_0\left(\frac{\left\{(x-x')^2 + \left[z(x) - z(x')\right]^2\right\}^{1/2}}{l}\right) \tag{2.9}$$

Where κ is the curvature at any point on the interface, K_0 is the modified Bessel function of order zero and l is the thermal diffusion length given by $l = 2D_{th}/V$. In the absence of capillarity ($d_o(\hat{n}) = 0$) the above expression reduces to the Ivantsov solution. Nash and Glicksman solved the 3D version of eq. 2.9 for the case of an isotropic interface energy ($d_o = const$) and invoked the condition that the dendrite shape remains smooth at its tip, ie. $dz/dx = 0$ at $x = 0$. The authors then computed the shape velocity relationship with capillarity included to test the veracity of the maximum velocity selection rule.

The condition of a smooth dendrite tip turns out to be a key ingredient in establishing a velocity selection criterion. Subsequent to the Nash and Glicksman work a number of studies examined approximate models of the full time dependent dendrite growth problem. Local models [17-20] and boundary layer models [21,22] are numerically quite tractable yet manage to capture many of the essential features of dendrite formation. Results from these models indicated that for a non-zero value of the capillary length there no longer exists a complete spectrum of solution, only a discrete set of velocities yield solutions which are stable. Meiron [23] and independently Kessler [24] then examined the behavior of solutions to the full 2D growth problem, but did not force the dendrite tip to remain smooth when solving eq. 2.9. For all cases of non-zero interfacial energy, it was discovered that no solutions could be found which yielded a smooth tip. The only means of generating an acceptable dendrite shape was to incorporate anisotropy of the solid-liquid interfacial free energy through the orientation dependence of $d_o(\hat{n})$. Addition of a small anisotropy leads to a discrete family of solutions and, as was later shown [25], the only stable solution from this set is the one corresponding to the highest velocity. A compelling selection criterion, known as microscopic solvability, is then complete. The operating point of the dendrite is dictated by allowed solutions to the numerical problem and necessarily includes some degree of crystalline anisotropy.

Although microscopic solvability appears to have solved a long standing problem in the study of solidification, its experimental verification remains a formidable challenge. Since anisotropy in the interfacial free energy can not be neglected, no matter how small, experimental measures of the σ^* parameter must be accompanied by accurate measurements of the anisotropy in order to successfully validate theory. A convenient measure of the anisotropy is the parameter ε_4 which represents the relative interfacial free energies in the 100 and 110 orientations or:

$$\varepsilon_4 = \frac{\gamma_{100} - \gamma_{110}}{\gamma_{100} + \gamma_{110}} \qquad 2.10$$

(the subscript 4 refers to the four fold symmetry of the underlying crystal lattice.)
Given the difficulty of performing measurements of γ in general and the anisotropy in particular, it is perhaps not surprising that anisotropies in the solid-liquid boundary energy have been measured in just six systems. In all cases the anisotropy was found to be on the order of $\varepsilon_4 \approx 1\%$. By measuring the equilibrium shapes of liquid inclusions embedded in the crystalline solid, Glicksman and co-workers [26,27] obtained the anisotropy in both succinonitrile and pivalic acid. Mucschol et al. [28] studied the same two systems by measuring shapes of crystal particles surrounded by the liquid phase. The results for pivalic acid illustrate the difficulty in measuring the very small anisotropy as the two separate experiments yielded anisotropies which differ by a factor of two. Using the crystal in liquid method, Dougherty and Gollub [29] determined the anisotropy in NH_4Br and Oswald [30] studied the system hectaoctyloxytriphenylene. In a study of dendrite growth in ice crystals, Koo et al. [31] measured the anisotropy of the solid-liquid interfacial free energy in both the six fold symmetric basal plane and the two fold symmetric edge plane. Very recently Napolitano and Trivedi [32] were able to isolate liquid inclusions within the solid in Al-Cu alloys. By measuring the shapes of the liquid regions after quenching these authors provided the first anisotropy result for metal systems. The lack of sufficient experimental information concerning the anisotropy remains a significant hurdle to the application of continuum modeling of real systems, but as will be shown in section 3.1, atomistic simulation methods can often provide the necessary anisotropy factors.

To date there are just two complete experimental tests of solvability theory. The agreement between theory and measured dendrite growth velocities and morphologies is adequate for the case of succinonitrile, whereas experiments on pivalic acid [33-35] show substantial disagreement with the predictions of microscopic solvability. Due to the overall lack of experimental data, closure between theory and experiment remains incomplete.

An important point concerning crystalline anisotropy needs to be addressed at this juncture. Much of the early work on the formulation of the microscopic solvability idea neglected effects resulting from kinetic undercooling. As indicated by the last term in eq. 2.3, the kinetic effect is also dictated by crystalline anisotropy through the μ term. Since the anisotropy of γ plays such a central role in the dendrite shape and velocity, it is reasonable to assume that anisotropies in μ should also be important. Furthermore, there is now mounting evidence that the anisotropy in μ is about an order of magnitude larger than that of γ (see below). It is quite possible that the absence of anisotropy in the kinetic coefficient in the solvability predictions could explain the large discrepancy between theory and experiment for the case of pivalic acid. Evidence to support the notion that the anisotropy in μ may be the source of the error for PVA stems from experimental observations which show σ^* is in fact dependent on undercooling.

2.2 The Phase Field Model

2.2.1 *Basic Equations*

There exist two derivations of the basic equations of the phase field model. The original, due to Langer [36], is based on a variational form. The starting point is a phenomenological description of the free energy of the system given by the following functional:

$$F = \int dV \left[\frac{W^2(\hat{n})}{2} |\nabla \phi|^2 + f(\phi) + g(\phi) b \lambda u \right] \qquad 2.11$$

The quantity ϕ is the phase field, it characterizes the state of system at any point and varies continuously from a value of +1 in the solid phase to –1 in the liquid. (Several formulations define the limits of $\phi = 0$ for the liquid and $\phi = 1$ in the solid.) For a uniform system, that is with ϕ a constant throughout, the free energy per unit volume is given by $f(\phi)$. Traditionally, $f(\phi)$ assumes the form of a double well potential of the form:

$$f(\phi) = -\frac{\phi^2}{2} + \frac{\phi^4}{4} \qquad 2.12$$

Since the above expression possesses minima at +1 and –1, this free energy contribution alone would predict an equilibrium morphology consisting of solid and liquid regions separated by infinitely sharp interfaces. However, an energy cost for creating gradients in ϕ is embodied in the first term in the integral expression of eq. 2.11. The competition between the gradient term and the f function is a ϕ which varies continuously, although rapidly, across a diffuse solid-liquid boundary where W is a measure of the interface thickness. The final term in eq. 2.11 represents the coupling between the phase field and the temperature where the two parameters b and λ will be defined below. The g contribution, an odd function of ϕ, has the effect of lowering the minimum at $\phi = +1$ relative that at $\phi = -1$ for instances where $u < 0$, thereby driving the solidification process.

The free energy functional of eq. 2.11 is similar in spirit to other models which have been traditionally been utilized to describe phase transitions [37-39]. In fact, Langer's original development of the phase field method was based on a reformulation of the model C of Halperin, Hohenberg and Ma [40] describing critical phenomena into a model of solidification of a pure melt. Other early work on the phase field technique includes a numerical implementation by Fix [41] and an independent derivation by Collins and Levine [42]. Furthermore, the thermodynamic consistency of the variational form was verified by Penrose and Fife [43] and Wang et al. [44]who rederived the relevant equations and constraints starting from an entropy functional.

Kinetics of the phase field model require rate equations for the two relevant fields in the problem. The phase field, a non-conserved order parameter, is assumed to evolve according to the time dependent Ginzburg-Landau form:

$$\tau(\hat{n})\frac{\partial\phi}{\partial t} = -\frac{\delta F}{\delta\phi} \qquad 2.13$$

where τ is a relaxation time. The required diffusion equation describing the temperature field can be generated as follows. Let *U* be a dimensionless enthalpy given by

$$U = u - h(\phi) \qquad 2.14$$

U has been normalized by the latent heat such that when the system transforms from a complete solid phase to the liquid at $u = 0$ the change in *U* is unity. Therefore, latent heat generation places a constraint on the function *h* given by:

$$\frac{h(+1) - h(-1)}{2} = 1 \qquad 2.15$$

By performing the functional differentiation indicated in eq. 2.13 and using the definition of eq. 2.14, the following diffusion equation is obtained:

$$\frac{\partial u}{\partial t} = D_{th}\nabla^2 u + \frac{1}{2}\frac{\partial h(\phi)}{\partial t} \qquad 2.16$$

However, the above expression is valid provided

$$g(\phi) = \frac{b}{2}h(\phi) \qquad 2.17$$

This constraint fixes the value of *b*, it is a constant chosen such that the limiting behavior of *h* (eq. 2.15) is obeyed. The simplest consistent set of functions is $g(\phi) = \phi$, $h(\phi) = \phi$ and b=1.

A second derivation of the phase field equations is known as the isothermal variational form. The key feature of the isothermal version is the absence of the constraint of eq. 2.17 or, in other words, the functions *g* and *h* can be chosen independently. A functional form for *g* used in many phase fields studies is

$$g(\phi) = \phi - 2\phi^3/3 + \phi^5/5 \qquad 2.18$$

which has the distinct advantage of maintaining the minima of the free energy at the positions $\phi = \pm 1$ independent of the value of *u*. For the function *h* the simple form $h(\phi) = \phi$ has been shown to be very efficient from a computational standpoint. Although the isothermal variational form lacks the rigorous thermodynamic justification of the variational form, both versions yield identical results in the limit of a thin interface region. Hence the isothermal variation description is preferred in cases where computational requirements are severe.

The widely recognized appeal of the phase field method is the elimination of the explicit tracking of moving interfaces and the above development demonstrates how this important feature is achieved. Partial differential equations 2.13 and 2.16 can now be solved on a fixed finite difference grid and the growth of the solid region is reflected in the evolution of ϕ. In practice, the position of the solid-liquid boundary is found by computing the contour $\phi = 0$. Numerical implementation of the phase field equations typically involves an explicitly scheme with a time step chosen to insure numerical stability. Spatial derivatives are computed using standard central difference schemes. However, care must be taken when evaluating the Laplacian operator because the standard first order expression can introduce anisotropies due to the grid itself. Therefore, a second order expression which effectively removes the spurious anisotropy has been utilized [45].

Anisotropy in the solid-liquid interfacial free energy and the kinetic coefficient can be written as [46]:

$$\begin{aligned}
\gamma(\hat{n})/\gamma_o &\equiv a_c(\hat{n}) = (1-3\varepsilon_4)\left[1+\frac{4\varepsilon_4}{1-3\varepsilon_4}\left(n_x^4+n_y^4+n_z^4\right)\right] \\
\beta(\hat{n})/\beta_o &\equiv a_k(\hat{n}) = (1-3\varepsilon_4^k)\left[1+\frac{4\varepsilon_4^k}{1-3\varepsilon_4^k}\left(n_x^4+n_y^4+n_z^4\right)\right]
\end{aligned} \qquad 2.19$$

Where ε_4^k is the anisotropy, analogous to ε_4, of the kinetic coefficient and n_x, n_y and n_z are the components of the normal vector. Equations 2.19 represent a first order expansion about the isotropic values γ_o and β_o such that the four fold lattice symmetry is maintained. The coefficients of the expansion are written in a form which maintains the definition of ε_4 in eq. 2.10. The crystalline anisotropy is incorporated into the phase field method through the parameters W and τ. They are given by $W(\hat{n}) = W_o a_c(\hat{n})$ and $\tau(\hat{n}) = \tau_o a_c(\hat{n}) a_k(\hat{n})$ and the values of the prefactors will be derived in the next section. Finally, since there are no longer sharp interfaces in the phase field picture, one needs to be careful when defining the normal vector. The working definition is:

$$\hat{n} = -\frac{\nabla\phi}{|\nabla\phi|} \qquad 2.20$$

And hence the final term in eqs. 2.19 is given by:

$$n_x^4 + n_y^4 + n_z^4 = \frac{(\partial\phi/\partial x)^4 + (\partial\phi/\partial y)^4 + (\partial\phi/\partial z)^4}{|\nabla\phi|^4} \qquad 2.21$$

One of the more striking features of dendries is the emission of sidebranches starting at distances equal to few tip radii behind the advancing primary branch. It is now well accepted that sidebranches result from the amplification of noise initially located at the dendrite tip [47-51]. Noise in phase field simulations can be introduced in a qualitative fashion by randomly driving the tip [52,53] and in fact numerical noise in the simulation can provide a source of sidebranching activity. A more quantitative means of study sidebranching formation was introduced by Karma and Rappel [54] who added a Langevin noise term to both the phase field kinetic equation (2.13) and the diffusion equation for the temperature field (2.16). The noise was assumed to be uncorrelated in space and time and the specific form of the terms were chosen such that equilibrium fluctuations of the temperature and the shape of the solid-liquid interface reproduced the forms predicted from statistical mechanics considerations (a discussion of the proper form of the interface fluctuations is given in sect. 3.1). The authors demonstrated that both noise sources can be specified by a single dimensionless parameter given by $F_{ex} = k_B T_M / (\gamma d_o^2)$.

To conclude this section we note that the phase field method has been extended far beyond studies of solidification. Similar forms of the free energy functional in eq. 2.11

and the kinetic laws of eqs. 2.13 have been utilized to simulate a host of diverse materials science problems including, particle coarsening [55-57], grain growth [58-61], eutectic/eutectoid transformations [62,63], dislocation dynamics [64], faceting of solid surfaces [65], fracture [66] and domain structures in ferroelectrics [67].

2.2.2 *The Thin Interface Limit*

At this point three quantities in the phase field model remain as unknowns, W, λ and τ. Since the phase field technique is a numerically efficient means of studying the underlying sharp boundary problem defined in eqs. 2.4, it is reasonable to demand that the phase field equations reduce to the sharp boundary case in the limit of vanishing interface thickness. As shown by Langer [36] and subsequently Caginalp [68] this limit provides the link between the quantities W, λ and τ and actual materials parameters d_o and β. In particular, it can be shown:

$$d_o = a_1 \frac{W}{\lambda}$$
$$\beta = a_1 \frac{\tau}{\lambda W} \qquad 2.22$$

Where a_1 is a constant of order unity which depends on the specific functional forms chosen for $g(\phi)$. The limiting behavior including the effects of crystalline anisotropy have been investigated by Kobayashi [69] and McFadden et al. [70]. Notice that the limiting forms in eq. 2.22 do not uniquely specify all three unknowns, but only the ratios W/λ and $\tau/\lambda W$. In practice, convergence of a phase field calculation is checked by decreasing W and λ while maintaining a constant d_o, decreasing τ at constant β and verifying that the results are independent of the interface thickness.

Kobayashi [71] was the first to generate realistic dendrite structures using large scale phase field simulations at high undercooling. However, work by Wheeler et al [52] and Wang and Sekerka [72] addressed the question of convergence and uncovered a serious limitation to the phase field model as the undercooling is decreased. The problem is one of length scales, of which there are three in the dendrite problem. The smallest length scale is the capillary length. For typical pure materials d_o is on the order of nm. The second, larger scale is the microscopic scale which is on the order of the tip radius of curvature. The third and largest scale is the thermal diffusion length which is given by D_{th}/V. At high undercoolings the velocity of the dendrite is high, meaning the diffusion length is relatively small. Furthermore, at high Δ the dendrite tips are quite sharp which implies the microscopic scale is also small. Therefore, it is possible to generate a finite difference grid of mesh size ~W which can capture all three length scales. At small undercooling, a regime in which dendrites are slow moving and exhibit large tip radii, the largest and smallest length scales can differ by several orders of magnitude. The length scale problem limited initial phase field simulations of solidification to the regime $\Delta \sim 1$.

Part of the length scale dilemma can be overcome by reexamining the way in which the limit was taken in deriving eqs. 2.22. However, it is instructive to first investigate the constraints imposed by assuming a vanishing interface thickness. Notice that the variation in u across the diffuse interface varies as the interface thickness divided by the diffusion length, or $\delta u \sim WV/D_{th}$. In the vanishing thickness limit, the variation is zero or equivalently u approaches a constant. A variation in u such that $\delta u << u_I$ implies from boundary condition 4 $WV/D << \beta V$. From eqs. 2.22, this constraint can be rewritten as:

$$\frac{W}{d_o} << \frac{D\tau}{W^2} \tag{2.23}$$

The term on the RHS of the above inequality must be less than unity to insure numerical stability in an explicit numerical scheme and therefore W must be less than the capillary length. Consider now the total number of floating point operations, N_{fp}, needed to simulate dendrite growth. N_{fp} is the product of two terms: the first is the total number of grid points, a total which must capture the large thermal diffusion scale or $(D_{th}/WV)^d$ where d is the dimensionality (2 or 3) of the calculation. The second is the time needed to reach steady state which varies as $D_{th}/V^2\tau$. By recalling the definition of σ^* and the Peclet number, p, one can write the final expression as:

$$N_{fp} \sim \left[\frac{W^2}{D_{th}\tau}\right]\left[\sigma^* p^2\right]^{-(2+d)}\left[\frac{W}{d_o}\right]^{-(2+d)} \qquad 2.24$$

The first term in brackets in the above expression also appears in eq. 2.23 and the second term reflects the microscopic length scale. It is the third term which clearly illustrates the very drastic effects resulting from the vanishing interface limit constraint of eq. 2.23. Any method capable of increasing the W in a phase field simulation would dramatically improve efficiency especially in three dimensions. One such method is the thin interface limit.

Rather than study the behavior of the phase field equations in the limit of the thickness approaching zero, Karma and Rappel [46,73] argued that the important requirement is the interface width being much smaller than the thermal diffusion length and not that the thickness vanish completely. A necessary consequence of this approach is a temperature variation within the diffuse boundary region and the authors obtained the temperature field by employing a boundary layer technique. The derivation of the thin interface limit is quite lengthy and the reader is referred to ref. [46] for details. Nevertheless the main results can be stated as follows. In the thin interface limit, the first of eqs. 2.22 is unchanged, but the condition on the β term becomes:

$$\beta = a_1\left[\frac{\tau}{\lambda W} - a_2\frac{W}{D_{th}}\right] \qquad 2.25$$

Where a_2 is an additional positive constant of order unity. The second term in brackets is a direct result of the temperature variation and is the key to the improved efficiency. It is now possible to choose a larger value of W, or equivalently λ, than suggested by eq. 2.22 and still maintain the same value of β. Karma and Rappel used the thin interface results to simulate, for the first time, dendrite growth in two dimensions for a value of Δ as low as .25 and in three dimensions for $\Delta = .45$. A second advantage of the thin interface limit is the fact that by choosing $\lambda = \tau D_{th}/W^2 a_2$ the kinetic term vanishes completely. Negligible interface kinetics is physically relevant for many materials at low undercooling.

2.2.3 *Adaptive Mesh Refinement Schemes*

In solving the basic phase field equations we have thus far examined schemes which maintain a uniform finite difference grid. However, in finite element solutions of problems in heat transfer or solid mechanics a nonuniform mesh is routinely used. In regions where the temperature or stress is varying rapidly a fine mesh is generated and in those regions where the field variable varies slowly a coarse grid is established. Based on the success of finite element methods one may ask: can such a nonuniform mesh approach be utilized in the dendrite problem to overcome the disparate length scales inherent in the problem? As evidence by the work of Provatas et al. [74,75], adaptive mesh refinement schemes have been successful in treating the solidification problem.

A crucial difference between static finite element problems and the solidification case is, once again, the moving solid-liquid boundary. Although it is possible to construct a new mesh every few time steps such that the fine mesh elements are located in the vicinity of the diffuse boundary, such mesh regeneration schemes are far too inefficient. A preferred method is to refine, or unrefine, existing elements as the boundary moves. A successful numerical scheme would then involve two tasks: a technique for splitting up an element into smaller elements and a method to identify those elements which need to be refined.

To understand how a refinement scheme might work, consider the case of a uniform square array of elements in a two dimensional simulation. If a given element has been targeted for refinement, one could simply split the square into four smaller squares. This approach however, produces four additional edge nodes on the four neighboring elements. It is a nontrivial exercise to satisfy the field equation at these extra edge nodes and Palle and Dantzig [76] solved the node problem by creating additional triangular elements in all the neighboring squares. Thus, at any given time step the mesh consists of triangular and square elements and the size of the elements near the solid-liquid boundary are much smaller than the elements in the far field. In fact, in the work of Provatas, et al., the mesh refinement is so severe that the difference in size of the smallest and largest element is a factor of 2^{17}. The adaptive mesh scheme also allows for the reverse process of unrefinement, whereby smaller elements are removed as the solid-liquid interface sweeps through a given region. Although adaptive mesh refinement is capable of bridging the length scales in the solidification problem, it is not clear the technique can be extended in an efficient manner to three dimensions.

In finite element methods the gradient field, for example the heat flux, is evaluated only within an element and gradients need not be continuous between elements. However, a smoothed gradient field can be generated by projecting the element gradients to the node points. Palle and Dantzig, based on an earlier study by Zienkiewicz and Zhu [77], used the difference between the smoothed heat flux and the heat flux calculated by the finite element technique as a metric for mesh refinement. If the normalized error between the smoothed and calculated fields for a given element is larger than a certain tolerance level, then the element is refined as described above. One can easily see why the error estimation is quite effective in locating and refining elements close to the solid-liquid boundary. It is in these regions that the heat flux is varying rapidly. In fact, the sharp interface model predicts a discontinuity in the heat flux at the interface (see eq. 4).

Provatas et al. were able to successfully model dendrite growth in two dimensions for dimensionless undercoolings as low as $\Delta = .1$. Interestingly, for small undercooling, the authors noted a very long transient regime where a significant deviation between the computed tip velocities and those predicted by solvability theory was found. The discrepancy can be understood as follows. In the two dimensional simulation, crystal symmetry dictates that four dendrite tips form and grow in four orthogonal directions. As noted above, the thermal length increases as Δ decreases and if the undercooling is sufficiently small the thermal fields of the four dendrite tips begin to overlap. The transient regime then is the time needed for one dendrite to “outrun” the thermal fields of the others, a time which increases rapidly with decreasing undercooling. As microscopic solvability theory is valid for an isolated dendrite, the work of Provatas et al. does not point to a failure of theory, but does offer a cautionary tale for simulations which seek to investigate the small undercooling limit.

2.2.4 *The Random Walker Technique*

Adaptive mesh refinement resolves all length scales in the problem using a consistent numerical procedure. Another possibility is to separate the entire computational space into just two regions of small and large length scales. The thin interface limit analysis offers an effective means to help bridge the gap between the small capillary length and the larger microscopic length in the dendrite solidification problem. There remains however the large difference between the thermal diffusion length and the length scale associated with the tip radius. At very low undercooling these scales can differ by many orders of magnitude. In any phase field simulation the function ϕ varies rapidly only near the diffuse boundary and is a constant (± 1) far from the interface. In these distant regions the only relevant field is the temperature and the diffusion equation given in eq. 2.1 is valid. Thus, a possible approach for bridging length scales would be a scheme which couples an efficient means of solving the slowly varying temperature field in a region far from the boundary with a phase field approach for the inner region. Such an idea has been carried out by Plapp and Karma [78,79].

The inner, smaller length scale, domain in the Plapp-Karma scheme contains the solid-liquid interface and is solved using the phase field model on a fine finite difference mesh as described above. The outer domain is solved by the method of random walkers. Walkers are discrete points in space and each can be viewed as containing a certain amount of heat. As solidification proceeds the positions of all the walkers change and to update an individual walker a new position is randomly selected with a probability distribution given by:

$$P(\mathbf{r}',t' \mid \mathbf{r},t) = \frac{1}{\left[4\pi D_{th}(t'-t)\right]^{d/2}} \exp\left[-\frac{|\mathbf{r}'-\mathbf{r}|^2}{4D_{th}(t'-t)} \right] \qquad 2.26$$

Here $\mathbf{r}$ and $\mathbf{r}'$ are the old and new positions of the walker respectively and $t'-t$ is the time increment between updates. The greatly improved efficiency of the random walker approach stems from the fact that walkers far from the interface are updated less frequently and are allowed to move further than the walkers close to the inner domain. In a sense, the random walker algorithm acts as a variable mesh size finite element approach without the need to continually update a mesh.

To merge the two computational domains Plapp and Karma specify how walkers are created and destroyed in the transition region. Net changes in the number of walkers are handled by a coarse grid of "conversion cells" located at the transition between the outer and inner domains. The grid of conversion cells can be superimposed on the finer phase field grid. The temperature of a conversion cell is related to the density of walkers in the cell by:

$$u_{cc} = -\Delta(1 - m_i(t)/M) \qquad 2.27$$

Where m_i is the density of walkers in cell i and M is a constant integer. Definition 2.27 dictates that an empty cell corresponds to the initial state ($u = -\Delta$) and a conversion cell with M walkers is equivalent to $u = 0$. The temperature in the conversion cells satisfies one boundary condition between the inner and outer domains, another condition which must be met is a balance of heat flow. Let $Q_i(t)$ be a reservoir variable describing the heat content of conversion cell i. At each time step in the simulation the phase field inner solution yields the amount of heat that flows into or out of the conversion cells and this amount can be added to Q_i. Then if the updated value of Q_i is greater than some critical value Q_c a walker is added to conversion cell i and Q_c is subtracted from the reservoir. On the other hand if Q falls below -Q_c a walker is removed and Q_c is added to the cell reservoir. The above algorithm ensures that the addition and subtraction of walkers occurs at a rate proportional to the local heat flow and thus heat is conserved.

The hybrid phase field – random walker scheme appears to be the most efficient means of computing dendritric solidification at this time. Despite the fact that a large number of walkers were employed (5x10^6) in the calculation, the authors found that the far field temperature profile could be computed with virtually no extra cost. That is, most of the computer time was devoted to solving the inner region. Plapp and Karma were able to simulate dendrite growth in three dimensions for a very low undercooling of $\Delta = .05$. An interesting result of the study was the observation that σ^* reaches a constant value very soon after the dendrite arms have formed. The individual contributions, ρ and V, evolve much more slowly consistent with the findings of Provatas et al.

2.2.5 *Binary Alloys*

As in the pure material case, the logical starting point for a discussion of dendrite formation in alloys is the sharp interface limit. Langer [4] has emphasized that there exists an exact analogy between the set of eqs. 4 and the governing equations of alloy solidification. If $\tilde{\mu}$ represents the deviation of the chemical potential of solute atoms in solution from the equilibrium value at some specified temperature, then the diffusion equation of eq. 1 becomes

$$\partial\tilde{\mu}/\partial t = D_L \nabla^2 \tilde{\mu}; \quad \partial\tilde{\mu}/\partial t = D_S \nabla^2 \tilde{\mu} \qquad 2.28$$

where diffusion in both the solid and liquid phases has been included and D_L and D_S are the corresponding chemical diffusion coefficients. Notice only the chemical field is relevant here. Since the diffusion of heat is much faster than the rearrangement of solute atoms ($D_{th} >> D_L$), it is justified to assume an isothermal system at some specified temperature. Similarly, in simulations of forced velocity solidification within a temperature gradient it is valid to invoke the frozen temperature approximation, meaning the temperature gradient remains fixed at all times. The equivalent of the latent heat boundary condition becomes

$$V_n \Delta c = \hat{n} \cdot \left[M_S \nabla c|_S - M_L \nabla c|_L \right] \qquad 2.29$$

where M are mobilities and Δc is the difference between the equilibrium concentration in the liquid phase and that of the solid phase at the temperature of interest, or equivalently, Δc is the length of the equilibrium tie line in the solid-liquid two phase region of the alloy phase diagram. The above condition relates the velocity to the rejection of solute at the solidification front in an analogous fashion to the rejection of latent heat in a pure melt. The rejection of solute at dendrite tips eventually leads to a nonuniform solute distribution in the final microstructure of cast alloys. The final boundary condition is then:

$$\tilde{\mu}_I = -d_o\left(1/R_1 + 1/R_2\right) - \beta V \qquad 2.30$$

where d_o is now the chemical, rather than thermal, capillary length (to be defined below) and again βV is the kinetic undercooling. Finally, the equivalent of the dimensionless undercooling from the pure case, is the dimensionless supersaturation which can be written as:

$$\Omega = \frac{c_l^o - c_\infty}{c_l^o(1-k)} = \frac{c_l^o - c_\infty}{\Delta c} \qquad 2.31$$

Here k is the equilibrium segregation coefficient defined by $k = c_s / c_l$ where $c_s(c_l)$ is the solid (liquid) concentration at the interface and c_l^o is the equilibrium concentration in the liquid. The initial concentration of the system is denoted by c_∞.

Unlike the pure melt case, in alloys it is no longer appropriate to assume equal diffusivities in the solid and liquid phases. For typical alloys, the ratio of chemical diffusivities D_c^S / D_c is on the order of 10^{-4} at the melting point and hence the symmetric model of solidification is entirely unacceptable. However, the general non-symmetric model presents special problems when applying a phase field method of solution. Since ϕ varies continuously across a solid-liquid interface, one must also specify a ϕ dependent diffusivity which yields $D = D_S$ in the limit $\phi = 1$ and $D = D_L$ for the liquid phase ($\phi = -1$). Many forms for the dependence of D on the phase field have been utilized to date but, as will be discussed below, when applying the thin interface limit the optimal choice of the functional form is by no means trivial. A second problem in the phase field adaptation to the alloy case is the use of chemical potential fields. The analogy between the alloy and the pure material case is instructive, however in practice it is often more desirable to solve for the experimentally accessible concentration field rather than the chemical potential. The conversion from chemical potential to concentration depends on the free energy functional chosen in the phase field formulation and, in general, results in a nonlinear diffusion equation even in the far field limit.

Pioneering theoretical work on the phase field formulation of alloy solidification was provided by Wheeler, Boettinger and MacFadden [80,81] and Calginalp and Xie [82]. Warren and Boettinger [53] generated realistic dendrite morphologies in two dimensions, complete with sidebranching behavior and microsegregation, for a phase field simulation using parameters appropriate to the Cu-Ni system. The authors employed a regular solution model to describe the themodynamics and investigated dendrite morphologies for two ratios of diffusivities, $D_S / D_L = 1.\text{x}10^{-4}$ and $1\text{x}10^{-1}$. Warren and Boettinger found good agreement with the sharp interface, Ivantsov prediction provided the finite difference grid spacing was sufficiently small. The Cu-Ni phase field model was later modified [83] to examine growth morphologies and solute redistribution during recalesence. The phase field model was modified such that a constant rate of heat removal could by applied to the entire system. Finally, Boettinger and Warren [84] investigated the case of forced velocity solidification starting from an initially flat solid-liquid boundary. Results were compared to the Mullins-Sekerka [85] instability prediction and solute trapping as a function of interface velocity was compared to the model of Aziz [86].

To date, phase field simulations of binary alloy solidification have been plagued with the same constraint as in the early work on modeling of pure melt solidification. That is, they have been limited to the high supersaturation range. For example, the Warren and Boettinger Cu-Ni study was performed at $\Omega = .85$. In addition, for numerical efficiency considerations the value of the kinetic coefficient chosen was about a factor of 100 too small. Based on the preceding discussion, the obvious starting point in extending the range of supersaturation is the thin interface limit idea. However, for the non-symmetric model the limit produces serious difficulties. In the pure melt case, the phase field model predicts a smooth variation of the temperature across the solid-liquid boundary and, for equal diffusivities in both phases, the flux of heat is proportional to the gradient in the temperature variation. In this symmetric case it is possible to satisfy both the continuity of temperature and the latent heat boundary condition (eq 4) in the limit of a thin interface. In the binary alloy case, the flux of solute is no longer proportional to just the gradient in concentration across the boundary, but is the product of the gradient and a diffusivity, a diffusivity which is itself varying rapidly in the diffuse interface region. For a general choice of the $D(\phi)$ it is no longer possible to satisfy all of the sharp boundary equations when reducing to the thin interface limit and specifically a jump in chemical potential across the interface is obtained. In an important paper, Almgren [87] has shown that two additional complications arise in the thin interface analysis: an interfacing stretching correction and a surface diffusion artifact appear in the latent heat boundary condition.

Karma [88] has demonstrated how it is possible to choose functions of the phase field model such that the sharp interface equations of the non-symmetric model are reproduced in the thin limit. To understand the analysis it is convenient to examine the simple case of a dilute binary alloy. In the dilute limit where ideal solution thermodynamics is appropriate, the following set of sharp interface equations can be derived:

$$\begin{aligned} &\frac{\partial c}{\partial t} = D_L \nabla^2 c \\ &c_l(1-k)V_n = -D_L \hat{n} \cdot \nabla c\big|_L \\ &c_l / c_l^o = 1-(1-k)d_c\left(1/R_1 + 1/R_2\right) \end{aligned} \qquad 2.32$$

Notice, in the above set of equations the solid diffusivity has been set to zero and no diffusion equation or solute flux through the solid is considered. The case $D_S = 0$ is often referred to as the one sided model. Also, in the dilute limit the chemical capillary length is given by:

$$d_0 = \frac{\gamma T_M}{Lm(1-k)c_l^o} \tag{2.33}$$

where m is the slope of the liquidus line on the equilibrium phase diagram.

Cast into a phase field formulation, the sharp interface relations for a dilute alloy can be written as follows. The evolution of the phase field obeys:

$$\tau \frac{\partial \phi}{\partial t} = W^2 \nabla^2 \phi - f'(\phi) - \frac{\lambda}{1-k} g'(\phi)\left(e^{\tilde{\mu}} - 1\right) \tag{2.34}$$

where the primes denote differentiation with respect to the argument. Equation 2.34 is similar to the phase field description of pure melt solidification, the important difference being the exponential dependence of the chemical potential term rather than a linear dependence with temperature (eq. 2.11). In this case the conversion of the chemical potential field to the concentration reads:

$$\tilde{\mu} = \ln\left[\frac{2c/c_l^o}{1+k-(1-k)h(\phi)}\right] \tag{2.35}$$

The diffusion equation is the usual continuity equation:

$$\frac{\partial c}{\partial t} = +\nabla \cdot j = 0 \tag{2.36}$$

Combined with an expression for the flux given by:

$$j = -Dcq(\phi)\nabla\tilde{\mu} - aWc_l^o(1-k)e^{\tilde{\mu}}\frac{\partial}{\partial t}\left(\phi\frac{\nabla\phi}{|\nabla\phi|}\right) \tag{2.37}$$

Two contributions to the flux are unique to the problem at hand. First, the function $q(\phi)$ is the as yet to be determined dependence of the diffusion coefficient on the phase field. All that is known at this point is the function must vanish for the solid (=1) and reproduce the liquid diffusivity for (=-1). The second important contribution is the last term of eq. 2.37 which originated with the work of Karma. It represents a solute current from the liquid to the solid along a direction normal to the interface (see eq. 2.20) and is nonzero only in the diffuse boundary region. The extra flux, known as the anti-trapping current, is designed to counteract the presence of a jump in chemical potential arising from the thin interface limit of the non-symmetric model. Furthermore, Karma showed that a proper choice of the constant a in eq. 2.37. along with specific choices for the functions g and h can force all three unwanted interface corrections to vanish simultaneously. Again, we need not present the details of the asymptotic analysis but can summarize the key findings. Results for W, τ and λ remain identical to the symmetric model findings of eqs. 2.22 and, consequently the kinetic term can be made to vanish. Also, the function h can again be chosen as $h(\phi) = \phi$. To eliminate the chemical potential jump, the interface stretching effect and the surface diffusion contribution, q can be chosen to be:

$$q(\phi) = \frac{1-\phi}{1+k-(1-k)h(\phi)} \qquad 2.38$$

and the constant a is fixed at $a = 1/\left(2\sqrt{2}\right)$.

Since the thin interface limit performs well in pure melt simulations, it should come as no surprise to find that the above results are also a significant improvement in numerical efficiency. To demonstrate the improvement, the Karma model can be compared to the more standard choice of functions, that is, no anti-trapping current (a=0) and $q(\phi) = (1-\phi)/2$. Simulations were performed using $\varepsilon_4 = .02$, $k = .15$ and a scaled supersaturation of $\Omega = .55$. To test the thin interface limit scheme the concentration along the central axis of the dentrite was compared to the Gibbs-Thomson prediction of $c_s(x)/c_l^o = k[1-(1-k)d_o/\rho]$. Karma found that the results of the thin interface implementation agree to within a few percent of the theoretical result for a small ratio of d_o/W. On the other hand, the standard model is not well converged even with a larger d_o/W. Clearly, the thin interface analysis demonstrates that quantitative predictions of dendrite growth are now possible for binary alloys.

3. Atomistic Simulations

Numerical implementation of the phase field model has progressed to the point where realistic dendrite morphologies can be generated for a wide range of undercooling or supersaturation. The next logical step in the modeling process is the quantitative prediction of solidification behavior in real materials. Utilizing the phase field approach as a predictive tool requires the specification of several material properties. Many parameters are readily available in the experimental literature – for example, the latent heat or the thermal diffusivity – others, however, are not. For these difficult to measure quantities, atomistic simulations can provide useful information. In this section we review how molecular dynamics (MD) methods and Monte-Carlo (MC) simulations can be employed to compute three necessary input parameters: the solid-liquid interfacial free energy, the kinetic coefficient and the chemical diffusivity in the liquid.

The accuracy of materials parameters derived from simulation depends, of course, on how accurately the interatomic potential can capture the physics of bonding in the material. Most of the work to be presented below has employed the embedded atom method (EAM). Developed in the mid 1980's [89,90], the EAM is a semi-empirical potential which includes, in a simple way, many body effects. EAM potentials have been proven to be quite successful in reproducing various thermodynamic, structural, kinetic and defect properties of several noble and late transition metals [91]. The original EAM potentials developed by Foiles, Baskes and Daw (FBD) [92] used as fitting parameters known properties of only the crystalline phase, however, Foiles [93,94] subsequently showed that the potentials also predict quite well the structure and thermodynamics of the liquid phase as well. Since the original FBD work a number of potential fitting schemes have appeared in the literature. Potentials discussed in this section include the Voter-Chen (VC) [95] scheme and the force matching procedure introduced by Ercolessi and co-workers [96,97].

3.1 The Solid-Liquid Interfacial Free Energy

In 1950, Turnbull [98] measured the solid-liquid interfacial free energy in a variety of pure metals by observing the maximum undercooling achieved by the liquid and comparing the result with predictions from classical nucleation theory. Since that time many experimental measures of γ have been conducted and a fairly large database has been established (see, for example, Jones [99]). From the point of view of solidification modeling the value of γ is not critical. In the aforementioned Turnbull study, it was found that the solid-liquid interfacial energy is proportional to the latent heat. The interfacial energy enters the solidification problem through the capillary length but it always appears in the ratio γ / L and, as it turns out, d_o is nearly a constant for all materials. As suggested by the microscopic solvability predictions, a much more important quantity is the anisotropy of γ and here the experimental data is more scarce (see sect. 2.1.3). Because of the precision required to extract the very small anisotropy experiments are quite difficult to perform and, as will be seen below, atomistic simulations can provide useful insights.

Atomistic computations of the solid-liquid interfacial free energy originated with the work of Broughton and Gilmer [100] on the Lennard-Jones system. The authors employed lambda integration techniques combined with an imposed cleaving potential. Use of a cleaving potential allowed for a four step process which: cleaved the bulk solid and liquid, replaced one side of the separated solid portion with liquid and recombined the solid-liquid system by removing the applied potential. The reversible work for the entire process yields the work required to form a solid-liquid interface of a given area. Broughton and Gilmer computed γ for the 100, 110 and 111 orientations and noted that extreme care must be taken in choosing the mathematical form of the orientation dependent cleaving potential. In dimensionless units, the interfacial energies were found to be $\gamma_{100} = .34 \pm .02$, $\gamma_{110} = .36 \pm .02$ and $\gamma_{111} = .35 \pm .02$. Due to the uncertainty of the simulation results, no anisotropy could be derived. Davidchack and Laird [101] used a modified Broughton-Gilmer scheme to calculate the solid-liquid interfacial free energy in the hard sphere system and they found $\gamma_{100} = .62 \pm .01$, $\gamma_{110} = .64 \pm .01$ and $\gamma_{111} = .58 \pm .01$ in reduced units. Although the Davidchack and Laird result represents the first reliable value of γ in this much studied model system, the uncertainty is still too high to accurately fix the anisotropy. Density functional theory [102-104] approaches offer a promising means of theoretically computing γ, however, results of various studies on the hard sphere system show considerable discrepancy [105]. The work of Curtin [106], who employed a weighted density approximation [107], is considered to be the most accurate model as it predicts a hard sphere interfacial energy close to that found from simulation. Curtin did find a small anisotropy between the two interfaces studied, 100 and 111, but the uncertainty of the results are unclear considering the assumptions invoked. What is needed is a simulation method which is capable of resolving the small anisotropy and such a method has been developed by Hoyt, Asta and Karma [108].

Consider a thin solid-liquid system with the direction x running along the interface and let the length in x be denoted by W. Furthermore, let the system be infinite in the direction perpendicular to the boundary and let b be the thickness of the system with $b << W$. If $\xi(x)$ represents the height of the interface, then the energy of this system can be written as:

$$E = b\int ds\gamma(\theta) = b\int dx\gamma(\theta)\sqrt{1+(d\xi/dx)^2} \qquad 3.1$$

At the melting temperature the amplitude of fluctuations in the interface position are small such that the following approximations can be used $ds \approx 1+(d\xi/dx)^2/2$ and $\theta \approx d\xi/dx$. Also, let the interface height function be expressed as the sum of Fourier modes according to:

$$\xi(x) = \sum_k A(k)\exp(ikx). \qquad 3.2$$

With the above assumptions and definitions the energy per Fourier mode E_k can be derived:

$$E_k = bW(\gamma + \gamma")|A(k)|^2 k^2 \qquad 3.3$$

where $\gamma" \equiv d^2\gamma/d\theta^2$ and is the same term which appears in eq. 2.3. The principle of equipartition of energy states that the mean energy per Fourier mode must be equal to k_BT_M (that is 2 degrees of freedom per mode corresponding to $\cos(kx)$ and $\sin(kx)$). Therefore, the desired result can be written as:

$$<|A(k)|^2> = \frac{k_BT_M}{bW(\gamma+\gamma")}\frac{1}{k^2} \qquad 3.4$$

Equation 3.4 above is the starting point for the fluctuation spectrum method for determining the solid-liquid interfacial free energy and its anisotropy. The sum $\gamma + \gamma"$ is known as the interface stiffness and it is important to note that it is this quantity and not γ itself which controls the amplitude of fluctuations.

The result of capillary theory, eq. 3.4, has been used frequently in the past to study various interface properties. For example, Bartelt et al. [109] derived surface mass diffusion coefficients by monitoring fluctuations in surface steps during Monte-Carlo simulations, Hapke et al [110] employed molecular dynamics simulations to compute the surface tension in polymer films and Le Floc'h et al [111] examined the roughening transition of anti-phase boundaries for the ordered phases L12 and DO3, but in each case an isotropic interfacial energy was assumed. The real power of the fluctuation spectrum method is its ability the resolve very small anisotropies, as can be seen from the following simple example. Consider an orientation dependence of γ given by:

$$\gamma = \gamma_o[1 + \varepsilon_4 \cos(4\theta)] \qquad 3.5$$

Where γ_o is an average interfacial energy and ε_4 is again a measure of the four fold anisotropy and is on the order of .01. We shall denote by 100[010] a solid-liquid system that is oriented with the [100] crystal direction normal to the interface and [010] coincides with the *x* direction. The stiffness for the 100[010] case is $\gamma_o(1+15\varepsilon_4)$. On the other hand, if the orientation is such that 110 is the interface normal and $1\bar{1}0$ is the direction along the interface, or $110[1\bar{1}0]$, the stiffness is $\gamma_o(1-15\varepsilon_4)$. The large factor multiplying ε_4, and the change of sign, for the different orientations illustrates that the anisotropy in the stiffness is about one order of magnitude larger than that of γ alone. By monitoring the fluctuations in the solid-liquid boundary during MD simulations for several orientations, the large variation in stiffness can be obtained and, by parameterizing the interfacial energy as in eq. 3.5, the anisotropy in γ can be precisely determined.

The fluctuation spectrum method requires a means of accurately locating the solid-liquid interface as a function of *x*. The first step in extracting the interface position is distinguishing a given atom as belonging to either the solid or liquid phase. In the past several methods have been proposed to identify atoms in the crystalline phase vs. those in topologically disordered regions [112-115]. For the fluctuation spectrum technique, Hoyt et al. defined an order parameter ϕ for the atom *j* as

$$\phi_j = \frac{1}{12}\sum_i \left|\mathbf{r}_i - \mathbf{r}_{FCC}\right|^2 \qquad 3.6$$

where the sum runs over the twelve nearest neighbors of a given atom, $\mathbf{r}_i$ is the position of each neighbor measured from the atom in question and $\mathbf{r}_{FCC}$ are the positions of the neighbors for the ideal FCC crystalline lattice in the specified orientation. The second step in locating the boundary position is a coarse graining procedure. Dimensions of a typical MD simulation for the 100[010] orientation consisted of b=3 unit cells and W=64 unit cells. The length in the direction normal to the interface, the y direction, was approximately 128 unit cells and two interfaces are present in the periodic cell. Similar dimensions were utilized for other crystal orientations and the total number of atoms range from 100,000-150,000. The x direction of the total cell was divided into several slices corresponding to the number of desired k points and similarly the y direction was divided into slices whose width was approximately an interatomic spacing. The average order parameter, denoted ϕ, was then computed by summing the individual order parameters over all the atoms in each of the smaller cells in the system. For a given x position, the function ϕ vs. y is as shown in fig. 3.1a where large (small) values of ϕ signify the liquid (solid) portion of the system. The data of fig. 3.1a was collected from one configuration of the simulation of pure Ni using the EAM potential developed by Foiles, Baskes and Daw. The abrupt, nearly factor of five change in ϕ precisely pinpoints the two solid-liquid interface locations and in particular the contour $\phi = .7$ was used as the defining position. By repeating the procedure of fig. 3.1a across the entire x range, the full height function can be generated. Figure 3.1b shows the interface position over a portion of the total cell as determined by the procedure just described (the heavy solid line) superimposed on the actual atom positions. The atoms in the figure were shaded based on the individual ϕ_j values; $\phi_j < .7$ are shaded gray and correspond to solid atoms whereas values greater than .7 are white, liquid atoms. It is clear from these results that the interface tracking method is capable of accurately resolving small amplitude fluctuations.

Figure 3.2 shows the mean square Fourier amplitude vs. k on a log-log scale for three different crystal orientations of pure Ni. Averages were generated from snapshots taken every .2*ps* (the time step was 2*fs*) for a total of 125*ps* in an MD run in the microcanonical ensemble. In the figure, the solid lines indicate a slope of –2 and it is clear that the correct functional dependence with k as predicted by the capillary result of eq. 3.4 is reproduced over a wide range of wavenumbers. The offset of the three curves in fig. 3.2 reflects the anisotropy in the stiffness for the three orientations. The anisotropy can be more clearly in fig. 3.3 which plots the reciprocal of the power spectrum vs. k^2. The slopes of the lines in the figure are proportional to the stiffness and the large between the 100[010] and $110[1\bar{1}0]$ orientations, as discussed above, is evident. Hoyt et al. used the three stiffness values to generate three parameters, γ_o, ε_4 and δ, of the following expansion for the interfacial free energy:

$$\gamma(\hat{n})/\gamma_o = 1 - 3\varepsilon_4 + 4\varepsilon_4 \sum_{i=1}^{3} n_i^4 + \delta\left(\sum_{i=1}^{3} n_i^6 + 30 n_1^2 n_2^2 n_3^2 \right) \qquad 3.7$$

The final term, absent in most phase field formulations, is a small correction which allows one to predict the interfacial energy of any orientation. The predictive power of eq. 3.7 was tested on two other orientations, 100[012] and $110[1\bar{1}2]$, and the simulated stiffnesses agreed almost exactly with the γ expansion. From eq. 3.7 the authors were able to determine a γ_o value of 326 mJ/m^2 and an anisotropy between 100 and 110 of 1.8%.

Subsequent to the Hoyt et al. work on Ni, the fluctuation spectrum method has been applied to the EAM metals Cu, [116] Au, Ag, [117], Pb [118] and Al [119]. Figure 3.4 shows $1/bW\left\langle |A(k)|^2 \right\rangle$ vs. k^2 for the case of Cu and fig. 3.5 shows a log-log plot of $\left\langle |A(k)|^2 \right\rangle$ vs. k for pure Au. The stiffness vs. orientation dependence is qualitatively the same as for Ni, although in the case of Au the stiffnesses of the 100[010] and 110[001] orientations are nearly equivalent. Results for all the elements studied to date are summarized in table I. Three materials parameters are listed, the melting point predicted by the EAM potential, γ_o and the 100/110 anisotropy. Numerical values in parenthesis refer to experimental results where available. Three separate potentials for Ni were investigated, the original FBD form, the Voter-Chen (VC) description and the most recent, potential developed by Angelo, Baskes and Moody (ABM) [120]. Although the VC and FBD potentials predict a melting point reasonably close to the known value, the ABM model does not. Also, the value of γ_o varies nearly linearly with the melting point, a result not unexpected based on the Turnbull correlation between interfacial energy and latent heat and the fact that L is proportional to T_M for most materials. The experimental data for γ_o given in parenthesis (the first entry for the case of Au and Pb) are the results of the undercooling experiments performed by Turnbull. The agreement with the simulated results is fair at best, but the comparison with the Turnbull data is suspect for two reasons. First, it is well known that the Turnbull values are consistently low, in fact, Jiang et al [121] argue that the correct interfacial energy is about 46% higher than that quoted by Turnbull. The second reason for not placing too much emphasis on the comparison with experiment is the melting point deviation as noted above. In the case of Pb, which was modeled using the Lim, Ong and Ercolessi [97] potential, the melting point agrees quite well with experiment and the solid-liquid interfacial free energy agrees within a few percent of an experimental value [122] other than the Turnbull estimate. A large discrepancy however, exists between computed and experimental [122] interfacial free energy in the case of Au. From the point of view of solidification modeling it is the final column, the anisotropy, which is most critical. Here we see values consistently around the 1.5% level.

3.2 The Kinetic Coefficient

Unlike the solid-liquid interfacial free energy there are no measurements whatsoever of the kinetic coefficient nor its anisotropyand atomistic simulations have proven invaluable in establishing reliable estimates for μ and its orientation dependence. The complete lack of experimental data has lead some phase field investigations [80,81,123] to assume a kinetic coefficient based on the model of Coriell and Turnbull [124]. However, the Coriell and Turnbull result represents only an upper limit to the growth velocity and MD simulations have since shown the estimate to be a factor of 4 or 5 too high. On the other hand, the model of Broughton, Gilmer and Jackson [125,126] predicts the growth velocity vs. undercooling using rate theory arguments and, in section 3.2.4, we will demonstrate that the BGJ model is an adequate description of the kinetic coefficient in the 100 and 110 growth directions.

The fluctuation spectrum method appears to be the ideal simulation technique for extracting the small anisotropy in γ. However, there exists several techniques capable of determining the kinetic coefficient from MD simulations and each falls into one of three broad categories. Forced velocity simulations impose a specified velocity on each atom in the system and the temperature at the interface is then recorded. By contrast, free solidification runs impose a fixed undercooling everywhere and monitor the rate at which the solid-liquid boundary advances. Forced velocity and free solidification schemes compute μ by determining the velocity vs. undercooling relationship, however, techniques which monitor the fluctuations in the position of the interface provide a means of obtaining μ precisely at the melting point. In this section we will review each of above mentioned techniques, but a more detailed review can be found in ref. [127].

3.2.1 Forced Velocity Simulations

Broughton, Gilmer and Jackson [125] (see also ref. [126]) were the first to employ atomistic simulations to the study of crystal growth rates. These authors studied the solidifcation kinetics in the Lennard-Jones system for both the 100 and 111 crystal orientations. Simulation cells in the BGJ technique consist of three regions aligned along the z direction. A large central region, referred to as the dynamic region, contains the solid-liquid boundary and has no temperature control. A thin region at the bottom of the cell is the static liquid region and contains a heat bath which controls the temperature at some temperature below the melting point. Similarly a static solid region is positioned at the high z end of the cell and again a heat bath maintains the same temperature as the lower heat bath. At each time step, δt, in the simulation, the numerical solution to Newtons equations of motion are supplemented by a displacement of all atoms in the z direction, ie. from bottom to top of the cell, by an amount $V\delta t$. Since the entire system translates at constant velocity, atoms which move beyond the top solid region are annihilated from the system and are replaced by liquid atoms in the lower region. During the simulation the x and y dimensions of the cell are held fixed such that the zero pressure crystalline lattice parameter is maintained and zero pressure in the z direction is fixed by dynamically changing the total cell length during the MD runs.

The BGJ method involves choosing both the temperature of the heat baths and an imposed velocity. The undercooling for a given velocity is found by monitoring the temperature at the interface during the run. To accurately compute the average interface temperature the imposed velocity must be varied, by trial and error, such that the solid-liquid boundary remains stationary in approximately the center of the dynamic region. BGJ performed simulations over a wide range of temperatures from just under the melting temperature ($T_M \approx .61$ in reduced units for the Lennard-Jones system) to temperatures below .1. An important result of the BGJ study was the observation of a significant crystallization rate even at very low temperatures where the liquid diffusivity is known to be negligibly small. The BGJ results contradict an earlier model of growth kinetics due to Wilson [128] and Frenkel [129] who proposed that crystallization is a thermally activated process with diffusion being the rate limiting step at low temperatures. The modification of the Wilson-Frenkel model proposed by BGJ will be discussed in the section 3.2.4.

In a more recent work, Celestini and Debierre [130] performed forced velocity MD simulations, similar to a zone refining process, capable of extracting the velocity vs. undercooling behavior. In the Celestini approach two solid-liquid interfaces are established and a fixed velocity is imposed in a direction z perpendicular to the boundaries. Four temperature baths I, II, III and IV are established along z. Regions I and II are maintained at a temperature below the melting point and thus the region

$z_I < z < z_{II}$ is entirely solid phase. Similarly, baths III and IV are maintained at $T > T_M$ with all liquid phase between. The liquid region is located in the center of the cell and periodic boundary conditions (and constant volume) are utilized such that a solid atom leaving the high z side subsequently appears in the solid at the low z end. The temperature baths are very thin (10-20Å) and temperature is controlled via. explicit velocity rescaling. In between the solid and liquid thermostats, ie. between regions I and IV and also, II and III, there exist large temperature gradients. The two solid-liquid boundaries are found in these regions, one region being the melting interface and the other is the solidifying front. Steady state, that is a constant temperature profile and two stationary interfaces, is achieved after a few complete passes of the liquid zone over the entire length of the sample.

An advantage of the Celestini-Debierre technique over the BGJ method is that any velocity can be imposed and the two interfaces adjust along the z direction and within the temperature gradients until the proper interface temperature is maintained. A comparison of the steady temperature profile and the boundary positions establishes the velocity-undercooling relationship. In other words, a search for that velocity which renders the interfaces immobile is not necessary. The authors originally applied their technique to the study of solute segregation as a function of velocity in a Lennard-Jones binary system and they demonstrated good agreement between simulation results and the segregation model proposed by Aziz [86]. However, in a later study [131] the authors have extended their technique to the case of pure Au modeled using interatomic potentials of the embedded atom type. It was found that the velocity-undercooling relationship is in excellent agreement with that obtained via a free solidification procedure as described below.

3.2.2 Free Solidification Simulations

The free solidification technique involves a solid-liquid system with periodic boundary conditions equilibrated at the melting temperature. Initially the system contains a small volume fraction of solid. An atomistic picture of the starting point system is shown in fig. 3.6. The system is then "quenched" to some specified undercooling and allowed to solidify. During the MD run the latent heat generated is removed everywhere in the system by various established thermostat methods (Nose-Hoover, Langevin dynamics, etc.). The position of the interface vs. time is monitored most easily by tracking the total potential energy of the system as described in detail in ref. [132]. Finally, due to the density difference between solid and liquid, constant volume simulation leads to a gradual build up of pressure during crystallization which eventually halts soldification. Instead, constant pressure conditions are required with the pressure maintained at zero throughout the run.

The free solidification method has been applied to the study of crystallization kinetics in Cu and Ni [132] and Au and Ag [117] using the EAM. Velocity vs. undercooling behavior using the free solidification analysis has also been used by Briels and Tepper [114] in their study of crystallization in the Lennard-Jones system and by Tymczak and Ray [133] in an MD investigation of Na. An example of velocity-undercooling results from the free solidification method is shown in fig. 3.7. The data, reproduced from ref. [117], are results from EAM Au and three low index growth directions are depicted, 100, 110 and 111. The slopes of the heavy solid lines in the figure are a measure of the kinetic coefficient. For Au, and for all EAM systems investigated thus far, the ratio μ_{100} / μ_{110} is found to be approximately $\sqrt{2}$. The ratio is also the ratio of interplanar spacings in an FCC crystal and the significance of this equality will be discussed in the section 3.2.4. It should also be noted that the $\sqrt{2}$ factor represents a fairly large anisotropy ($(\mu_{100} - \mu_{110})/(\mu_{100} + \mu_{110}) = .17$) and is an order of magnitude larger than the anisotropy in the interfacial free energy. As will be discussed in section 4, the large anisotropy of μ has important consequences in continuum modeling of dendrite growth.

A disadvantage of the free solidification technique is the fact that the computed velocities are subject to fairly large error and the scatter is much greater at low undercoolings (see below). At temperatures close to melting, the velocities are sufficiently slow such that even during long MD runs the interface moves only a handful of lattice spacings and thus large uncertainties are observed for $\Delta T < 10 - 20$ K. Unfortunately it is in this low undercooling regime where many detailed experimental studies of dendrite growth have been performed. What is desired then is an MD technique capable of extracting the kinetic coefficient exactly at T_M. As described below, techniques based on fluctuations provide such a capability.

3.2.3 Fluctuations

In 1997, Briels and Tepper [114] developed an MD technique for extracting the kinetic coefficient by monitoring the fluctations in the total number of solid atoms for a solid-liquid system maintained at the melting point. The authors studied the Lennard-Jones system and, an important ingredient of the method, utilized an NVT ensemble. Any fluctuation which moves the position of the solid-liquid interface, or equivalently changes the number of solid atoms, will lead to a change in pressure of the solid-liquid system owing to the fixed-volume constraint and the density difference between the phases.

If we assume that the pressure equilibrates rapidly on the time-scale of the atomic interface-attachment kinetics, the fluctuation will lead to a change in pressure of the system away from the equilibrium value at temperature *T*. A chemical potential difference between the solid and liquid phases results, providing a restoring force which tends to return the solid-liquid interface to its equilibrium position. If ΔN_S represents the change in the number of solid atoms from the average value, the following deterministic equation can be derived:

$$\frac{d\Delta N_S}{dt} = -\frac{1}{\tau}\Delta N_S \qquad 3.8$$

where the time constant τ is related to the thermodynamic restoring force and is given explicitly as:

$$\frac{1}{\tau} = k\frac{A}{aN}\left[\frac{\left(v_L^{eq} - v_S^{eq}\right)^2}{v_S^{eq}\kappa_S f_S^{eq} + v_L^{eq}\kappa_L f_L^{eq}}\right]\frac{1}{k_B T} \qquad 3.9$$

In the above expression the equilibrium volume per atom in the solid (*S*) and liquid (*L*) phase is denoted by v^{eq}, κ is the isothermal compressibility and f^{eq} is the equilibrium number fraction of solid and liquid with *N* being the total number of atoms in the simulation. The ratio *A/a* is the total interface area normalized by the specific area of a single atom in the solid. Briels and Tepper assume a-priori that the interface velocity is proportional to the chemical potential difference between the liquid and solid, $\mu_L - \mu_S$. The constant *k* appearing in eq. 3.9 reflects this proportionality. Specifically, one has:

$$V = kd\frac{\mu_L - \mu_S}{k_B T} \qquad 3.10$$

where *d* is the interplanar spacing of the crystal.

From eq. 3.8 it is straightforward to show that the correlation function given by $\langle \Delta N_S(t)\Delta N_S(0)\rangle$ decays exponentially according to:

$$\frac{\langle \Delta N_S(t)\Delta N_S(0)\rangle}{\langle \Delta N_S(0)^2\rangle} = \exp\left(-\frac{t}{\tau}\right) \qquad 3.11$$

The angular brackets in the above expression denote averages over many arbitrary time origins.

Briels and Tepper developed an order parameter which distinguishes quite effectively the solid and liquid atoms in the simulation and they computed the above correlation function vs. time. From the resulting value of τ the constant *k* can be derived from eq. 3.9 and the velocity vs. undercooling behavior is established. The solidification kinetics derived from the fluctuation technique was found to be in excellent agreement with both a non-equilibrium (ie. free solidification) simulation and the previous work by BGJ.

A distinct advantage of the Briels and Tepper scheme is the fact that the kinetic coefficient is computed precisely at the melting temperature. Since equilibrium fluctuations are monitored, one does not have to rely on an often inaccurate extrapolation of the velocity vs. undercooling data to zero undercooling in order to determine μ.

A disadvantage of the method is that it is formulated specifically for an NVT ensemble.

Rather than monitoring the average position of the solid-liquid interface during an MD simulation as was done by Briels and Tepper, it is possible to extract the value of μ from the kinetics of the entire *k*-space fluctuation spectrum of the interface position.
Consider again the quasi-2D solid-liquid system described in sect. 3.1. If ξ is the height of the interface as a function of *x*, then, for small amplitude fluctuations at the melting point, the time dependence of ξ can be written as:

$$\frac{1}{\mu}\frac{\partial \xi}{\partial t} = \Gamma \nabla^2 \xi + \eta(x,t) \tag{3.12}$$

The first term on the right hand side of the above expression represents curvature driven motion and $\Gamma = (\gamma + \gamma'')T_M / L$. To derive an appropriate expression for the noise term η, one first makes the usual assumption that the noise is uncorrelated in space and time. Second, the value of η is chosen such that the equilibrium fluctuation spectrum predicted by eq. 3.12 must be the same as the result obtained from capillarity theory, ie. eq 3.4. The above two requirements imply that the noise term possesses the following form:

$$\langle \eta(x,t)\eta(x',t') \rangle = 2\frac{k_B T}{bW\gamma}\frac{1}{k^2} \tag{3.13}$$

The solution of eq. 3.12 using eq. 3.13, is given by:

$$\left\langle \left| A(k,t) - A(k,0) \right|^2 \right\rangle = 2\left\langle \left| A(k) \right|^2 \right\rangle \left[1 - \exp(-t/\tau) \right] \tag{3.14}$$

where $A(k,0)$ refers to the amplitude evaluated at some arbitrary time origin and the decay constant is given by $\tau = \left(\Gamma \mu k^2\right)^{-1}$. A fit of the full time dependent correlation function to the exponential form of eq. 3.14 for various values of *k*, leads to a decay constant which varies as k^2 with slope proportional to μ.

Results for the kinetic fluctuation spectrum technique for extracting the value of μ are shown in fig. 3.8 for the case of pure EAM Ni. Simulation details are described fully in ref. [108]. The large scatter in the data suggests that long simulation runs are required to accurately determine μ, a clear disadvantage of the fluctuation spectrum method. Nevertheless, the correct k^2 dependence is reproduced in the results and the anisotropy between 100 and 110 interfaces can be seen. The best fit slopes, shown by the solid lines in fig. 2, lead to kinetic coefficient values of 52 $cm/s/K$ for the 100 direction and 40 $cm/s/K$ for 110. In reasonable agreement with the free solidification results. The anisotropy is found to be ≈ 1.3 which, again, is close to $\sqrt{2}$.

3.2.4 The Broughton, Gilmer and Jackson Growth Model

The earliest model of crystallization kinetics is due to Wilson [128] and Frenkel [129]. The rate expression is given by:

$$v = \left(D_L d / \Lambda^2\right) f e^{-\Delta S / k_B}\left[1 - e^{-\Delta\mu / k_B T}\right] \qquad 3.15$$

where d is the interplanar spacing of the growing crystal, Λ is the mean free path of an atom in the liquid and f represents the fraction of liquid atom collisions with the solid which result in a crystallization event. The thermodynamic driving force in the above model is contained in the term $e^{-\Delta S / k_B}\left[1 - e^{-\Delta\mu / k_B T}\right]$ where ΔS and $\Delta\mu$ are the differences in entropy and chemical potential between the solid and liquid phases. For a derivation of the thermodynamic driving force term using rate theory arguments the reader is referred to the review article by Jackson [134].

The Wilson-Frenkel model predicts that growth involves two thermally activated processes, one reflecting the free energy difference between the solid and liquid and the second arising from the diffusivity. At low temperatures the diffusivity term should dominate, however the Lennard-Jones results of BGJ clearly showed that the crystallization rate remains high even in temperature regimes where $D_L \approx 0$.

BGJ modified the growth model by replacing the diffusion term by a thermal velocity contribution. The final form of the BGJ model is given by:

$$v = (d / \lambda) f \left(3 k_B T / m\right)^{1/2} e^{-\Delta S / k_B}\left[1 - e^{-\Delta\mu / k_B T}\right] \qquad 3.16$$

Here $3k_B T / m$ with the m being the atomic mass is the thermal velocity in the liquid and λ represents an average distance traversed by an atom. The authors argue that $\lambda \approx .4a$ where a is the lattice constant.

The replacement of the diffusion coefficient by the thermal velocity implies that crystallization in the Lennard-Jones system does not require a local rearrangement of the liquid structure near the boundary in order to achieve a successful atomic hop from liquid to solid. As summarized by Jackson [135], there exists two classes of materials. One, which includes glasses, semiconductors and other directionally bonded materials, is well characterized by the Wilson-Frenkel model. The second class can be modeled using the BGJ formalism and includes metals and model systems which are well described by spherically symmetric interatomic interactions. EAM metals clearly fall into the latter category.

In what follows we would like to compare the BGJ model with available MD data for various EAM systems. To do so we will first approximate the temperature dependence of the solid-liquid free energy difference as $\Delta H_{fus} - T\Delta S_{fus}$ where ΔH_{fus} is simply the potential energy difference found from separate MD runs and $\Delta S_{fus} = \Delta H_{fus} / T_M$. The only remaining unknown is the probability *f*. For this quantity we shall simply use the best fit value obtained by BGJ in their Lennard-Jones study. Notice, there is no reason to suspect that *f* is the same for all growth directions. Nevertheless, for lack of a detailed theoretical prediction of the attachment probability, we will invoke an isotropic *f* at the outset.

Figure 3.9 shows a comparison of the solid-liquid interface velocity obtained from MD simulations vs. the velocity predicited by the BGJ model. The MD simulations represent free solidification results for the 100 and 110 growth directions in a variety of EAM metals. Although there is fairly large uncertainty in the simulation data at low velocities (low undercoolings), the agreement between model and simulation is quite good up to quite large velocities. At very high undercoolings the model overestimates the interface velocity and the possible origin of this discrepancy is discussed in ref. [117]. In addition to the results for EAM systems, Tymczak and Ray [133] also report good agreement between MD simulation and BGJ theory for BCC Na modeled using an interatomic pair potential based on pseudopotential perturbation theory. The results of fig. 3.9 indicate that the BGJ model is a good prediction of the kinetic coefficient in elemental metals provided, as discussed below, the low index 100 and 110 orientations are considered.

The presence of the interplanar spacing in eq. 3.16 implies that the ratio of velocities between the 100 and 110 growth direction is indeed $\sqrt{2}$. As discussed above the $\sqrt{2}$ relationship has been confirmed in all three MD simulation techniques. Therefore it is now safe to conclude that the high anisotropy in the kinetic coefficient, first observed by Hoyt et al. [132], is in fact correct.

Although the BGJ model of crystallization kinetics is obeyed quite well for the 100 and 110 orientations, the agreement between model and simulation is poor for the 111. Typically, the MD results show a much lower velocity than predicted by eq. 3.16, the BGJ model predicts that the 111 velocity should be, in fact, higher than that of 100. Part, but not all, of the explanation for the sluggish 111 kinetics is due to the presence of stacking faults. In 1988 Burke, Broughton and Gilmer (BBG) [126] investigated the kinetics of crystallization in the Lennard-Jones system for the 100 and 111 interfaces and offered one explanation as to the slower than expected growth in the 111 direction. The authors argue that an atom from the liquid phase can attach itself to either an FCC site or an HCP site on the adjacent 111 solid surface. If the stacking fault energy is sufficiently low and/or the driving force sufficiently high, islands of defective HCP atoms may form during the course of solidification. Since, eventually, the resulting solid is defect free, the system must "anneal" out these HCP islands in order for crystallization to proceed. Thus the thermally activated growth step is not the thermal motion of atoms in the liquid as assumed in the BGJ model, but rather the conversion of all layer atoms to the FCC orientation. As discussed below, we conclude that the explanation of Burke et al. is also valid in the case of Au and Ag, and by extension Cu and Ni.

The first evidence for the existence of growth limited by the annealing of faults is a size dependent crystallization rate. BBG found that the 111 growth velocity is faster for a system in which the area of the solid-liquid interface is decreased. The authors argue that in a small system the defect clusters cannot grow as large before contacting clusters from the periodic image of the cell. Since it is the cluster circumference to area ratio which determines the rate of annealing, the smaller systems exhibit a higher growth rate. Figure 3.10 shows the size effect for the case of Au. Here the velocity vs. undercooling was obtained for a small system whose solid-liquid boundary area measured 1728 Å^2 (seven (1-10) atomic planes by four (11-2) planes) and a large system with an interface area of 5876. Å^2 (12 (1-10) x 8 (11-2)). Consistent with findings of BBG the smaller system size possesses a significantly higher growth rate in the 111 direction. No such size effect is found for the 100 or 110 growth directions.

A second indication that the BBG mechanism is operative for the case of Au and Ag, is provided by a detailed examination of the structure of the solid-liquid boundary. In what follows it will be convenient to distinguish atoms of the solid phase from atoms belonging to the liquid and for this purpose the order parameter of eq. 3.6 is used. Recall if $\phi_j > .7$ the atom is considered to be part of the liquid phase and vice-versa for the solid. However, in the case of the 111 orientation, high values can also indicate an atom in a HCP defect site on the solid surface, as discussed below. Figure 3.11 shows a cut parallel to the solid-liquid interface at a depth well within the solid phase. The figure was generated from the large solid-liquid system of pure Au. In fig. 3.11, and subsequent figs. 3.12 and 3.13, the white atoms denote solid atoms whereas the gray atoms are liquid or defect atoms. The crystalline plane clearly shows the six fold symmetry of the 111 plane and at this position far from the boundary plane there a very few gray "defect" atoms. Figure 3.12 depicts a similar plane at a position in the liquid far from the solid-liquid interface. The thickness of the cut was kept the same as in the previous figure. In this position the atomic arrangement is highly disordered, there is little evidence of six fold symmetry and most atoms are colored gray. The proceeding figures should be compared with fig. 3.13 which shows the atomic arrangement for the layer adjacent to the liquid phase. Here roughly half of the atoms are white and exhibit six fold symmetry. These atoms occupy the proper lattice positions of the solidifying solid. However, there are also many other atoms which also exhibit six fold symmetry, but, being colored gray, do not lie on perfect FCC sites. These atoms represent defect clusters on the surface and three such regions are shown by heavy black lines in fig. 3.13. For the regions in the upper center part of the figure and for the area to the left of the drawing, one can show that the atomic arrangement is HCP by extending the FCC atom planes in nearby regions as shown by the light black lines. The displacement of the gray atoms from the ideal planes (white atoms) is one half of the 11-10 *d* spacing as expected from a stacking fault. The continued crystallization of the system requires that the faulted regions as shown in fig. 3.13 must shrink at the expense of the perfect FCC regions and as a result the 111 kinetics are slower relative to the 100 and 110 orientations.

The region delineated in the upper right portion of fig. 3.13 shows a six fold symmetric arrangement of gray atoms, yet the region is rotated by 30 degrees with respect to the underlying 111 surface. Such a rotation implies that there are alternate atoms in FCC and HCP positions in the defect cluster and the nearly equal atom spacing means there exist some displacement of atoms from the hollow sites. Although the region is an interesting observation, it is doubtful that such defect clusters play a major role in the growth kinetics, as they appear to occur infrequently.

Unfortunately the presence of stacking fault islands does not fully explain the discrepancy between the simulated velocity vs. undercooling behavior and the growth model of BGJ. The fast growth rate of the small system size, which minimizes the effect of stacking fault formation, shown in fig. 3.10 is still much less than that predicted by BGJ. Recall from eq. 3.16 that the crystallization rate is proportional to the lattice *d* spacing meaning that the 111 orientation ($d = \sqrt{3}/3$) should solidify more rapidly than the 100 orientation ($d = a/2$). The relationshoip $\mu_{111} > \mu_{100}$ has never been observed in atomistic simulation even for small system sizes. Huitema et al. [136] offer an explanation for the slow growth of the 111 direction. These authors argue that the kinetic coeffcient consists of two mechanisms which add in series, ie. $1/\mu = 1/\mu_{org} + 1/\mu_{hop}$. Here "org" refers to the mechanism of intralayer organization of the liquid atoms into the crystalline lattice and μ_{hop} denotes the hopping within the layer to increase the density. From a detailed examination of their simulations of crystallization in the Lennard-Jones system the authors were able to show that the dominant mechanism in the 100 direction is the μ_{org} term whereas the hopping contribution is large for the 111 direction. The BGJ model assumes a mechanism of atom attachment from the liquid to the solid and thus neglects any mechanism of the type μ_{hop}. Although the Huitema et al. arguments provide a plausible explanation for the observed behavior, the theory is at this point qualitative and a fully quantitative description of the crystallization of the 111 orientation remains an open question.

3.3 The Diffusion Coefficient

In phase field or sharp interface models of solidification the diffusivity in the liquid is invariably assumed to be $1\mathrm{x}10^{-5}\ cm^2/s$. This value however is merely an order of magnitude estimate and from what little experimental data exists it is clear that the assumed DL can be in error by a factor of two or more. Since the diffusion coefficient sets the velocity of interface motion through the solute conservation boundary condition its true value is important in modeling the correct morphology and growth rate of a dendrite. MD simulations provide a straightforward means of obtaining the diffusivity in the liquid and in this section we review some results obtained from EAM elemental metals. Continued advances in computer power have made it possible to compute DL using first principles MD techniques and thus results from ab-initio MD will be summarized as well.

There are two methods for computing liquid diffusivities from MD simulations [137]. The first relates the diffusion coefficient to the long time behavior of the mean square displacement of an atom and is given by:

$$D_L = \lim_{t\to\infty}\frac{1}{6t}\left\langle\left|\mathbf{r}(t)-\mathbf{r}(0)\right|^2\right\rangle \qquad 3.17$$

The position of an atom at any time t is denoted by $\mathbf{r}(t)$ and the angular brackets indicate an average with respect to all atoms in the simulation and over all time origins. The second technique for computing D_L is through the formulation of the velocity-velocity correlation function, $Z(t)$, which is defined as:

$$Z(t) = \frac{1}{3}\langle \mathbf{u}(t) \cdot \mathbf{u}(0) \rangle \tag{3.18}$$

where **u** is the velocity vector. The diffusivity is related to the function $Z(t)$ by a straightforward integration over all time, that is:

$$D_L = \int_0^\infty Z(t)dt \tag{3.19}$$

Figure 3.14 shows the mean square displacement, that is the bracketed term in eq. 3.17, vs. the time for liquid Ni modeled using the FBD potential at two temperatures;1600 and 2000K. The results are reproduced from the work of Hoyt et al. [132]. After a short transient period of approximately .2*ps* a linear relationship is established with a slope equal to $6D_L$. The increased diffusivity with increasing temperature is clearly observed. Figure 3.15 shows the velocity-velocity correlation function normalized by its value at t=0 vs. the time for Ni. The two temperatures shown are again 1600 and 2000K. It can be seen that all velocity correlations decay rapidly and are essentially zero after about .5*ps*. The negative correlation observed in the vicinity of the minimum at about 75*fs* is a well known effect in dense fluids and arises due to backscattering resulting from the cage of atoms which surrounds any given atom. As is also typical in fluid systems this so-called cage effect becomes less pronounced as the temperature is increased. The diffusion coefficient as determined by eq. 1 at 2000K was found to be 5.54x10^{-5} cm^2/s whereas the diffusivity computed via the $Z(t)$ correlation function was 5.67x10^{-5} cm^2/s. The error of about 2.5% demonstrates the equivalence of the two methods.

Figure 3.16 plots the diffusion coefficient of Ni (filled squres) and Cu (filled circles) as a function of temperature. At moderate undercoolings and at the short time scales required for a diffusivity computation, there is no evidence in the MD simulations to indicate crystallization (for example, a drift in the average temperature in the system). Therefore, the diffusion data includes three points in the undercooled regime and the range of the data is from 140K below the melting temperature to 310K above T_m. The vertical lines on each curve indicate the EAM melting temperatures. Data for both Ni and Cu suggest a nearly linear dependence with temperature consistent with experimental data for several pure metals and in agreement with phenomenological theories of liquid phase diffusion [138]. A linear regression analysis yields the following temperature behavior: $D_{\mathrm{Ni}} = 6.92x10^{-4}(T - T_M) + .382$ and $D_{\mathrm{Cu}} = 7.219\mathrm{x}10^{-4}(T - T_M) + .332$ in units of $10^{-4}\ cm^2/s$ ($Å^2/ps$).

The symbols filled with X's in fig.3.16 label the diffusion coefficients computed by Allemany et. al. [139,140] using the Voter-Chen (VC) EAM potential rather than the Foiles-Baskes-Daw potential. It should be pointed out however that a significant difference between the computations of Hoyt et al. and those of Alemany et al. is the fact that the latter study used the experimental value of the liquid density when performing the MD simulations. The filled symbols of fig. 3.16 were obtained by equilibrating the liquids at each temperature (zero pressure) to obtain the EAM predicted density. The results for Ni are within fairly good agreement, the VC results being approximately 10-15% lower and the trend with temperature appears to be consistent. For Cu the agreement is somewhat worse, on the order of 20%, and the VC potential again yields a lower value. The open circles shown in fig. 3.16 are results from the capillary reservoir technique of Henderson and Yang [141]. Agreement between the present simulations and experiment is fairly good, particularly at the lower temperatures, with the EAM predicting consistently lower values. Because of the scatter in the experimental data it is difficult to confidently glean the behavior with temperature, but it appears that the simulations predict a somewhat smaller slope than the measurements. It is interesting to note that the FBD potential is in better agreement with experiment than the Voter-Chen results shown in fig. 3.16. The improved agreement is surprising given that the Alemany et al. investigation fixed the number density of the liquid equal to the experimental value. The closer agreement between EAM and experiment is also surprising when one compares the results of an ab-initio MD study [142] which is denoted by the symbol $\oplus$ in fig. 3.16. The ab-initio result, which is of course free of any inaccuracies associated with the assumption of an empirical potential, is in fact furthest removed from the experimental results.

In 1996, Dzugutov [143] proposed a universal scaling relationship between the diffusion coefficient and the excess entropy of a liquid. A similar scaling law was developed earlier by Rosenfeld [144]. The Dzugutov scheme starts with the definition of a scaled diffusivity defined by $D^* = D_L \nu^{-1} \sigma^{-1}$ where σ is the hard sphere diameter and ν is the collision frequency according to the well known Enskog theory of atomic transport [145]:

$$\nu = 4\sigma^2 g(\sigma)\rho\sqrt{\frac{\pi k_B T}{m}} \qquad 3.20$$

Here $g(\sigma)$ is the radial distribution function evaluated at the hard sphere diameter [in practice σ may be interpreted as the position of the first peak in $g(r)$], ρ is the number density of the liquid and the square root term is, apart from a numerical constant, the thermal velocity appearing in the BGJ model. Dzugutov proposed that D^* is proportional to e^S where S is the excess entropy and demonstrated its validity for the hard-sphere, Lennard-Jones and a variety of other pair potential systems. It is not clear however, if the scaling still holds for interatomic potentials of the many body type or for potentials which include a strong contribution from directional bonding. Hoyt et al. [146] performed MD simulations to test the Dzugutov law for these latter two cases and the results are shown in fig. 3.17. For the EAM elements Au, Ag, Cu, Ni, Pd and Pt as wells as the binary systems Ni3Al and AuPt the data collapse shown in the figure implies the scaling behavior is valid for the EAM multi-body form. Si was modeled using the Stillinger-Weber [147] potential which includes angular dependent contributions to the bonding. It is clear from fig. 3.17 that the scaling law fails in the case of Si and Hoyt et al. argue that the source of the discrepancy arises from the inability of the Enskog frequency to capture the true kinetics in Si.

The lone ab-initio data point for Cu in fig. 3.16 is due to Pasquarello et al. [142] and represents the first time first principles techniques have been used to study dynamic properties of liquid metals. The authors used the well known Car-Parinello [148] molecular dynamics scheme. In more recent times, ab-initio MD studies of metals have utilized the more efficient Vienna ab initio simulation package or VASP [149-152]. The

VASP code makes use of ultrasoft pseudopotentials and an expansion of the electronic wave functions in plane waves. Typically the local density approximation is employed in simulations although gradient corrections are possible. Kresse and Hafner [153] computed the diffusivity of liquid Cu and V and Kirchhof et al [154] obtained the diffusion coefficient in liquid Se using the VASP approach. In addition, liquid Fe and Fe-S alloys at ambient pressures and at pressures consistent with those of the earth's core were studied by Alfe et al.[155-157] and de Wijs et al [158]. Diffusion of both K and Sb in liquid K3Sb and KSb alloys were reported by Seifert-Lorenz and Hafner[159].

Asta et al. [160] used ab-initio MD to study diffusion of Ni and Al in a liquid of composition $Ni_{20}Al_{80}$ and compared the results with three versions of EAM potentials. The mean square displacement of an atom vs the time is shown in fig. 3.18 where the data was taken after an equilibration time of 1.3 ps. The temperature of the liquid was 1700K. Although the maximum time in fig. 3.18 , 5.6 ps, is considerably less than in simulations involving empirical potentials, a linear relationship is nevertheless observed. Diffusion coefficients for Ni, .24x10-4 cm^2/s, and Al, .42x10-4 cm^2/s, are considerably less than the values from EAM simulations. The discrepancy may be due to a subtle electronic charge transfer effect which is not captured in the EAM formalism.

3.4Binary Alloys

Atomistic simulations of solid-liquid interface properties is considerably more difficult than the case of elemental systems. In an equilibrium solid-liquid system for a binary alloy the concentrations of the two phases are different and, in addition to the concentration difference between the bulk solid and liquid, there is also the possibility of equilibrium segregation of the solute species to the interface. The time scales to establish equilibrium concentration profiles via diffusion in the liquid or solid are much too long for MD simulations and one is forced to utilize Monte-Carlo techniques. MC simulations in the semi-grand-canonical ensemble (or the transmutation ensemble see eg [161]) are ideally suited to the problem of equilibration in solid-liquid systems as the ensemble allows for not only atomic displacements, but changes in chemical identity as well. However, changes of a solute atom to a solvent atom, or vice-versa, are performed under an imposed chemical potential difference between the two species. Therefore, the creation of an equilibrium solid-liquid system at a given temperature requires a prior knowledge of the solution thermodynamics of the alloy and the solidus and liquidus curves in the phase diagram. In this section we will review thermodynamic integration techniques to compute thermodynamic properties of alloys and we will summarize MC results of interface structure and segregation.

To date only a few studies have been devoted to the properties of solid-liquid interfaces in alloy systems. Huitema et al. [162] examined crystallization kinetics in Lennard-Jones mixtures using MC and identified the transition from smooth to rough growth as a function of solute-solvent interaction strength and temperature. Nonequilibrium partitioning and solute trapping effects during solidification have been studied using MD in Si-Ge alloys be Yu et al [163] and in the Lennard-Jones system in the aforementioned work of Celestini and Debierre. Interface structure and diffusion profiles in binary hard-sphere systems [164,165] and model ionic alloys [166] have also been investigated with MD. In particular, Davidchack and Laird [165] analyzed the density profiles across the 100 and 111 solid-liquid interfaces in mixture of hard spheres with a diameter ratio equal to .9. The authors found that equilibrium segregation effects were minimal, but cautioned that this conclusion may be affected by the difficulty in obtaining chemical equilibrium on the time scales of MD.

Ramalingam et al. [167] outlined an MC method for computing the solid-liquid phase boundary in binary alloys as a first step in studying interfacial properties. The system chosen for study was EAM Cu-Ni, dilute in Cu, where the interatomic potential was generated by Foiles [168]. First, the chemical potential difference of pure Ni in the solid and liquid phase can be found via the thermodynamic relation:

$$\left(\frac{\partial(\mu/T)}{\partial T}\right)_P = -\frac{1}{T^2}H \qquad 3.21$$

Where H is the enthalpy per atom. Equation 3.21 can be integrated from the known melting point, where $\mu_{Ni}^S = \mu_{Ni}^L$, such that the chemical potential difference vs. temperature function can be determined. With the chemical potential of pure Ni established, the Gibbs free energy as a function of Cu concentration (X_{Cu}) can be found using a second thermodynamic relation:

$$\left(\frac{\partial G}{\partial X_{Cu}}\right)_{P,T} = \Delta\mu(X_{Cu},P,T) \tag{3.22}$$

Where $\Delta\mu = \mu_{Ni} - \mu_{Cu}$ is the chemical potential difference between Ni and Cu in the solid or liquid phase. To determine the RHS of eq. 3.22, MC simulations in the semi-grand-canonical ensemble are performed on the bulk solid and liquid systems. In the simulations an imposed value of $\Delta\mu$ generates the equilibrium concentration of Cu. Specifically, $\Delta\mu$ vs. X_{Cu} data is fit to the following functional form:

$$\Delta\mu(X_{Cu},T,P) = k_B T \ln\left(\frac{X_{Cu}}{1-X_{Cu}}\right) + \sum_{i=0}^{n} A_i X_{Cu}^i \tag{3.23}$$

where the first term on the RHS side represents the ideal contribution and the final term describes departures from ideality. Once the coefficients A_i are found, eq. 3.23 can be integrated to yield the free energy

$$\begin{aligned} G(T,X_{Cu}) = G(T,X_{Cu}=0) + k_B T[X_{Cu}\ln X_{Cu} + (1-X_{Cu})\ln(1-X_{Cu})] \\ + \sum_{i=0}^{n} A_i X_{Cu}^{i+1}/(i+1) \end{aligned} \tag{3.24}$$

The first term on the RHS is the chemical potential of pure Ni and for computing phase boundaries one can set $\mu_{Ni}^s = 0$ and determine the liquid chemical potential using the integration of eq. 3.21. Using the thermodynamic integration procedure, Ramlingam, et al. find good agreement between the EAM Cu-Ni phase boundaries and those of experiment. For example, the MC simulations yield a segregation coefficient (at T=1750K) of $k = X_{Cu}^s / X_{Cu}^l = .5$ whereas the experimental value is .6 at 1642K. Actual composition in the liquid phase is $X_{Cu} = 10.1\%$ and $X_{Cu} = 5.0\%$ for the solid.

With the solution thermodynamics of Cu-Ni established the authors generated density and concentration profiles in solid-liquid simulation cells for two different interface orientations, 100 and 111. Density profiles were very similar for both orientations and an effective interface width of $7.2 \pm .9\,\text{Å}$ was found. From the equilibrium concentration profiles an important interface quantity, the relative absorption, could be determined. Denoted by $\Gamma_{Cu}^{(Ni)}$, the relative adsorption coefficient is defined as the excess number of Cu atoms at the interface if the Gibbs dividing surface is chosen such that the excess number of Ni atoms is zero. $\Gamma_{Cu}^{(Ni)}$ is independent of the position of the dividing surface, a necessary property of excess interface quantities, and gives a measure of the concentration dependence of the solid-liquid interfacial free energy. Ramalingam et al. found the following adsorption coefficients, in units of $atoms/nm^2$, for the two interfaces $\Gamma_{Cu}^{(Ni)} = .04 \pm .71$ for 100 and $-.64 \pm .60$ for 111. Since a monolayer of Cu corresponds to 15.0 and 17.3 *atoms/nm*^{2}, it was concluded that in the Cu-Ni system negligible adsorption at the solid-liquid interface takes place.

The MC procedure can also be employed to generate equilibrium quasi-2D solid-liquid which can then be used in an MD computation of the solid-liquid interfacial free energy (sec. 3.1). Results of the fluctuation spectrum for Cu-Ni in three different orientations are shown in fig. 3.19. The simulations were performed at 1750K and the liquid and solid compositions are approximately those quoted above. A γ_o value of $268\,mJ/m^2$ and an anisotropy of 1.2% were determined. The results represent the first computation of the anisotropic solid-liquid interfacial free energy in a binary alloy.

4. Experimental Validation

Since atomistic simulations can provide the difficult to measure ε_4 anisotropy and the nearly impossible to measure quantities μ and ε_4^k, it is possible to perform continuum level computations of solidification with no adjustable parameters. Such a study was recently conducted by Bragard et al. [45] who derived dendrite growth velocities in pure

Ni as a function of undercooling. Ni provides an ideal test of phase field modeling. Not only has Ni been well studied in MD studies, but experimental data of the dendrite velocity vs. undercooling behavior for Ni is available from two separate experiments [169,170] (see also [171]). Both experiments utilized magnetic levitation of Ni droplets in order to avoid heterogeneous nucleation at container walls, thus allowing large undercoolings to be studied. Also, both experiments used a needle trigger to initiated the solidification reaction. The velocity of the resulting solidification front was measured by the abrupt change in surface temperature as the front passes. Willnecker et al. [169] monitored the temperature drop using two photodiodes in two regions of the droplet and determined the velocity by the time difference between the front arrival time on each sensor. Lum et al. [170] used a fast high resolution video camera that captures the thermal profile of the entire surface and thus provides information about both velocity and morphological evolution of the solidification front.

In the initial phase field simulations, Bragard et al. found that the dendrite tip velocity became independent of the interface thickness for values of the parameter λ close to unity. The result $\lambda \approx 1$ is equivalent to choosing an interface width on the order of the nanometer scale of the capillary length and thus the simulations become quite inefficient. Upon further investigation, the authors found that the temperature variation across the solid-liquid diffuse boundary was small compared to the interface undercooling, meaning the correction term to the kinetic coefficient resulting from the thin interface limit, ie. the last term of eq. 2.25, was negligibly small for the case of pure Ni. The severe constraint on the interface width also resulted in a velocity vs. undercooling behavior which was nonlinear as λ increased. MD simulations indicate that for the largest dendrite velocities accessed in experiments, 60-80m/s, the interface should remain a linear function of undercooling. To circumvent the above problems the authors modified the form of the last term of the free energy functional in eq. 2.11 from $f(\phi)+g(\phi)\lambda u$ to:

$$f(\phi)+G(\lambda u)g(\phi) \qquad 4.1$$

The new function G cannot be written down analytically, but was derived through a series of phase field computations of a planar solid-liquid boundary, moving in one direction, at various undercoolings. G, then, is that function which maintains the proper linear relationship between velocity and undercooling with a constant of proportionality, that is the kinetic coefficient, appropriate for pure Ni. Defining the new function G and mapping its dependence on λu effectively lifts the constraint on interface width and efficient implementation of the phase field model is again possible.

Bragard et al. studied dendrite velocity for undercooling as high as 350K. The random walker technique was utilized to capture the far field thermal field and the simulations were performed in three dimensions. The tip velocity vs. undercooling phase field results are shown by the solid line and the black triangles in fig. 4.1. The open symbols represent the two experimental results. Overall the agreement between simulation and experiment is excellent and it must be reiterated at this point that the continuum model contains no adjustable parameters. In addition to the comparison with experiment, the authors also examined the sensitivity of the results to the values of the two anisotropies in the problem. They found that the results were largely independent of the anisotropy in γ whereas both the solidification rate and the growth morphologies depend sensitively on the anisotropy of the kinetic coefficient. The Ni simulations point to the need of including both ε_4 and ε_4^k in any realistic simulation of dendrite growth.

For undercoolings above about 200K the phase field prediction lies consistently above the experimental data. The experiments tend to show a leveling of the curve above $\Delta T = 200\,\mathrm{K}$. This somewhat abrupt change in slope was first observed by Walker in the 1960's [172] and the experiments of Lum et al. suggest that the break is correlated with a change of morphology. For undercoolings below 200K the solidification front remains smooth whereas above this critical undercooling the front appears angular. (The video imaging cannot resolve individual dendrite tips, but only the macroscopic front.) The origin of the change in slope of the V vs. ΔT function remains an open question, but clearly the explanation must stem from some effect which has been left out of the phase field model. Candidates include convection in the liquid or the presence of trace impurities, most likely oxygen, in the Ni droplets.

5. Summary and Future Directions

The phase field model has been proven to be much more powerful than simply a numerical tool for solving the moving boundary problem in alloy solidification. Once limited to the range of large undercooling and supersaturation, the phase field model has been reformulated and combined with other efficient numerical schemes such that dendrite solidification can be successfully modeled at any temperature and composition. In addition, important yet difficult to measure, materials anisotropies need no longer be treated as adjustable parameters in simulation studies. Molecular dynamics and Monte-Carlo atomistic simulations are now providing the necessary anisotropies in a wide range of technologically relevant metals.

The excellent agreement between modeling and experiment for the case of dendrite velocity vs. undercooling in pure Ni illustrates just how far the field of solidification modeling has progressed within the past decade. Yet the results also clearly define the future directions of the phase field modeling research. The inability of the model to reproduce the observed change of slope of V vs. ΔT strongly suggest that impurities are playing a significant role. Therefore phase field modeling and atomistic simulation must, in the future, concentrate on the question of alloying. An efficient version of an alloy phase field model has only recently been developed and atomistic simulations of solid-liquid interface properties in binary alloys are still quite rare. Efficient modeling of alloy solidification is also essential from the technological point of view as all commercial cast or welded materials are binary or multicomponent alloys.

6. References

[1] G. P. Ivantsov, *Dokl. Akad. Nauk SSSR*, **58**, 567 (1947).

[2] G. Horvay and J. W. Cahn, *Acta Metall.*, **9**, 695 (1961).

[3] B. Chalmers, *Principles of Solidification*, (Wiley and Sons., New York) 1964.

[4] J. S.Langer, *Rev. Mod. Phys.*, **52**, 1 (1980).

[5] D. E. Temkin, *Dokl. Akad. Nauk SSSR*, **132**, 1307 (1960).

[6] M. E. Glicksman, R. J. Shaefer and J. D. Ayers, *Metall. Trans. A*, **7**, 1747 (1976).

[7] J. S. Langer and H. Muller-Krumbhaar, *Acta Metall.*, **26**, 1681 (1978).

[8] J. S. Langer and H. Muller-Krumbhaar, *Acta Metall.*, **26**, 1689 (1978).

[9] J. S. Langer and H. Muller-Krumbhaar, *Acta Metall.*, **26**, 1697 (1978).

[10] T. Fujioka, PhD Thesis, Carnegie-Mellon University (1978).

[11] C. S. Lindenmeyer and B. Chalmers, *J. Chem. Phys.*, **45**, 2807 (1966).

[12] J. Hallett, *J. Atmos. Sci.*, **21**, 671 (1964).

[13] H. R. Pruppacher, *J. Colloid Inter. Sci.*, **25**, 285 (1967).

[14] B. F. Ryan, *J. Crystal Growth*, **5**, 284 (1969).

[15] M. B. Koss, J. C. LaCombe, L. A. Tennenhouse, M. E. Glicksman and E. A. Winsa, *Metall. Trans. A*, **30**, 3177 (1999).

[16] G. E. Nash and M. E. Glicksman, *Acta Metall.*, **22**, 1283 (1974).

[17] R. C. Brower, D. A. Kessler, J. Koplik and H. Levine, *Phys. Rev. A*, **29**, 1335 (1984).

[18] R. C. Brower, D. A. Kessler, J. Koplik and H. Levine, *Phys. Rev. Lett.*, **51**, 1111 (1983)

[19] D. Kessler, J. Koplik and H. Levine, *Phys. Rev. A*, **30**, 3161 (1984).

[20] D. Kessler, J. Koplik and H. Levine, *Phys. Rev. A*, **31**, 1712(1985).

[21] E. Ben-Jacob, N. D. Goldenfeld, J. S. Langer and G. Schon, *Phys. Rev. Lett.*, **51**, 1930 (1983).

[22] E. Ben-Jacob, N. D. Goldenfeld, J. S. Langer and G. Schon, *Phys. Rev. A*, **29**, 330 (1984).

[23] D. Meiron, *Phys. Rev. A*, **33**, 2704 (1986).

[24] D. A. Kessler and H. Levine, *Phys. Rev. B*, **33**, 7867 (1986).

[25] D. A. Kessler and H. Levine, *Phys. Rev. Lett.*, **57**, 3069 (1986).

[26] M. E. Glicksman and N. B. Singh, *J. Cryst. Growth*, **98**, 277 (1989).

[27] M. E. Glicksman and N. B. Singh, *Rapidly Solidified Powder Aluminum Alloys*, edited by M. E. Fine and E. A. Starke (ASTM, Philadelphia, 1986), pg. 44.

[28] M. Muschol, D. Liu, and H. Z. Cummins, *Phys. Rev. A.*, **46**, 1038 (1992).

[29] A. Dougherty and J. P. Gollub, *Phys. Rev. A*, **38**, 3043 (1988)

[30] P. Oswald, *J. Phys. (Paris),* **49**, 1083 (1988).

[31] K. Koo, R. Ananth, and W. N. Gill, *Phys. Rev. A*, **44**, 3782 (1991).

[32] R. Napolitano amd R. Trivedi, to be published.

[33] S.- C. Huang and M. E. Glicksman, *Acta Metall.*, **29**, 701 (1981).

[34] M. E. Glicksman and N. B. Singh, *J. Cryst. Growth*, **98**, 277 (1989).

[35] E. R. Rubenstein and M. E. Glicksman, *J. Cryst. Growth*, **112**, 84 (1991).

[36] J. S. Langer, *Directions in Condensed Matter* (World Scientific, Singapore, 1986) p. 164.

[37] V. L. Ginzburg and L. D. Landau, *Sov. Phys. JETP*, **20**, 1064 (1950).

[38] J. W. Cahn and J. E. Hilliard, *J. Chem. Phys.*, **28**, 258 (1958).

[39] S. M. Allen and J. W. Cahn, *Acta Metall.*, **27**, 1085 (1979).

[40] B. I. Halperin, P. C. Hohenberg and S. K. Ma, *Phys. Rev. B*, **10**, 139 (1974).

[41] G. J. Fix, in *Free Boundary Problems: Theory and Applications*, edited by A. Fasano, and M. Primicerio (Piman, Boston, 1983) Vol II, p580.

[42] J. B. Collins and H. Levine, *Phys. Rev. B*, **31**, 6119 (1985).

[43] O. Penrose and P. C. Fife, *Physica D*, **43**, 44 (1990).

[44] S-L. Wang, R. F. Sekerka, A. A. Wheeler, B. T. Murray, S. R. Coriell, R. J. Braun and G. B. McFadden, *Physica D*, **69**, 189 (1993).

[45] J. Bragard, A. Karma, Y. H. Lee and M. Plapp, *Interface Science*, to be published.

[46] A. Karma and W. Rappel, *Phys. Rev. E*, **57**, 4323 (1998).

[47] R. Pieters and J. S. Langer, *Phys. Rev. Lett.*, **56**, 1948 (1986).

[48] M. Barber, A. Barbieri and J. S. Langer, *Phys. Rev. A*, **36**, 3340 (1987).

[49] D. Kessler and H. Levine, *Europhys. Lett.*, **4**, 215 (1987).

[50] J. S. Langer, *Phys. Rev. A*, **36**, 3350 (1987).

[51] E. Brener and D. Temkin, *Phys. Rev. A*, **51**, 351 (1995).

[52] A. A. Wheeler, B. T. Murray and R. Schaefer, *Physica D*, **66**, 243 (1993).

[53] J. A. Warren and W. J. Boettinger, *Acta Metall. Mater.*, **43**, 689 (1995).

[54] A. Karma and W. J. Rappel, *Phys. Rev. E*, **60**, 3614 (1999).

[55] P. H. Leo, J. S. Lowengrub and H. J. Hou, *Acta Mater.*, **46**, 2113 (1998).

[56] R. Podhuri and L. G. Chen, *Acta Mater.*, **45**, 1115 (1997).

[57] D. Fan, L. Q. Chen, S. P. Chen and P. W. Voorhees, *Comp. Mater. Sci.*, **9**, 329 (1998).

[58] D. Fan and L. Q. Chen, *Acta Mater.*, **45**, 611 (1997).

[59] D. Fan, C. Geng and L. Q. Chen, *Acta Mater.*, **45**, 1115 (1997).

[60] A. E. Lobkovsky and J. A. Warren, *J. Cryst. Growth*, **225**, 282 (2001)

[61] R. Kobayashi, J. A. Warren and W. C. Carter, *Physica D*,**140**, 141 (2000)

[62] Karma, *Phys. Rev. E*, **49**, 2245 (1994).

[63] A. A. Wheeler, G. B. McFadden and W. J. Boettinger, *Proc. Roy. Soc. London, Series A*, **452**, 495 (1996).

[64] Y. U. Wang, Y. M. Jin, A. M. Cutino and A. G. Khachaturyan, *Phil. Mag. Lett.*, **87**, 385 (2001).

[65] J. J. Eggleston, G. B. McFadden and P. W. Voorhees, *Physica D*, **150**, 91 (2001).

[66] A. Karma, D. A. Kessler and H. Levine, *Phys. Rev. Lett.*, **87**, 5501 (2001).

[67] Y. L. Li, S. Y. Hu, Z. K. Liu and L. Q. Chen, *Appl. Phys. Lett.*, **78**, 3878 (2001).

[68] G. Caginalp, *Phys. Rev. A*, **39**, 5887 (1989).

[69] R. Kobayashi, *Physica D*, **63**, 410 (1993).

[70] G. B. McFadden, A. A. Wheeler, R. J. Braun, S. R. Coriell and R. F. Sekerka, *Phys. Rev. E*, **48**, 2016 (1993).

[71] R. Kobayashi, *Exp. Math.*, **3**, 60 (1994).

[72] S-L. Wang and R. F. Sekerka, *Phys. Rev. E*, **53**, 3760 (1996).

[73] A. Karma and W. J. Rappel, *Phys. Rev. Lett.*, **77**, 4050 (1996).

[74] N. Provatas, N. Goldenfeld and J. Dantzig, *Phys. Rev. Lett.*, **80**, 3308 (1998).

[75] N. Provatas, N. Goldenfeld and J. Dantzig, *J. Comput. Phys.*, **148**, 265 (1999).

[76] N. Palle and J. Dantzig, *Metall. Mater. Trans. A*, **27**, 707 (1996).

[77] O. Zienkiewicz and J. Z. Zhu, *Int. J. Numer. Meth. Eng.*, **24**, 337, (1987).

[78] M. Plapp and A. Karma, *Phys. Rev. Lett.*, **84**, 1740 (2000).

[79] A. Karma, Y. H. Lee and M. Plapp, *Phys. Rev. E*, **61**, 3996 (2000).

[80] A. A. Wheeler, W. J. Boettinger and G. B. McFadden, *Phys. Rev. A*, **45**, 7424 (1992).

[81] A. A. Wheeler, W. J. Boettinger and G. B. McFadden, *Phys. Rev. E*, **47**, 1893 (1993).

[82] G. Caginalp and W. Xie, *Phys. Rev. E*, **48**, 1897 (1993).

[83] W. J. Boettinger and J. A. Warren, *Metall. Mater. Trans. A*, **27**, 657 (1996).

[84] W. J. Boettinger and J. A. Warren, *J. Crsyt. Growth*, **200**, 583 (1999).

[85] W. W. Mullins and R. F. Sekerka, *J. Appl. Phys.*, **35**, 444 (1964).

[86] M. J. Aziz, *J. Appl. Phys.*, **53**, 1158 (1981).

[87] R. F. Almgren, *SIAM J. Appl. Math.*, **59**, 2086 (1999).

[88] A. Karma, *Phys. Rev. Lett.*, **87**, 115701, (2001).

[89] M. S. Daw and M. I. Baskes, *Phys. Rev. Lett.*, **50**, 1285 (1983).

[90] M. S. Daw and M. I. Baskes, *Phys. Rev. B*, **29**, 6443 (1984).

[91] M. S. Daw, S. M. Foiles and M. I. Baskes, *Mater. Sci. Rep.*, **9**, 251 (1993).

[92] S. M. Foiles, M. I. Baskes and M. S. Daw, *Phys. Rev. B*, **33**, 7983 (1986).

[93] S. M. Foiles, *Phys. Rev. B*, **32**, 3409 (1985).

[94] S. M. Foiles and J. B. Adams, *Phys. Rev. B*, **40**, 5909 (1989).

[95] A. F. Voter and S. P. Chen, *Mater. Res. Soc. Symp. Proc.*, **82**, 175 (1987).

[96] F. Ercolessi and J. B. Adams, *Europhys. Lett.*, **26**, 583 (1994).

[97] H. S. Lim, C. K. Ong and F. Ercolessi, *Surf. Sci.*, **269/270**, 1109 (1992).

[98] D. Turnbull, *J. Appl. Phys.*, **21**, 1022 (1950).

[99] D. R. H. Jones, *J. Mater. Sci.*, **9**, 1 (1974).

[100] J. Q. Broughton and G. H. Gilmer, *J. Chem. Phys.*, **84**, 5759 (1986).

[101] R. L. Davidchack and B. B. Laird, *Phys. Rev. Lett.*, **85**, (2000).

[102] T. V. Ramakrishnan and M. Youssouff, *Phys. Rev. B*, **19**, 2775 (1979).

[103] A. D. J. Haymet and D. W. Oxtoby, *J. Chem. Phys.*, **74**, 2559 (1981).

[104] A. D. J. Haymet and D. W. Oxtoby, *J. Chem. Phys.*, **76**, 6262 (1982).

[105] D. W. Marr, *J. Chem. Phys.*, **102**, 8283 (1995).

[106] W. A. Curtin, *Phys. Rev. B*, **39**, 6775 (1989).

[107] W. A. Curtin and N. W. Ashcroft, *Phys. Rev. A*, **32**, 2909 (1985).

[108] J. J. Hoyt, M. Asta and A. Karma, *Phys. Rev. Lett.*, **86**, 5530 (2001).

[109] N. C. Bartelt, T. L. Einstein and E. D. Williams, *Surf. Sci.*, **312**, 411 (1994).

[110] T. Hapke, G. Pätzold and D. W. Heerman, *J. Chem. Phys.*, **109**, 10075 (1998).

[111] D. Le Floc'h, T. Saha-Dasgupta and A. Finel, *Comp. Mater. Sci.*, **8**, 192 (1997).

[112] P. J. Steinhardt, D. R. Nelson and M. Ronchetti, *Phys. Rev. B*, **28**, 784 (1983).

[113] O. Rodriguez de la Fuente and J. M. Soler, *Phys. Rev. Lett.*, **81**, 3159 (1998).

[114] W. J. Briels and H. L. Tepper, *Phys. Rev. Lett.*, **79**, 5074 (1997).

[115] C. L. Kelchner, S. J. Plimpton and J. C. Hamilton, *Phys. Rev. B*, **58**, 11085 (1998).

[116] J. J. Hoyt, M. Asta and A. Karma, to be published.

[117] J. J. Hoyt and M. Asta, to be published.

[118] J. J. Hoyt and M. Asta, unpublished research.

[119] J. R. Morris, S. Y. Lu and K. M. Ho, *Interface Science*, to be published.

[120] J. E. Angelo, M. I. Baskes and N. E. Moody, *Model. Simul. Mater. Sci. Eng.*, **3**, 289 (1995).

[121] Q. Jiang, H. X. Shi and M. Zhao, *Acta Mater.*, **47**, 2109 (1999).

[122] H. W. King, in *Physical Metallurgy*, edited by R. W. Cahn, (North-Holland, Amsterdam, 1970) p. 60.

[123] A. M. Mullis and R. F. Cochrane, *Acta Mater.*, **49**, 2205 (2001).

[124] S. R. Coriell and D. Turnbull, *Acta Metall.*, **30**, 2135 (1982).

[125] J. Q. Broughton, G. H. Gilmer and K. A. Jackson, *Phys. Rev. Lett.*, **49**, 1496 (1982).

[126] E. Burke, J. Q. Broughton and G. H. Gilmer, *J. Chem. Phys.*, **89**, 1030 (1988).

[127] J. J. Hoyt, M. Asta and A. Karma, *Interface Science*, to be published.

[128] H. A. Wilson, *Philos. Mag.*, **50**, 238 (1900).

[129] J. Frenkel, *Phys. Z. Sowjetunion*, **1**, 498 (1932).

[130] F. C. Celestini and J.-M. Debierre, *Phys. Rev. B,* **62**, 14006 (2000).

[131] F. C. Celestini, private communication.

[132] J. J. Hoyt, B. Sadigh, M. Asta and S. M. Foiles, *Acta Mater.*, **47**, 3181 (1999).

[133] C. J. Tymczak and J. R. Ray, *Phys. Rev. Lett.*, **64**, 1278 (1990).

[134] K. A. Jackson in *Treatise on Solid State Chemistry*, Vol. 5, edited by N. B. Hannay (Plenum Press, NY, 1975) p. 233.

[135] K. A. Jackson, Interface Science, to be published.

[136] H. E. A. Huitema, M. J. Vlot and J. P. van der Eerden, *J. Chem. Phys.*, **111**, 4714 (1999).

[137] J. P. Hansen and I. R. McDonald, *Theory of Simple Liquids*, (Academic Press, London, 1976).

[138] R. J. Reynik, *Appl. Phys. Lett.*, **9**, 239 (1966).

[139] M. M. G. Allemany, C. Rey and L. J. Gallegos, *Phys. Rev. B*, **58**, 685 (1998).

[140] M. M. G. Allemany, C. Rey and L. J. Gallegos, *J. Chem. Phys.*, **109**, 5175 (1998).

[141] J. Henderson and L. Yang, *Trans. Am. Inst. Min. Engrs.*, **221**, 72 (1961).

[142] A. Pasquarello, K. Laasonen, R. Car, C. Lee and D. Vanderbilt, *Phys. Rev. Lett.*, **69**, 1982 (1992).

[143] M. Dzugutov, *Nature*, **381**, 137 (1996).

[144] Y. Rosenfeld, E. Nardi and Z. Zinamon, *Phys. Rev. Lett.*, **75**, 2490 (1995).

[145] S. Chapman and T. G. Cowling, *The Mathematical Theory of Non-Uniform Gases*, (Cambridge University Press, London, 1970).

[146] J. J. Hoyt, M. Asta and B. Sadigh, *Phys. Rev. Lett.*, **85**, 594 (2000).

[147] F. H. Stillinger and T. A. Weber, *Phys. Rev. B*, **29**, 6443 (1984).

[148] R. Car and M. Parinello, *Phys. Rev. Lett.*, **55**, 2471 (1985).

[149] G. Kresse and J. Hafner, *Phys. Rev. B*, **47**, 558 (1993).

[150] G. Kresse and J. Hafner, *Phys. Rev. B*, **49**, 14251(1994).

[151] G. Kresse and J. Furthmuller, *Comput. Mater. Sci.*, **6**, 15 (1996).

[152] G. Kresse and J. Furthmuller, *Phys. Rev. B*, **54**, 11169 (1996).

[153] G. Kresse and J. Hafner, *Phys. Rev. B*, **48**, 13115 (1993).

[154] F. Kirchoff, G. Kresse and M. J. Gillan, *Phys. Rev. B*, **57**, 10482 (1998).

[155] D. Alfe and M. J. Gillan, *Phys. Rev. Lett.*, **81**, 5161 (1998).

[156] D. Alfe and M. J. Gillan, *Phys. Rev. B*, **58**, 8248 (1998).

[157] D. Alfe, G. Kresse and M. J. Gillan, *Phys. Rev. B*, **61**, 132 (2000).

[158] G. A. de Wijs, G. Kresse, L. Vocadlo, D. Donson, D. Alfe, M. J. Gillan and G. D. Price, *Nature (London),* **392**, 805 (1998).

[159] K. Seifert-Lorenz and J. Hafner, *Phys. Rev. B*, **59**, 843 (1999).

[160] M. Asta, V Ozolins, J. J. Hoyt and M. van Schilgaarde, *Phys. Rev. B*, **64**, 020201-1 (2001).

[161] M. Asta, D. Morgan, J. J. Hoyt, B. Sadigh, J. D. Althoff, D. de Fontaine and S. M. Foiles, *Phys. Rev. B*, **59**, 14271 (1999).

[162] H. E. A. Huitema, B. van Hengstum and J. P. van der Eerden, *J. Chem. Phys.*, **111**, 10248 (1999).

[163] Q. M. Yu, M. O. Thompson and P. Clancy, *Phys. Rev. B*, **53**, 8386 (1996).

[164] R. L. Davidchack and B. B. Laird, *Phys. Rev. E*, **54**, R5905 (1996).

[165] R. L. Davidchack and B. B. Laird, *Mol. Phys.*, **97**, 833 (1999).

[166] T. Akamatsu and K. Kawamura, *Mol. Simul.*, **21**, 387 (1999).

[167] H. Ramalingam, M. Asta, A. van de Walle and J. J. Hoyt, *Interface Science*, to be published.

[168] S. M. Foiles, *Phys. Rev. B*, **32**, 7685 (1985).

[169] R. Willnecker, D. M. Herlach and B. Feuerbacher, *Phys. Rev. Lett.*, **62**, 2707 (1989).

[170] J. W. Lum, D. M. Matson and M. C. Flemings, *Metall. Mater. Trans. B*, **27**,865 (1996).

[171] D. M. Matson, in *Solidification 1998*, edited by S. P. Marsh, J. A. Dantzig, R. Trivedi, W. Hofmeister, M. G. Chu, E. J. Lavernia and J.-H. Chun, The Minerals, Metals and Materials Society, p. 233 (1998).

[172] J. W. Walker, in *Principles of Solidification*, edited y B. Chalmers (John Wiley and Sons, Inc., New York, 1964) p. 114.

7. Tables and Figures

Table I. Summary of melting points, solid-liquid interfacial free energies and anisotropies for various EAM pure metals.

Fig. 3.1 a) Top, plot of the average order parameter ϕ vs. the y direction at a point along the solid-liquid boundary. Results were obtained from a single configuration during an MD simulation of Ni. b) Bottom, Portion of the solid-liquid interface obtained from one snapshot of an MD simulation for the 100[010] orientation. Solid atoms are shaded gray and liquid atoms are white (see text). Superimposed as a thick line is the interface position corresponding to the $\phi = .7$ contour.

Fig. 3.2 Log-log plot of the fluctuation spectra, $\left\langle |A(k)|^2 \right\rangle$ vs. k, for pure Ni in three crystal orientations. The solid lines indicate a slope of k^{-2} (see eq. 3.4).

Fig. 3.3 $1/bW\left\langle |A(k)|^2 \right\rangle$ vs. k^2 for three crystal orientations for pure Ni. The slopes of the lines are proportional to the interface stiffness and a clear anisotropy is observed.

Fig. 3.4 Fluctuation spectra for EAM Cu.

Fig. 3.5 $1/bW\left\langle |A(k)|^2 \right\rangle$ vs. k^2 for EAM Au.

Fig. 3.6 Initial configuration of atoms used in the simulation of solid-liquid interface motion. The example shown is for pure Ni.

Fig. 3.7 Velocity of the solid-liquid boundary as a function of undercooling in pure Au for the low index directions 100, 110 and 111. The slopes of the curves at the low undercooling, as shown by the heavy lines, yield the kinetic coefficient.

Fig. 3.8 Exponential decay constant, τ, normalized by the quantity Γ, vs. k^2. The slope of the lines is proportional to the kinetic coefficient μ.

Fig. 3.9 Comparison of the interface velocity according to the model of BGJ and those obtained from MD simulations. The data symbols represent free solidification results.

Fig. 3.10 Velocity vs. undercooling in the 111 direction for pure Au using two different cell sizes. The slower growth observed for the large size system is consistent with the findings of Burke et al. [126].

Fig. 3.11 Plane of atoms parallel to the solid-liquid boundary but located well within the solid phase. The white atoms are those which belong to the solid phase whereas the gray atoms denote liquid like or "defect" atoms. Deep within the solid there exists only a few defective atoms.

Fig. 3.12 Plane of atoms parallel to the solid-liquid interface but located well within the liquid phase. Most of the atoms are liquid like and no six fold symmetry is observed.

Fig. 3.13 Plane of atoms at the solid-liquid boundary. Clusters of defect (ie. gray) atoms are observed which possess six fold symmetry as indicated by the heavy solid lines. Such regions represent stacking faults as can be seen by the offset of the atom planes from the perfect FCC configuration (the light solid lines).

Fig. 3.14 Mean square displacement of Ni atoms as a function of time for two different temperatures. The slope of the lines at long times is proportional to the diffusion coefficient.

Fig. 3.15 The velocity-velocity correlation function normalized by its value at $t = 0$ vs. time for 1600 and 2000 K in Ni. The integral of the curves over all times yields the diffusion coefficient.

Fig. 3.16 The diffusion coefficient of pure Cu (filled circles) and Ni (filled squares) as a function of temperature. The vertical lines label the EAM melting points. The symbols filled with a cross are the results of Alemany et al. [139,140] and the open circles are the experimental results of Henderson and Yang [141]. The symbol filled with "+" is the ab-initio result from Pasquarello et al. [142].

Fig. 3.17 Log of the scaled diffusion coefficient D^* vs. the excess entropy for a variety of EAM metals and alloys and for Si using the Stillinger-Weber potential [147].

Fig. 3.18 Mean square displacement of Ni and Al atoms vs. time in liquid $Ni_{20}Al_{80}$ using first principles atomistic computations (VASP). The temperature of the simulation was 1700K.

Fig. 3.19 Fluctuation spectra for Cu-Ni at 1750K. The composition of the liquid phase was approximately $X_{Cu} = 10.1\%$ and for the solid $X_{Cu} = 5.0\%$.

Fig. 4.1 Dendrite velocity vs. undercooling in pure Ni computed using 3D phase field simulations (solid line) by Bragard et al. [45]. Open symbols are the experimental results by Willnecker et al. [169] and Lum et al. [170]. The kinetic coefficient, as well as the crystalline and kinetic anisotropy, were taken from MD studies and therefore there are no adjustable parameters in the phase field model.

Table I

	T_M (^oK)	γ_o (mJ/m^2)	$(\gamma_{100}-\gamma_{110})/2\gamma_o$ (%)
Ni (FBD)	1700 (1726)	326 (255)	1.8
Ni (VC)	1630	306	1.4
Ni (ABM)	1440	271	1.4
Cu (VC)	1270 (1356)	210 (177)	1.5
Au (VC)	1120 (1235)	147 (132, 270)	1.6
Ag (VC)	1115 (1297)	133	1.1
Pb (LOE)	615 (600)	41.6 (33,40)	0.9
Al (EA)	925 (933)	115 (93)	1.5

Fig. 3.1a

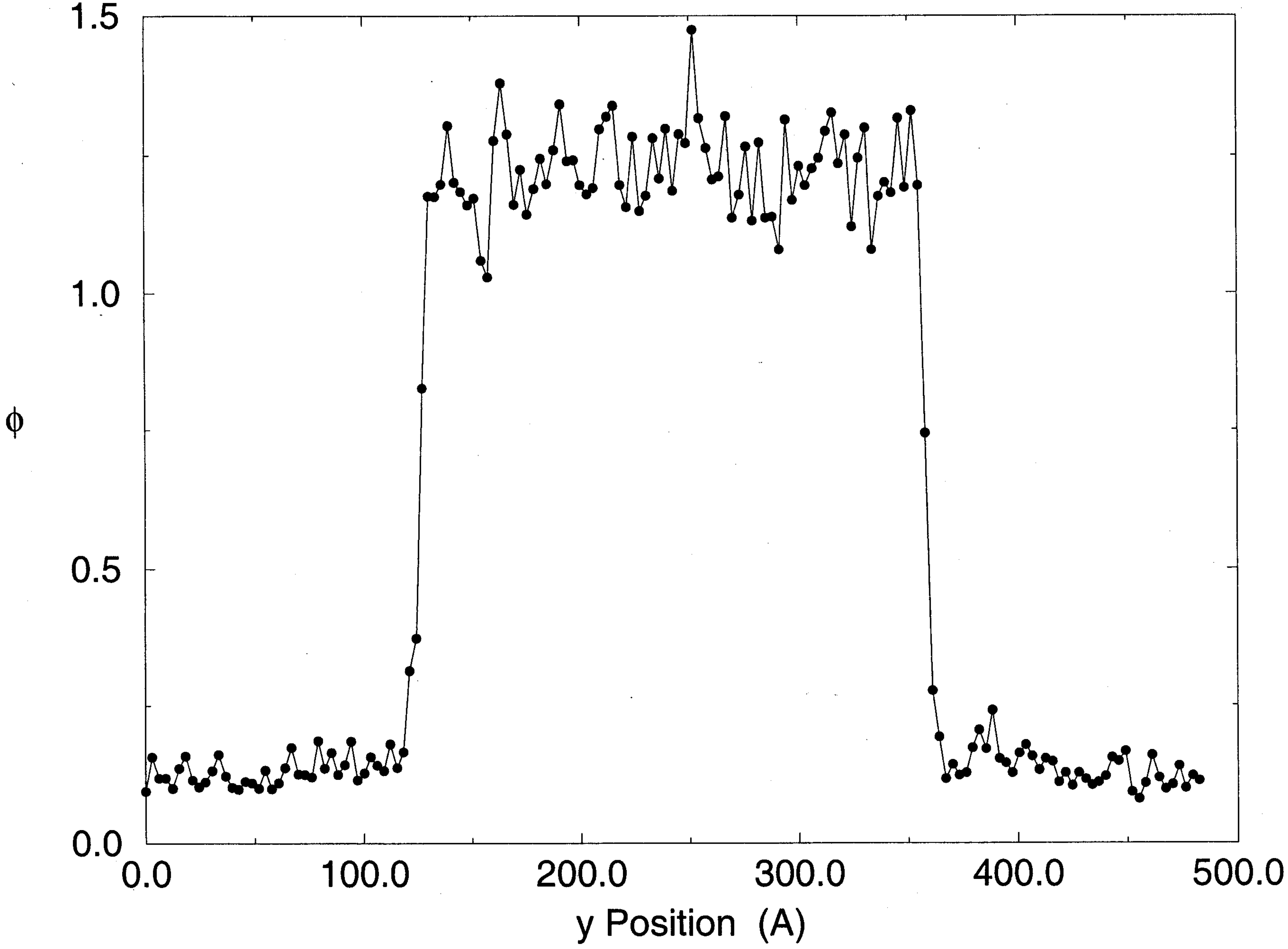

Fig. 3.1b

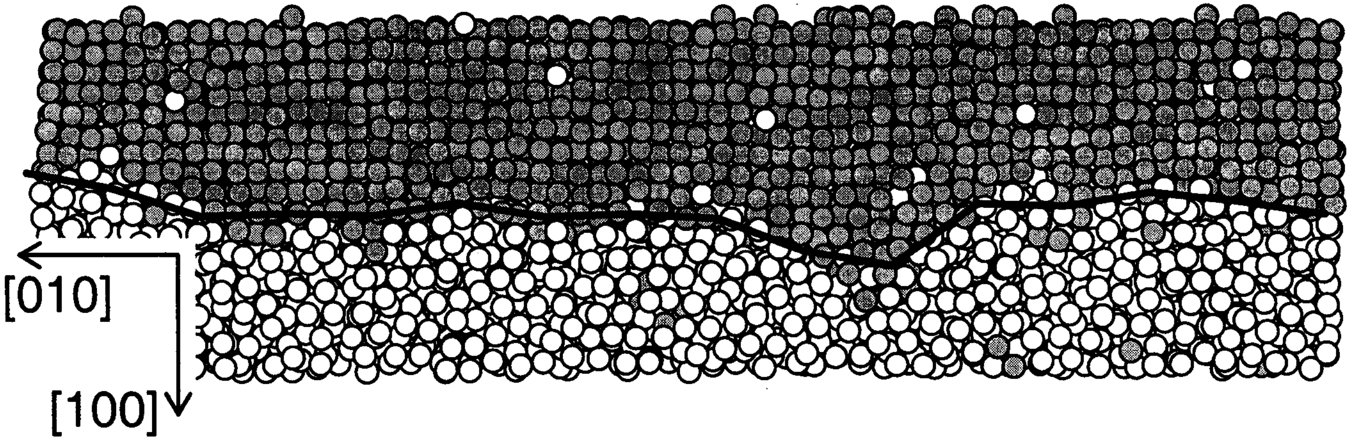

Fig. 3.2

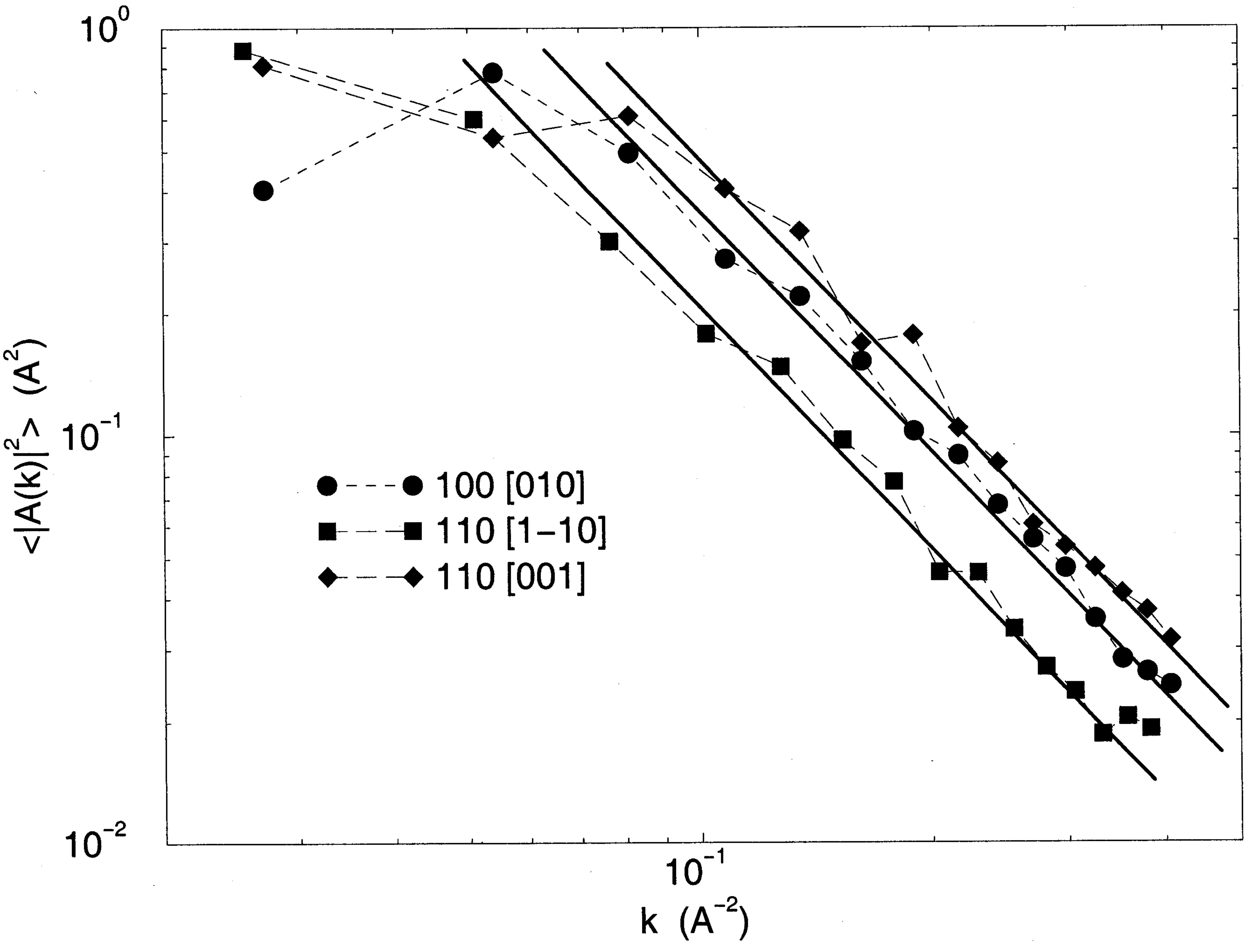

Fig. 3.3

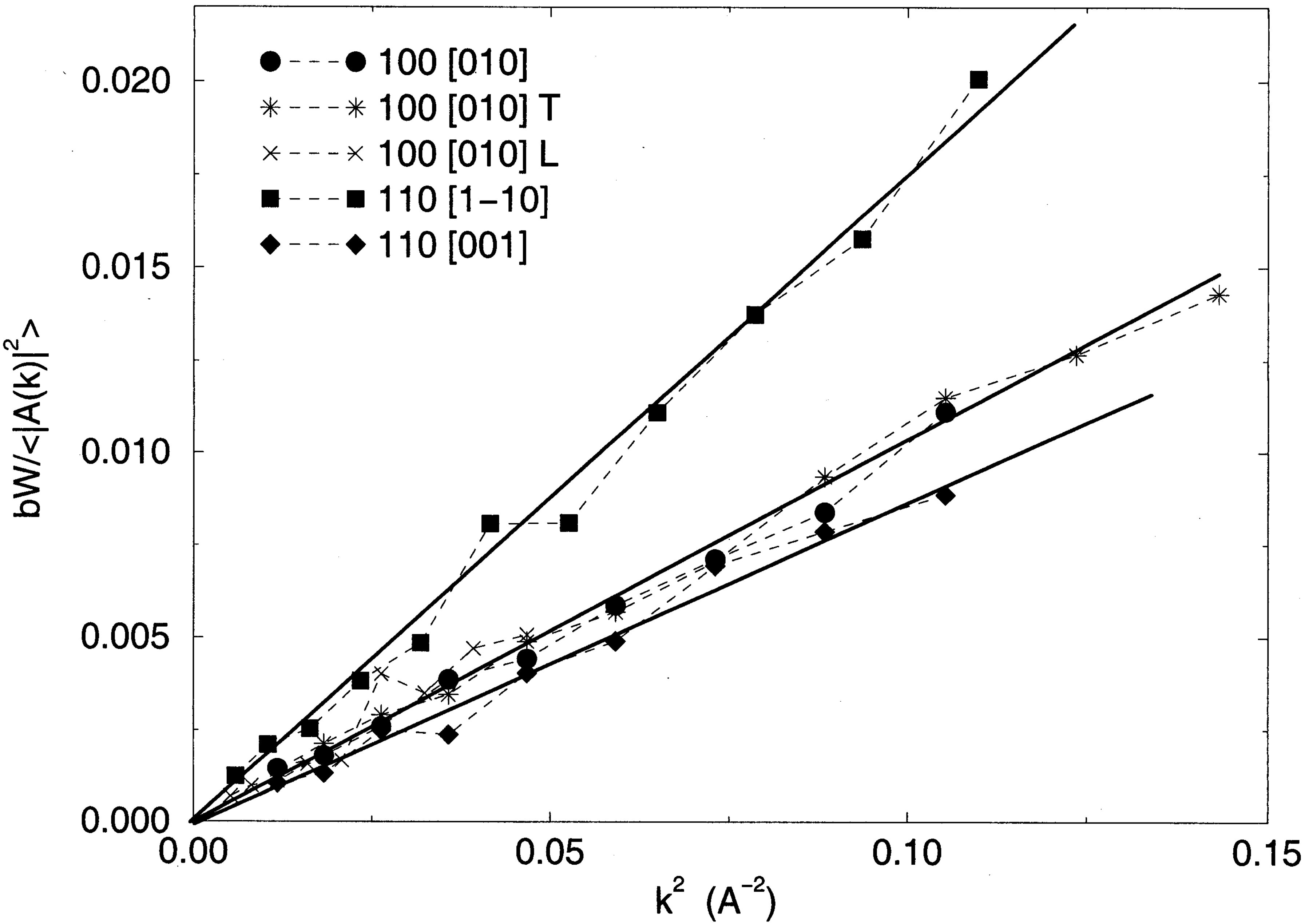

● - - - ● 100 [010]
✳ - - - ✳ 100 [010] T
× - - - × 100 [010] L
■ - - - ■ 110 [1−10]
◆ - - - ◆ 110 [001]
bW/<|A(k)|²>
0.000
0.005
0.010
0.015
0.020
0.00
0.05
0.10
0.15
k² (A⁻²)

Fig. 3.4

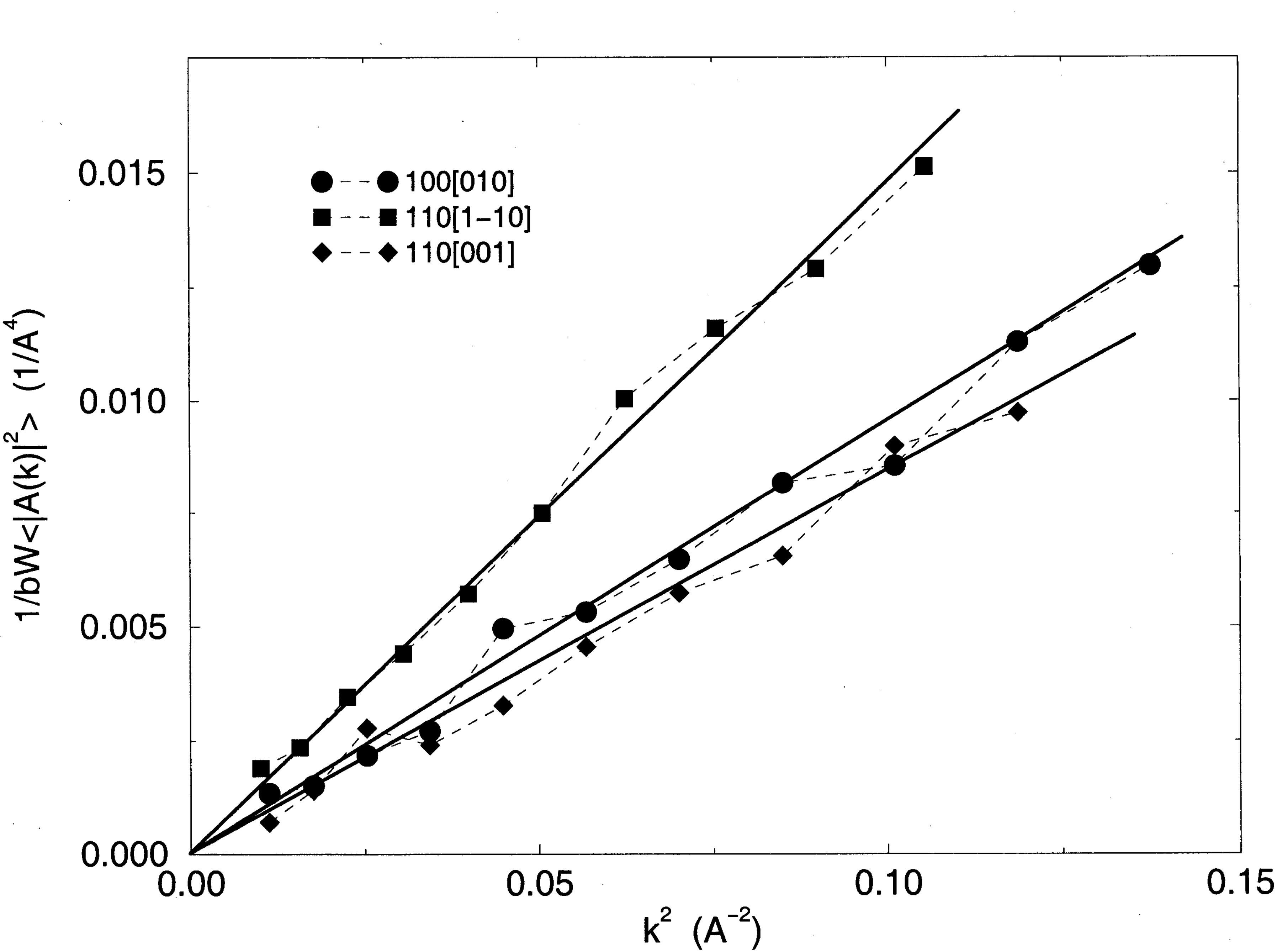
100[010]
110[1-10]
110[001]
0.000
0.005
0.010
0.015
0.00
0.05
0.10
0.15
1/bW<|A(k)|²> (1/A⁴)
k² (A⁻²)

Fig. 3.5

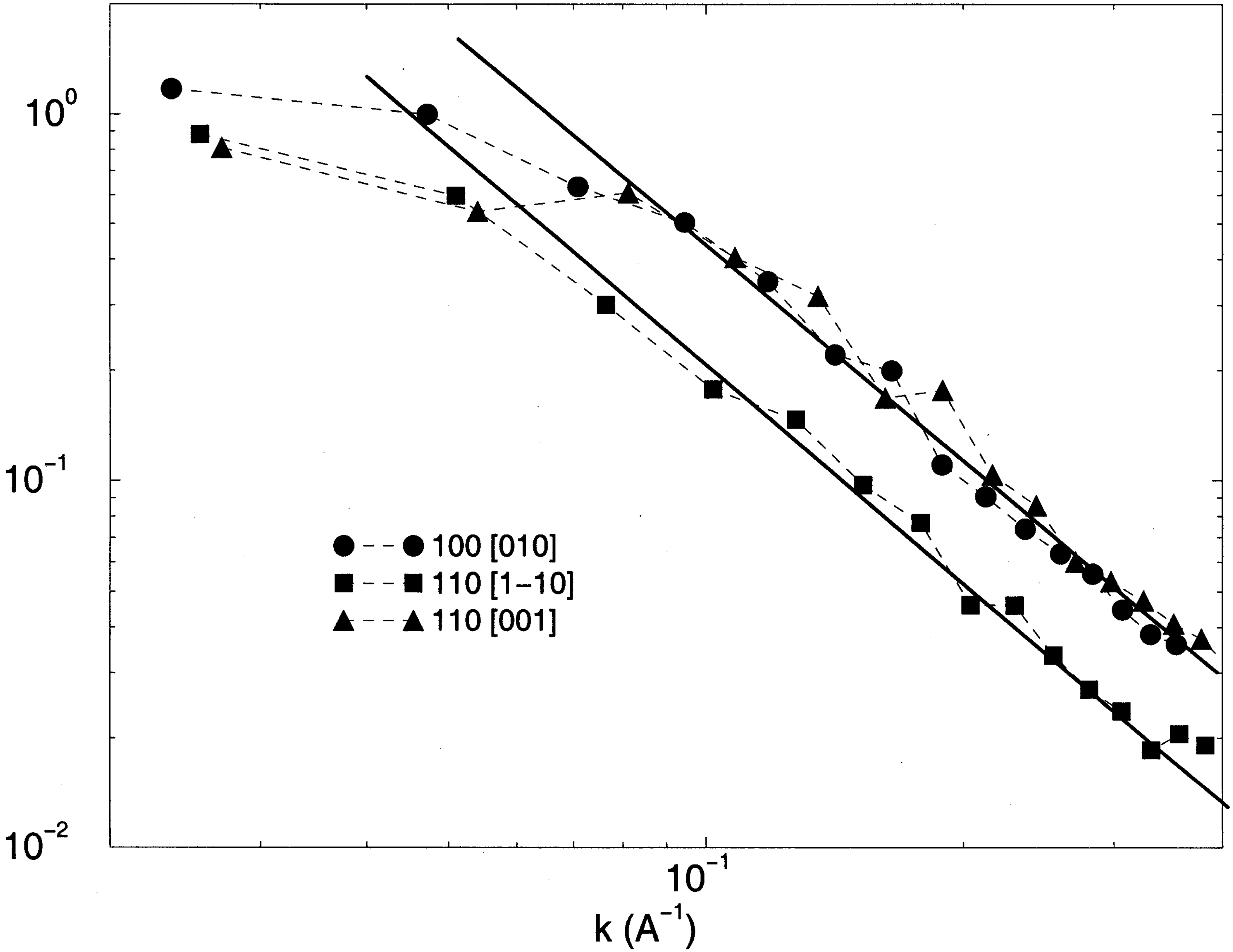

Fig. 3.6

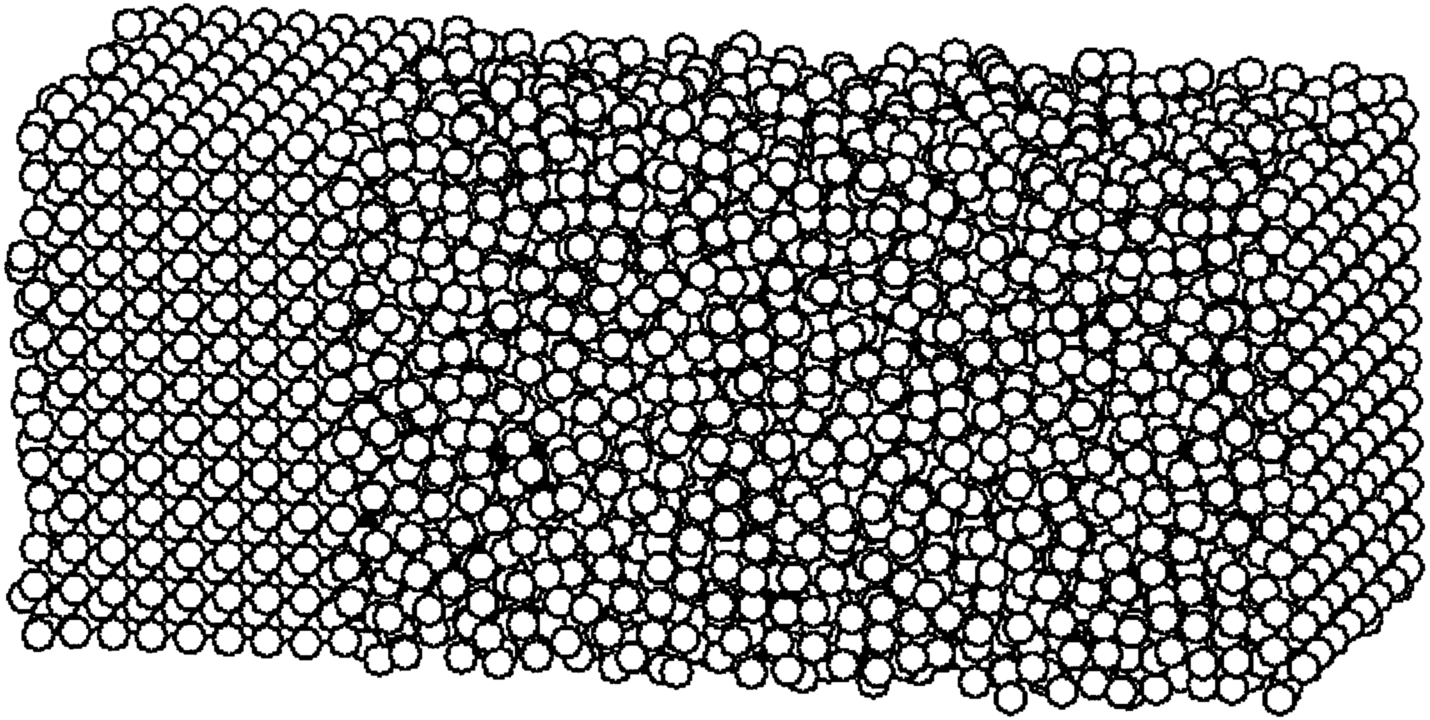

Fig. 3.7

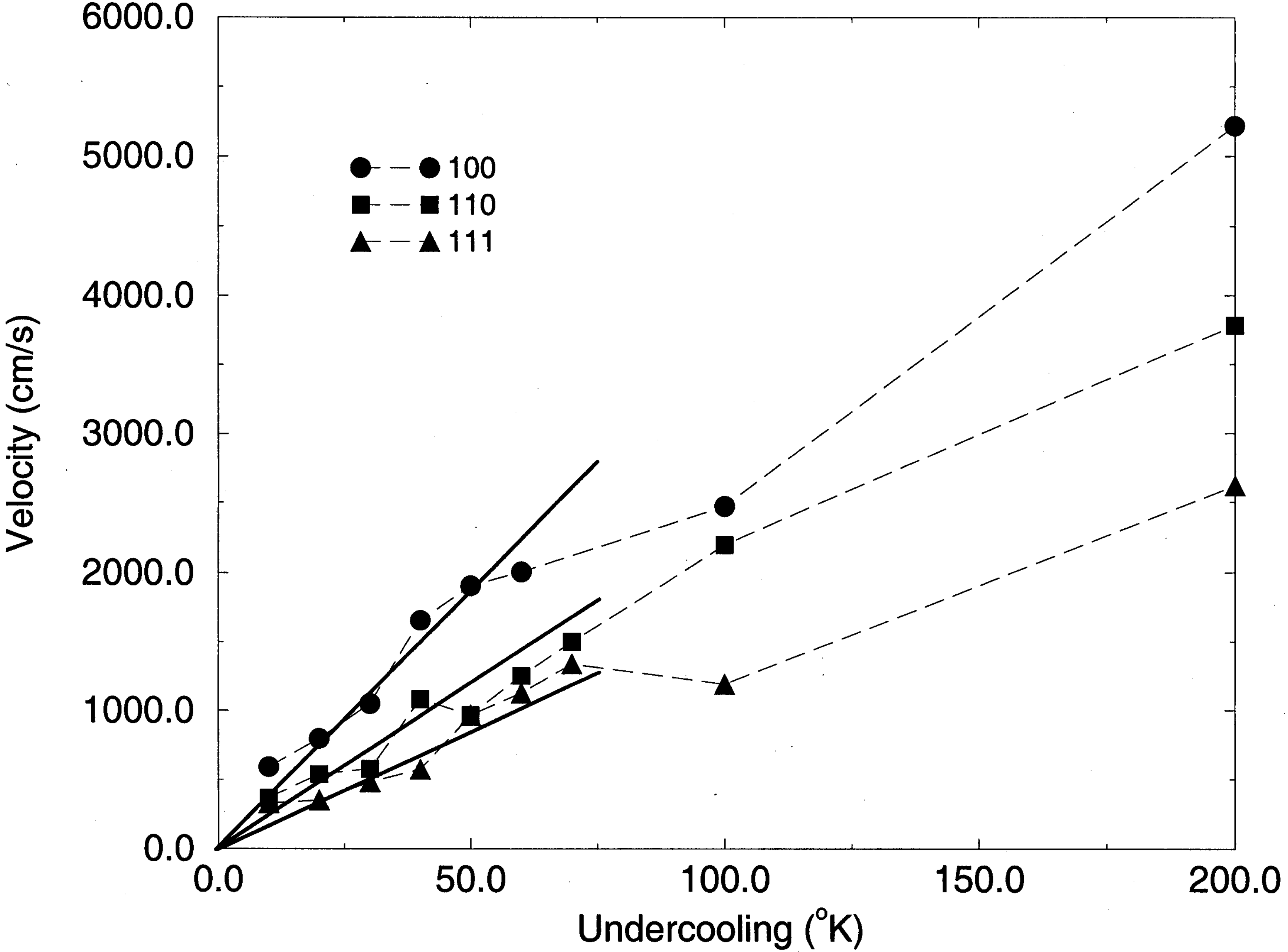
6000.0
5000.0
4000.0
3000.0
2000.0
1000.0
0.0
Velocity (cm/s)
0.0
50.0
100.0
150.0
200.0
Undercooling (°K)
● — ● 100
■ — ■ 110
▲ — ▲ 111

Fig. 3.8

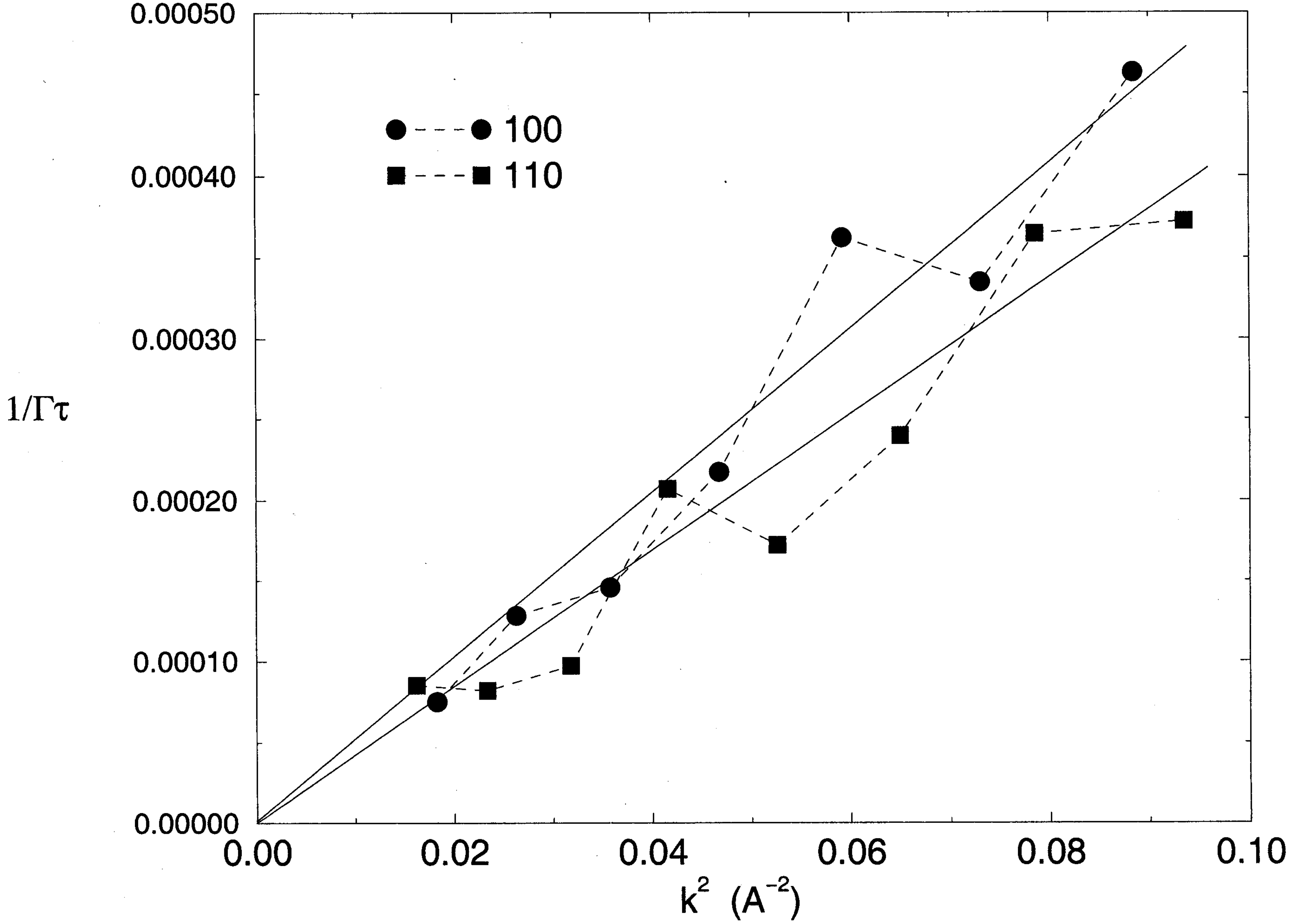

100
110
1/Γτ
0.00000
0.00010
0.00020
0.00030
0.00040
0.00050
0.00
0.02
0.04
0.06
0.08
0.10
k^2 (A^{-2})

Fig. 3.9

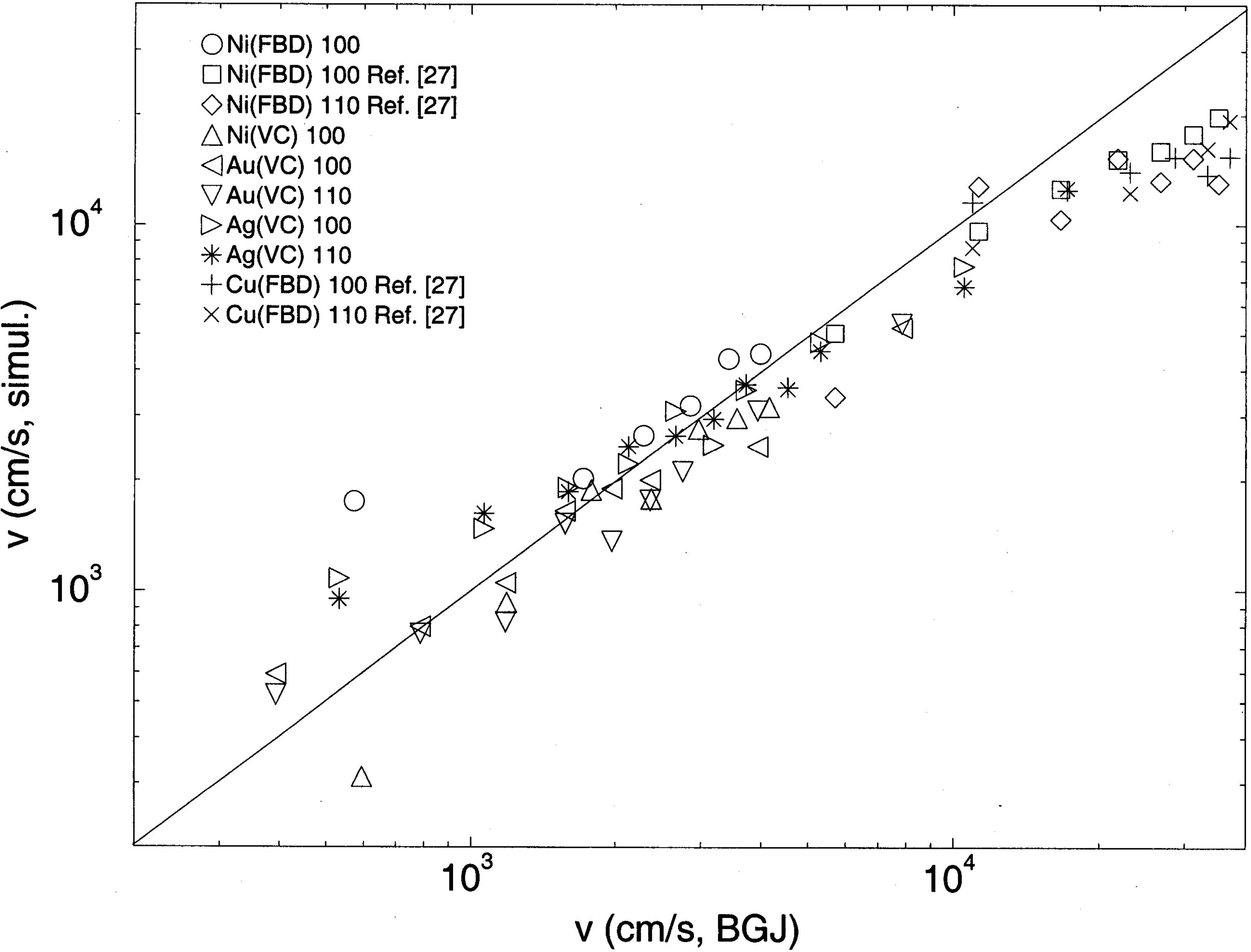
○ Ni(FBD) 100
□ Ni(FBD) 100 Ref. [27]
◇ Ni(FBD) 110 Ref. [27]
△ Ni(VC) 100
◁ Au(VC) 100
▽ Au(VC) 110
▷ Ag(VC) 100
✳ Ag(VC) 110
+ Cu(FBD) 100 Ref. [27]
× Cu(FBD) 110 Ref. [27]
10^4
10^3
v (cm/s, simul.)
10^3
10^4
v (cm/s, BGJ)

Fig. 3.10

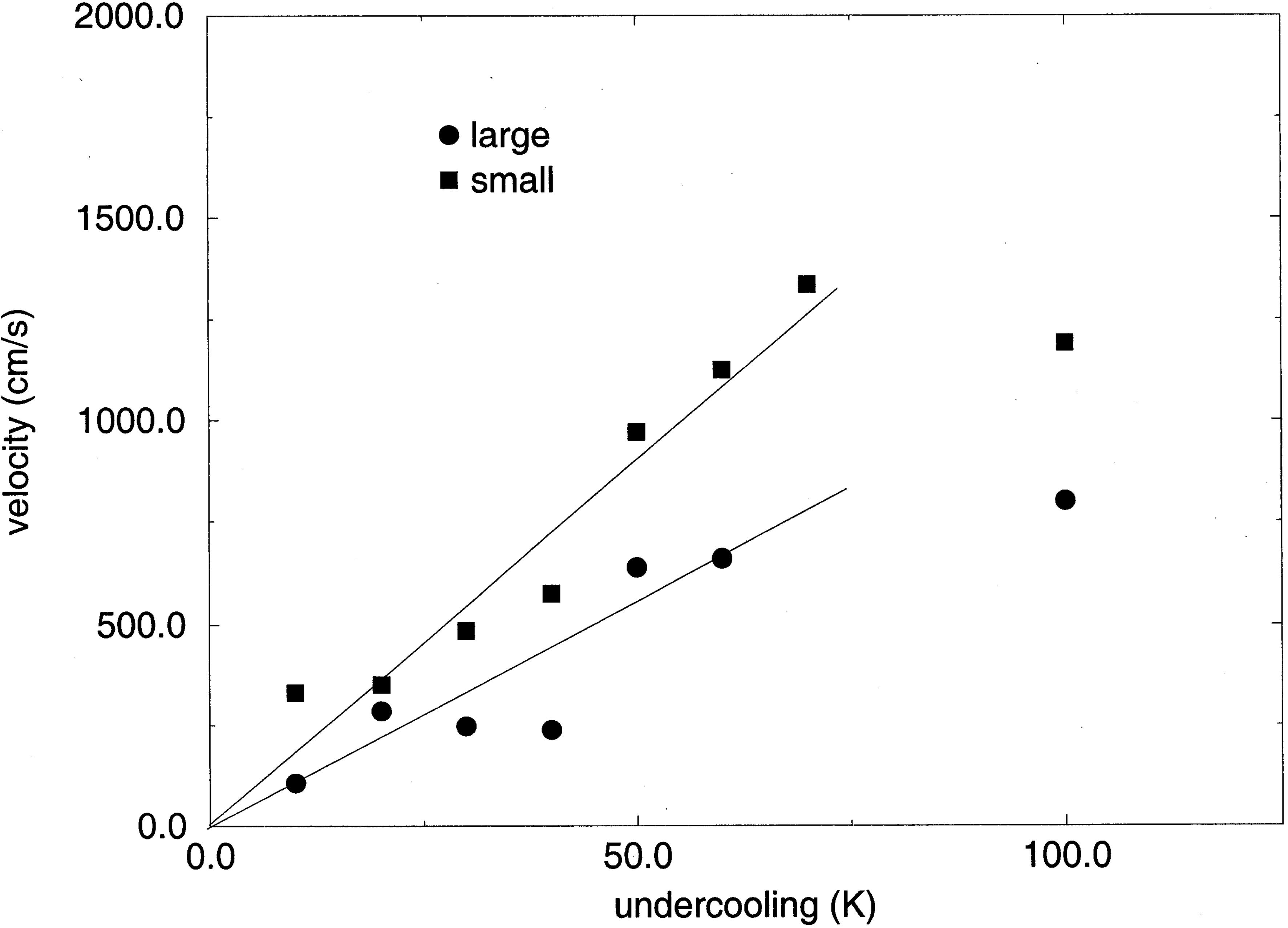
2000.0
1500.0
1000.0
500.0
0.0
velocity (cm/s)
● large
■ small
0.0
50.0
100.0
undercooling (K)

Fig. 3.11

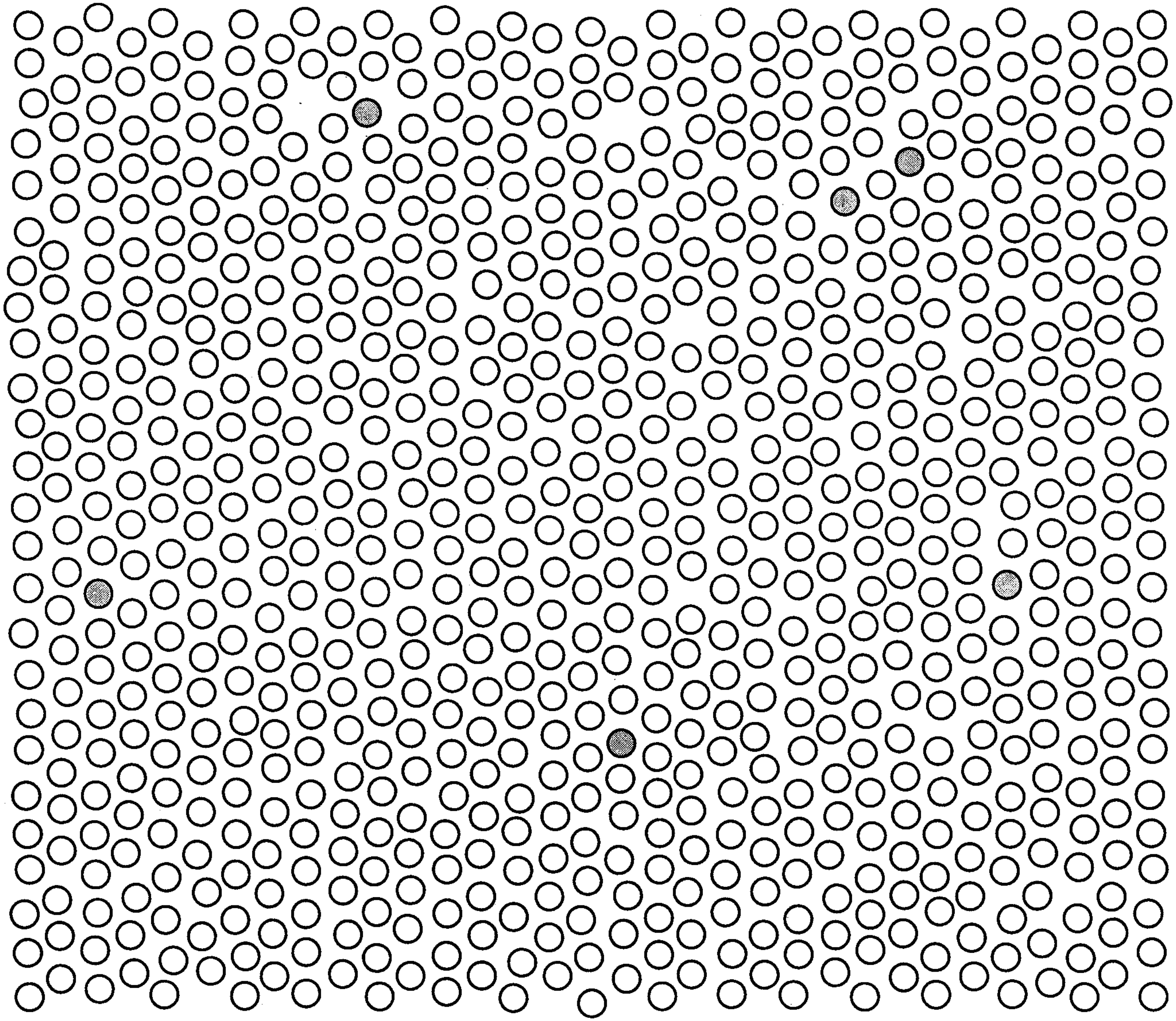

Fig. 3.12

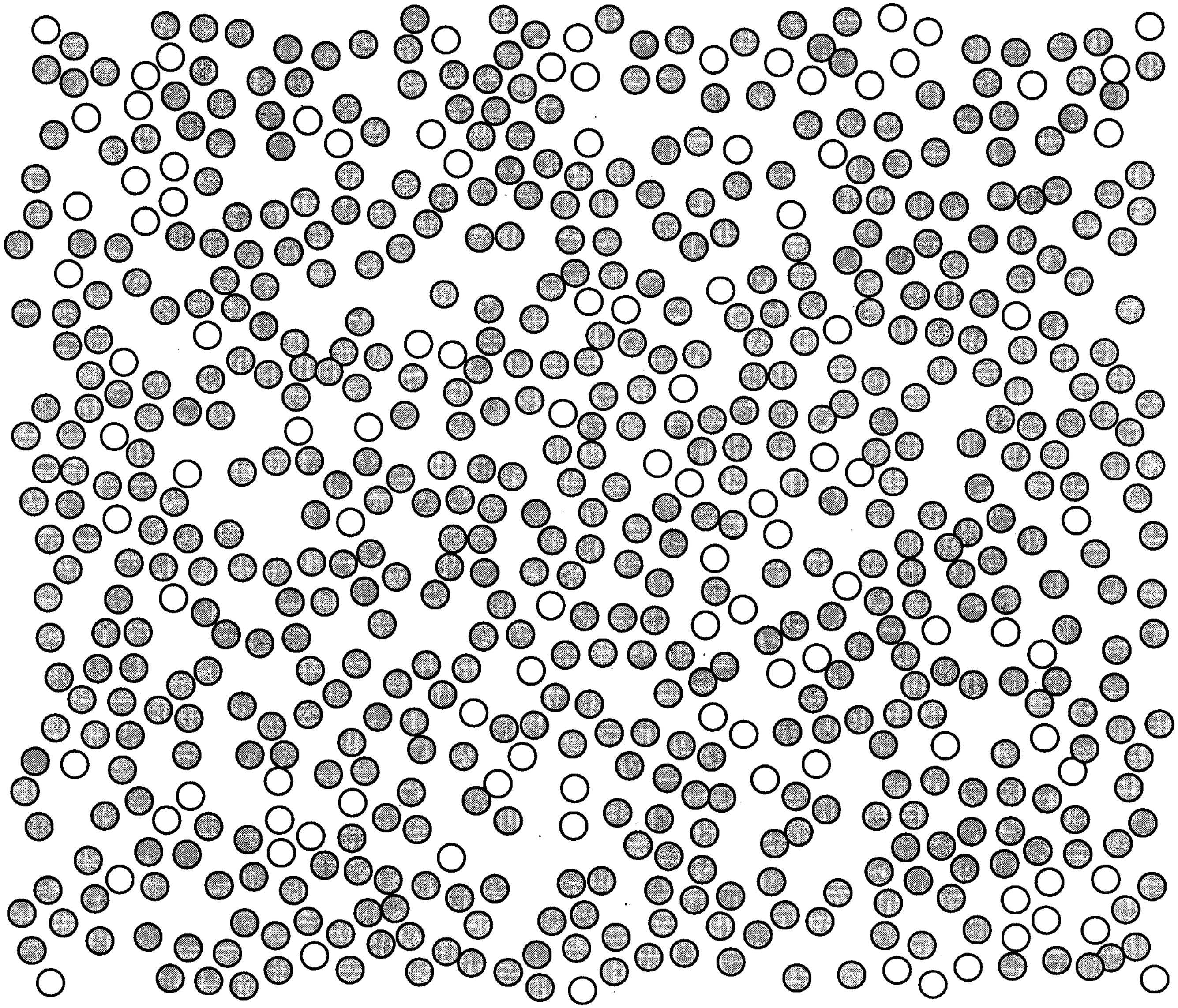

Fig. 3.13

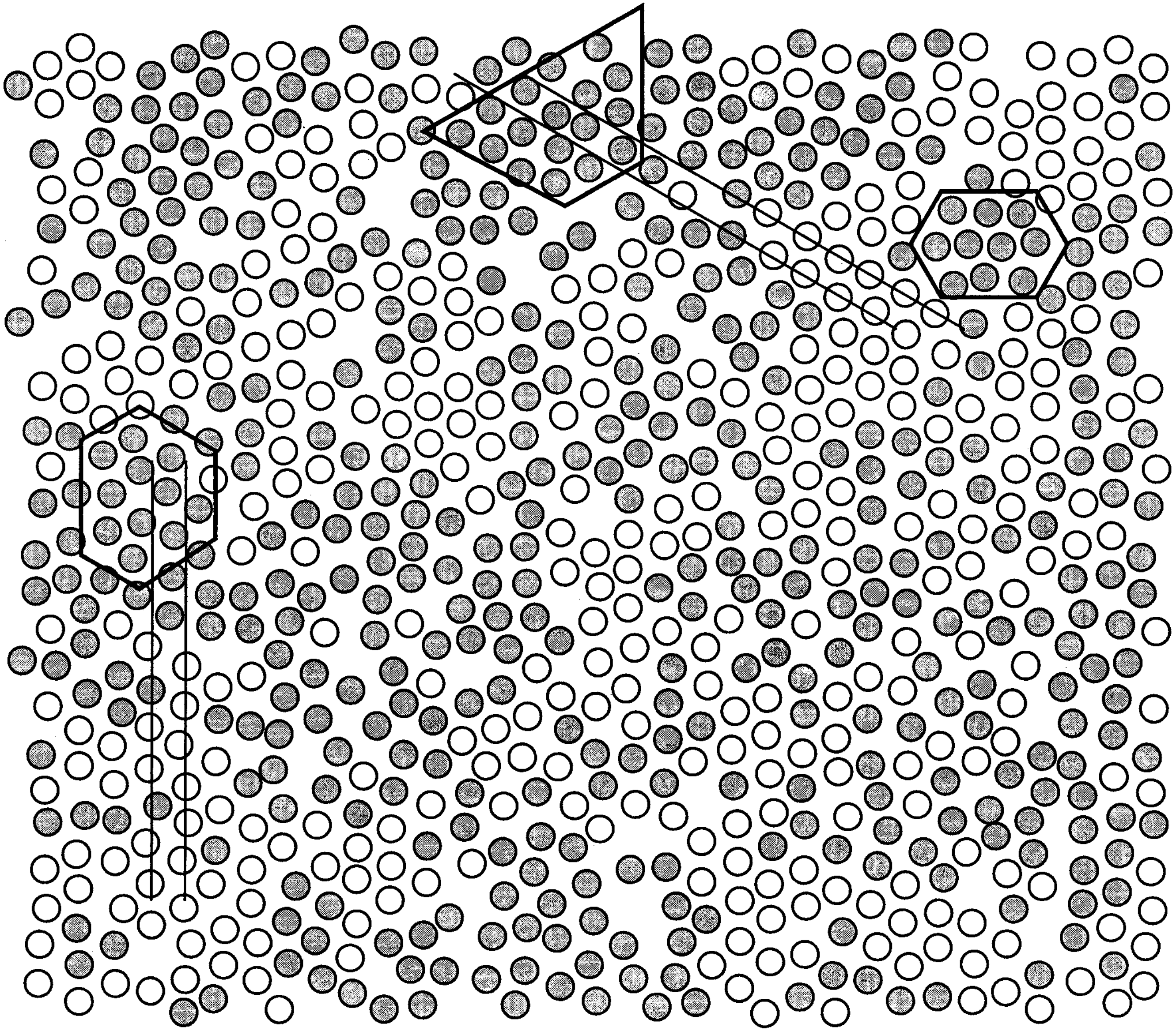

Fig. 3.14

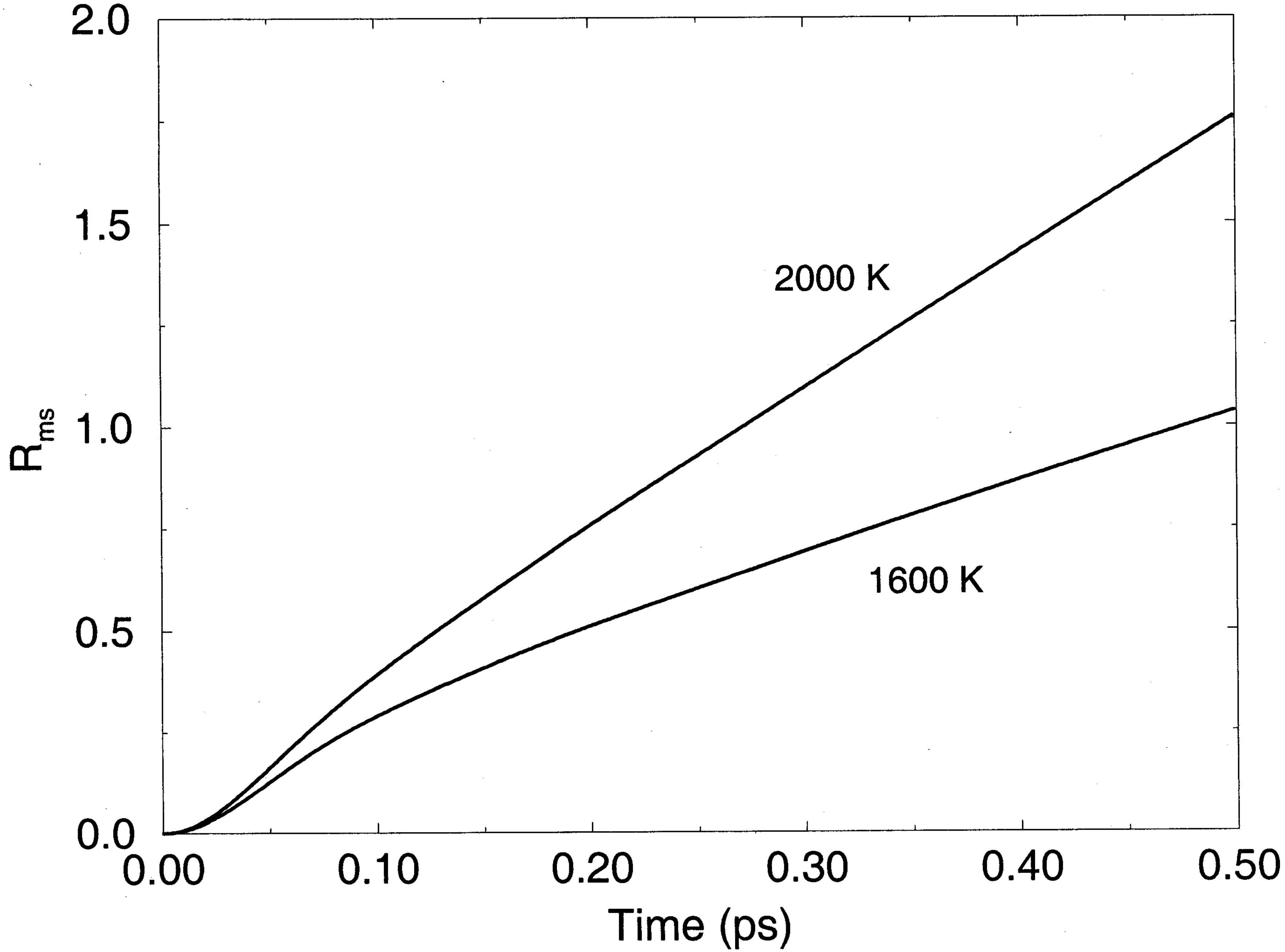

Fig. 3.15

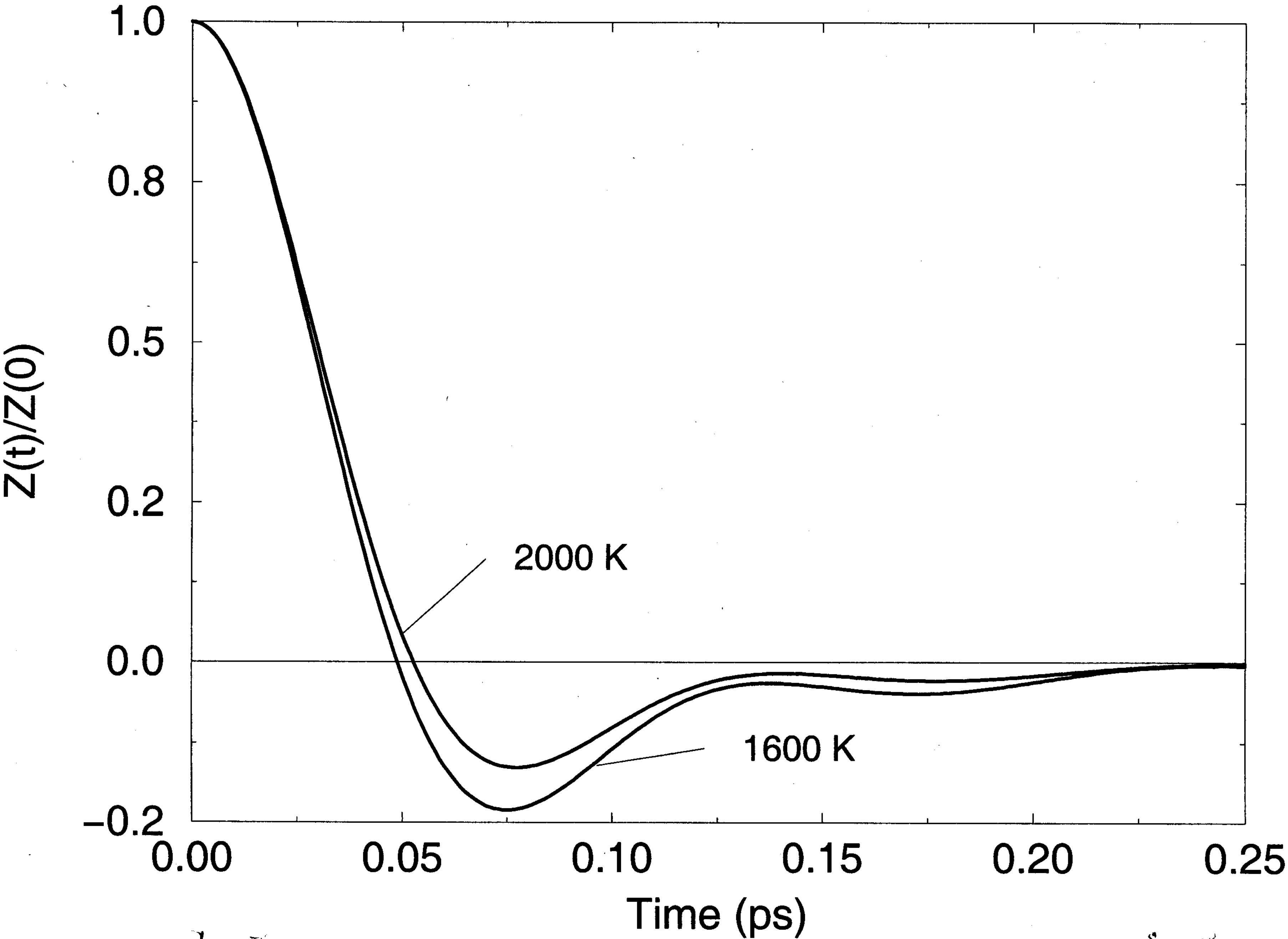
1.0
0.8
0.5
0.2
0.0
−0.2
Z(t)/Z(0)
0.00
0.05
0.10
0.15
0.20
0.25
Time (ps)
2000 K
1600 K

Fig. 3.16

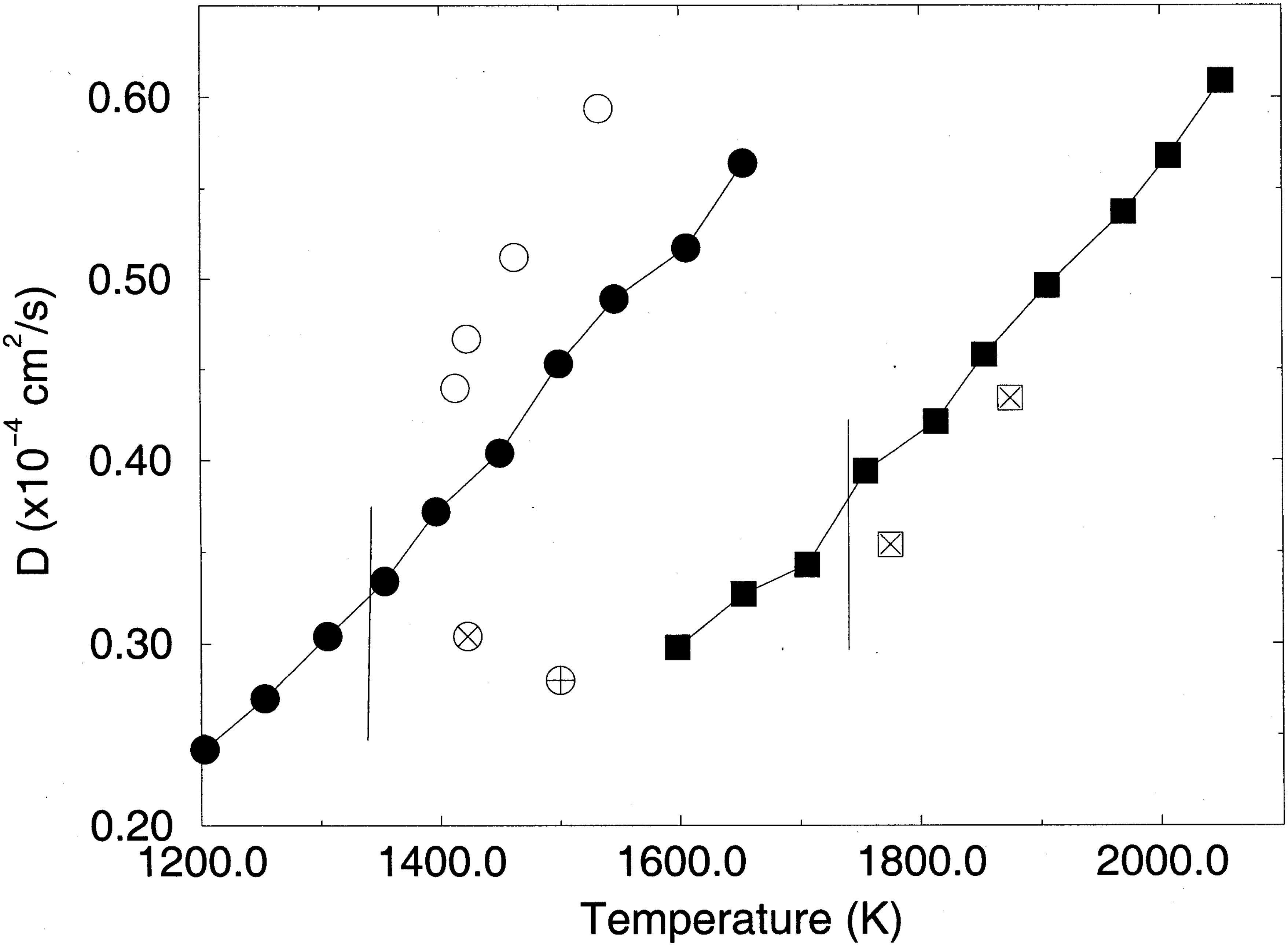
D (x10^{-4} cm^2/s)
0.20
0.30
0.40
0.50
0.60
1200.0
1400.0
1600.0
1800.0
2000.0
Temperature (K)

Fig. 3.17

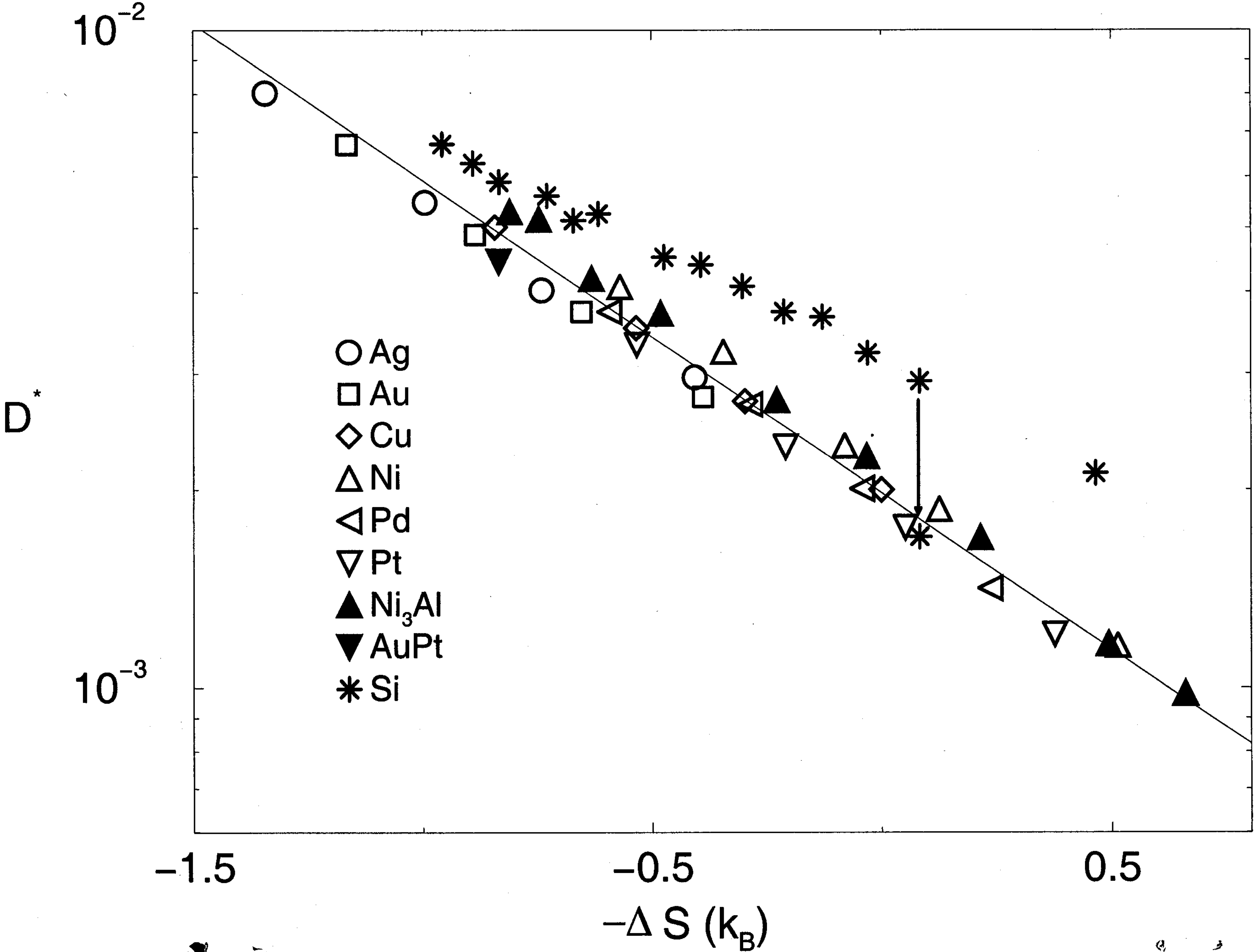

Fig. 3.18

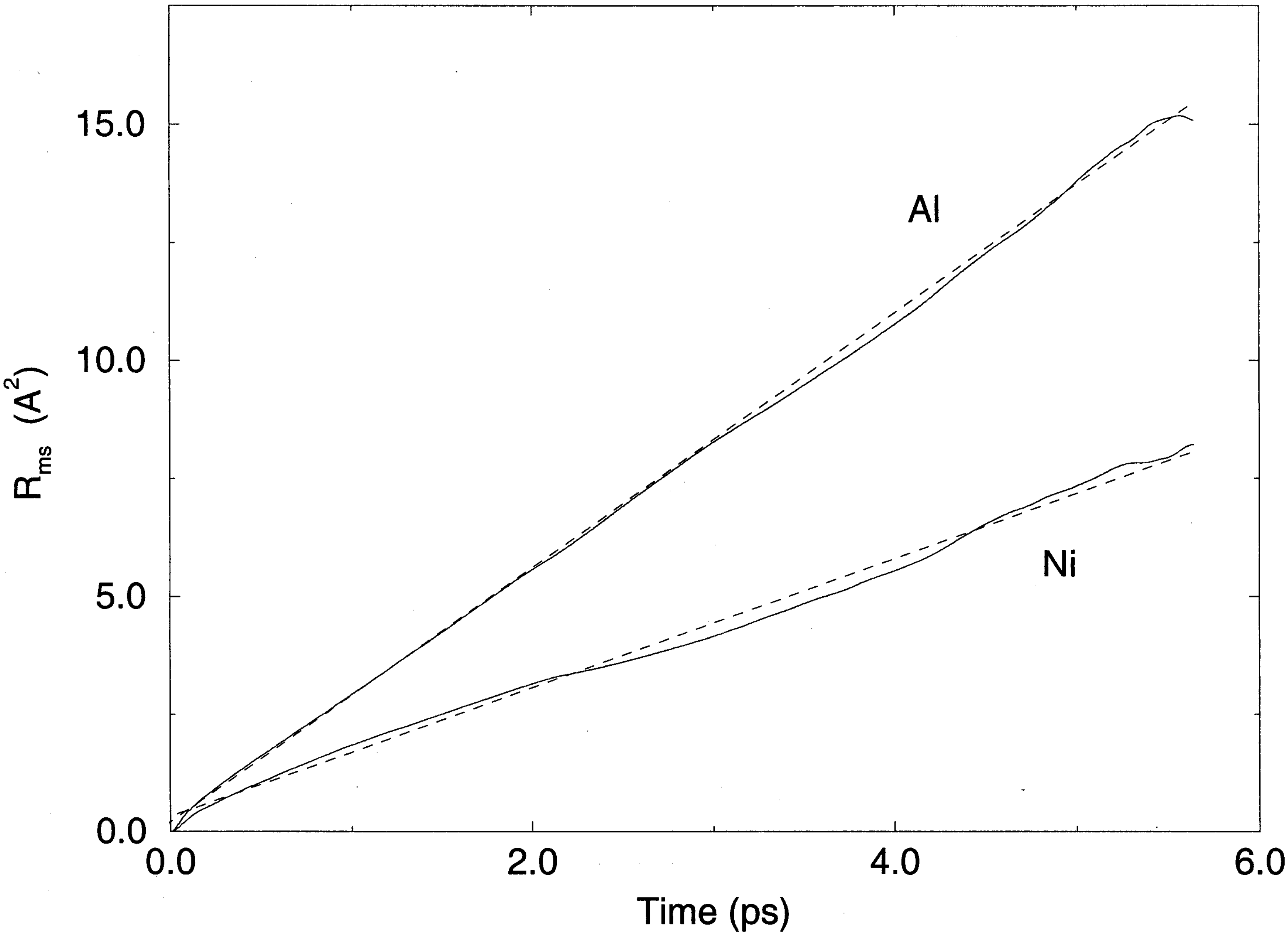

Fig. 3.19

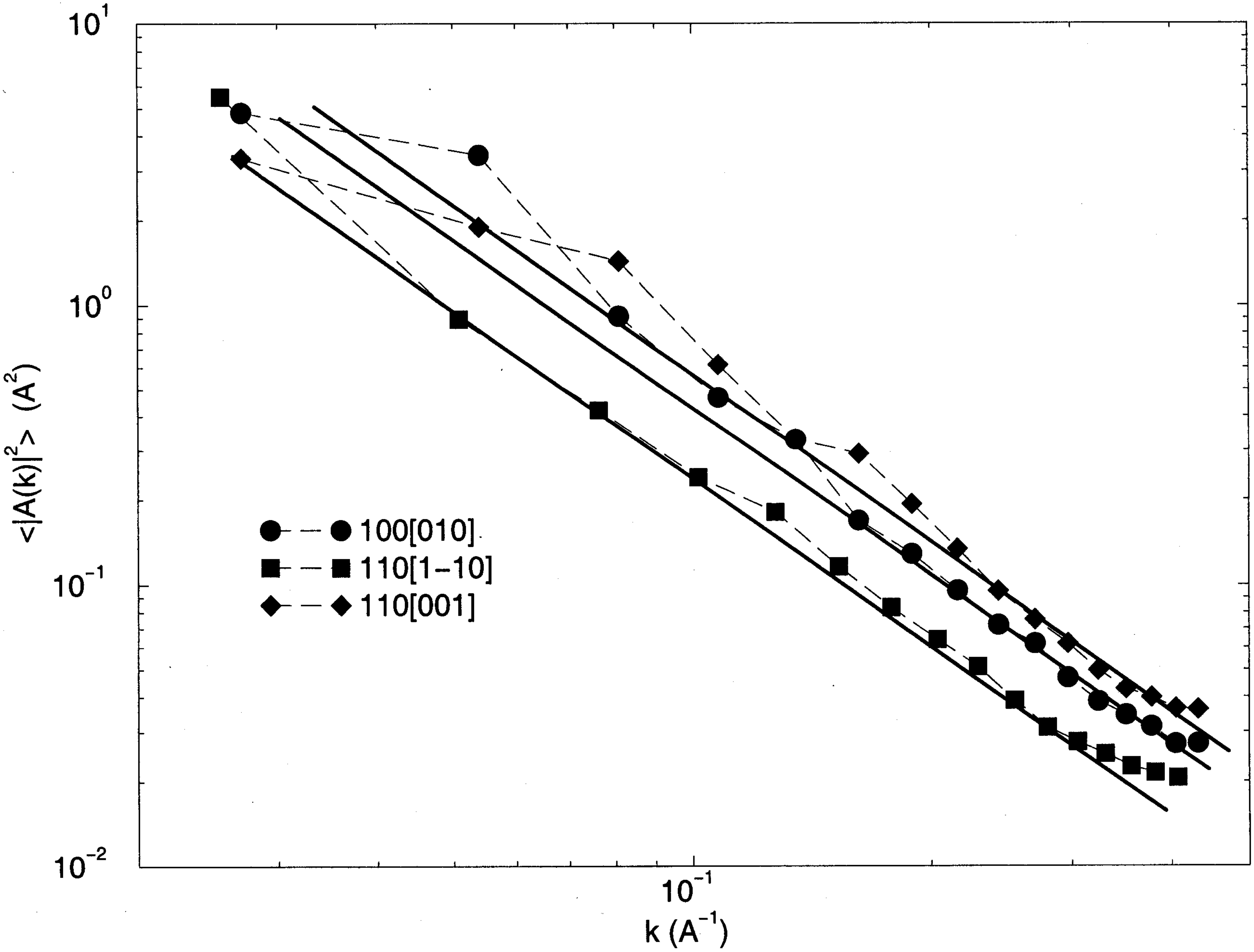

Fig. 4.1